The Pennsylvania State University

The Graduate School

Department of Material Science and Engineering

RELIABILITY AND AGING IN PATTERNED $Pb(Zr_{0.52}Ti_{0.48})O_3$ FILMS

A Dissertation in

Material Science and Engineering

by

Jung In Yang

© 2016 Jung In Yang

Submitted in Partial Fulfillment
of the Requirements
for the Degree of

Doctor of Philosophy

December 2016

The dissertation of Jung In Yang was reviewed and approved* by the following:

Susan Trolier-McKinstry
Professor of Ceramic Science and Engineering
Dissertation Advisor
Chair of Committee

Clive A. Randall
Professor of Material Science and Engineering

Srinivas Tadigadapa
Professor of Electrical Engineering

Venkatraman Gopalan
Professor of Material Science and Engineering

Suzanne Mohney
Professor of Materials Science and Engineering and Electrical Engineering
Chair, Intercollege Graduate Degree Program in Materials Science and Engineering

* Signatures are on file in the Graduate School

ABSTRACT

This research was targeted at understanding how and why aging and reliability are influenced by lateral feature size in PZT thin films patterned by ion beam milling and reactive ion etching.

Lead zirconate titanate, PZT thin films (with Zr/Ti ratios of 52/48) were grown on a $PbTiO_3$ seed layer and patterned into feature sizes of 100 μm, 50 μm and 10 μm using argon ion beam milling. It was found that as the pattern dimensions decreased, the remanent polarization increased, presumably due to the fact that the ferroelectric polarization near the feature perimeter is not as severely clamped to the substrate. It is believed that clamping at the film/substrate interface produces deeper wells that prevent some fraction of the spontaneous polarization from switching at high field. The dielectric nonlinearity in the serpentine patterned PZT thin films was described using the Rayleigh law at modest ac electric fields. Both Rayleigh parameters (ε_{init} and α) increased with decreasing serpentine line width after recovery annealing. It was observed that ε_{init} of 500 mm square patterns was 1510 ± 13; with decreasing serpentine line width, ε_{init} rose from 1520 ±10 for the 100 μm serpentine to 1568 ± 23 for the 10 μm serpentine. The irreversible parameter, α, for the square patterns was 39.4 ± 3.2 cm/kV and it increased to 44.1 ± 3.2 cm/kV as the lateral dimension is reduced. However, etched patterns also aged more rapidly. Based on this, it was concluded that sidewall damage produces shallow wells that lower the Rayleigh constants of aged samples at small fields. These observations are consistent with a model in which shallow wells can be overcome by the large fields used to measure the remanent

polarization and the large unipolar electric fields typically used to drive thin film piezoelectric actuators.

600nm thick PZT (52/48) thin films were also patterned into squares and antenna-shapes with feature sizes of 10 µm, 8 µm, 5 µm, and 2 µm using a reactive ion etching process. The effect of feature size on (1) highly accelerated lifetime tests (HALT), (2) the current-voltage (I-V) characteristics, and (3) the property stability as function of time using Rayleigh measurements was then investigated. HALT measurements were made at temperatures ranging from 120 ^{o}C to 180 ^{o}C and electric fields ranging from 100 kV/cm to 225 kV/cm. The characteristic time to failure t_{50} increased with decreasing feature size. The activation energy for all feature sizes were 0.82eV ~ 1.1eV; the range of voltage acceleration factors for all feature sizes was 3.4 ~ 5.2. It is hypothesized that the sidewall and the bulk of the film both contribute to the observed feature size dependence of the median time to failure and activation energy in patterned PZT thin film. HfO_2 was deposited using ALD to minimize sidewall damage such as dangling bonds on the etched surfaces. After ALD coating, the lifetime of all features sizes increases because the sidewall damage is partially recovered without significant changes in the activation energies.

I-V data were measured at temperatures ranging from 50°C to 150°C to investigate possible conduction mechanism. The most reasonable fits were obtained using a Schottky emission model.

To investigate the aging mechanisms for patterned PZT films, Rayleigh measurements were conducted as a function of time. Two methods were used to obtain preferred polarization states in the ferroelectric. First, patterned PZT films were exposed to a dc bias (poling); secondly, films were poled at elevated temperature to promote alignment of defect dipole complexes. Both poled and hot poled samples have loops that are shifted negatively along the electric field axis

due to development of the internal field. Thermal poling at 150 ^{o}C reduced aging rates to ~ 0.6 %/decade for ε_{init} and 1.1 %/decade for α. In contrast, the aging rate of unpoled samples were ~ 1.3 %/decade for ε_{init} and ~1.8 %/decade for α value. Also, all feature sizes showed the same trend; α / ε_{init} decreased rapidly over short time scales (on the order of 1-150 seconds) and then gradually decreased at longer time.

TABLE OF CONTENTS

LIST OF FIGURES x

LIST OF TABLES xix

ACKNOWLEDGEMENTS xxi

Chapter 1. Thesis Organization and Statement of Goals 1

Chapter 2. Literature Review 4

2.1 Piezoelectric Materials 4

2.2 Ferroelectric Materials 8

2.3 Ferroelectric Domain Structure and Formation 13

2.4 Lead Zirconate Titanate (PZT) 16

2.5 Intrinsic and Extrinsic Contributions to the Dielectric and Piezoelectric Response 19

2.6 Rayleigh Law 20

2.7 References 24

Chapter 3. Effect of Feature Size on Dielectric Nonlinearity of Serpentine Patterned $PbZr_{0.52}Ti_{0.48}O_3$ Films 29

3.1 Abstract 29

3.2 Introduction 31

3.3 Experimental Procedure 35

3.3.1 Chemical Solution Deposition Processing 35

3.3.2 Deposition and Crystallization of PZT Film with a PT Seed Layer 36

3.3.3 Patterning and Etching Process of PZT with PT Seed Layer Thin Film 36

3.3.4 Structural and Microstructural Characterizations 39

3.3.5 High and Low Field Ferroelectric and Dielectric Characterization 40
3.4 Results and Discussion 40
3.5 Conclusions 50
3.6 References 52

Chapter 4. Fabrication and Electrical Properties of Reactive Ion Etched Antenna Patterned PZT Thin Films 59

4.1 PZT Film Preparation 59
4.1.1 PZT Deposition 59
4.1.2 Top Electrode (Pt) and TiW Deposition 62
4.2 Film Patterning 64
4.2.1 Lift-Off Lithography 64
4.2.2 Nickel Electroplating 66
4.2.3 Top Pt and PZT Etching 69
4.2.4 Stripping of Ni and TiW Layers 71
4.3 Structure and Electrical Characterization 74
4.3.1 Continuous PZT (52/48) Thin Films 74
A. Crystal Structure and Microstructure of Continuous PZT Films 74
B. Electrical Properties of Continuous PZT Film 75
4.3.2 Patterned PZT (52/48) Thin Films 76
A. Microstructure 76
B. Dielectric and Ferroelectric Properties 77
4.4 References 81

Chapter 5. DC Electrical Field Reliability and Conduction Mechanisms of Patterned PZT Films

5.1 Introduction 82
5.2 Experimental Procedure 86

5.2.1 HALT Analysis 86

5.2.2 I-V Measurement Procedure 88

5.3 Results and Discussion 89

5.3.1 Reliability of 0.6 µm Thick Patterned PZT (52/48) Thin Films 89

A. Determination of The MTTF (t_{50}) Using The Weibull Lifetime Distribution ...92

B. Determination of The MTTF (t_{50}) Using Lognormal Distribution 100

C. Determination of Activation Energy 106

D. Microstructure after HALT Measurement 119

E. Determination of Voltage Acceleration Factor 121

5.3.2 Conduction Mechanisms in 0.6 µm Thick Patterned PZT (52/48) Thin Film..124

A. Schottky Emission 125

B. Poole - Frenkel Emission (PF emission) 127

5.4 Conclusions 134

5.5 References 137

Chapter 6. Aging Behavior in Patterned PZT (52/48) Thin Films 145

6.1 Introduction 145

A. Volume Effect (Bulk Effect) 149

B. Domain Wall Effect 151

C. Interface Effect 151

6.2 Experimental Procedure 153

6.2.1 Aging of the Rayleigh Parameters 153

6.2.2 Imprint of Patterned PZT (52/48) Thin Films – Poling and Hot Poling 155

6.2.3 Polarization Measurement 155

6.3 Results and Discussion 155

6.3.1 Effect of Poling and Hot Poling on The Rayleigh Parameters of Patterned PZT Thin Films 155

6.3.2 Rayleigh Parameters of Aging Behavior on Patterned PZT Thin Films 159

6.4 Conclusions 165

6.5 References 167

Chapter 7. Conclusions and Future Work 173

7.1 Effect of Feature Size on Dielectric Nonlinearity of Serpentine Patterned PZT Films..173

7.2 DC Electrical Field Reliability and Conduction Mechanism of Antennae Patterned PZT Films 174

7.3 Aging Behavior in Patterned PZT (52/48) Thin Films 175

7.4 Future Work 176

7.4.1 Thermally Stimulated Deposition Current (TSDC) in Patterned PZT (52/48) Thin Films 176

7.4.2 Effect of Patterning Techniques on Reliability of Patterned PZT Thin Films..178

7.4.3 AC Electric Stress Reliability of Patterned PZT Thin Films 179

7.4.4 Method of Classification Between Effect of Sidewall Damage and Bulk Damage of Patterned PZT Films ………………………………………………………181

7.5 References 183

LIST OF FIGURES

Figure 2.1. Schematic showing the classification of the 32 crystallographic point groups

Figure 2.2. A schematic of (a) the direct piezoelectric effect: surface charges are generated on the surface upon the application of compressive and tensile stress and (b) the converse effect: a strain (dimensional change) develops upon the application of an electric field. The solid lines show the original dimensions and the dotted lines indicate a change in the dimension of the material

Figure 2.3. Schematic diagram showing the relationships among piezoelectrics, pyroelectrics and ferroelectrics

Figure 2.4. Schematic representation of the unit cell of perovskite structure of ABO_3

Figure 2.5. Unit-cell distortion of the $BaTiO_3$ polymorphs (modified from reference [3])

Figure 2.6. A typical polarization – electric field (P-E) hysteresis loop for a polycrystalline ferroelectric sample (taken from reference [7])

Figure 2.7. Schematic showing the relation between a P-E loop and domain configurations at selected points in a uniaxial ferroelectric single crystal

Figure 2.8. Possible polarization directions referenced to the cubic prototype for (a) tetragonal perovskite with 6 equivalent <001> directions, (b) orthorhombic distortion with 12 equivalent <110> directions, or (c) rhombohedral with 8 equivalent <111> directions

Figure 2.9. Schematic diagrams of (a) 180° domain walls and (b) non-180° domain walls and (c) a mixed domain structure in a ferroelectric crystal (from reference [7])

Figure 2.10. Illustration of the possible polarization directions in a rhombohedral perovskite. (Only the upward polarization directions are indicated) (from reference [7])

Figure 2.11. Schematic illustration of 180° and 90° domain walls in the tetragonal perovskite crystal like $BaTiO_3$ (E_d: the depolarizing field, P_s: spontaneous polarization) (modified from reference [13])

Figure 2.12. PZT phase diagram (established in Jaffe et al. (1971) [3] and Noheda et al. [8] (2000). The figure is modified from reference [3])

Figure 2.13. Composition dependence of (a) the dielectric constant and (b) the piezoelectric charge coefficient of PZT (from references [16][17])

Figure 2.14. The dielectric nonlinearity ε_{11} and ε_{33} under an application of AC field in soft PZT ceramics, after Li et al. (taken from reference [22])

Figure 2.15. Illustration of (a) the interaction of domain walls with randomly distributed pinning centers and (b) the corresponding energy profile associated with the domain wall position. (taken from reference [27])

Figure 2.16. Illustration of the AC field dependence of the dielectric permittivity of hard PZT ceramic (modified from reference [29])

Figure. 3.1. Fabrication process flow of 0.5 μm patterned PZT (52/48) with $PbTiO_3$ seed layer (right side is cross-section view and left side is top view)

Figure 3.2. Device layout of patterned 0.5 μm thick PZT (52/48) with $PbTiO_3$ seed layer

Figure. 3.3. XRD patterns of 0.5 μm patterned PZT (52/48) with $PbTiO_3$ seed layer. The starred peaks arise from the substrate

Figure 3.4. FESEM micrograph of a serpentine patterned PZT (52/48) on a $PbTiO_3$ seed layer. (a) the cross-sectional image, (b) the expansion of the cross-sectional image and (c) top surface of 10 μm serpentine line width

Figure. 3.5. The frequency dependence of the dielectric constants and tangent loss for 0.5 μm PZT (52/48) with a $PbTiO_3$ seed layer. High frequency data for serpentine structures are contaminated by artifacts associated with the RC time constant for the capacitors studied

Figure. 3.6. Rayleigh parameter of a 0.5 μm thick patterned PZT (52/48) on a $PbTiO_3$ seed layer (a) after recovery annealing and (b) after aging for 9 months

Figure. 3.7. Normalized aging of the dielectric permittivity

Figure. 3.8. (a) P-E hysteresis loop measured at 100 Hz at 25V on serpentine structures with varying degrees of substrate clamping. (b) Change in remanent polarization and coercive field of 0.5 μm patterned PZT (52/48) on a $PbTiO_3$ seed layer

Figure. 3.9. A schematic of a potential energy landscape associated with the domain wall position: energy profile of shallow well due to side wall damage and surface degradation and deep well due to clamping

Figure 4.1. Schematic diagram of PZT film deposition

Figure 4.2. FESEM micrograph of a surface of PZT (52/48) (a) before PbO capping image, (b) after PbO capping

Figure 4.3. Fabrication flow for the stack growth of (a) the PZT layer on platinized Si substrate, (b) the Pt layer on the crystallized PZT film and (c) the TiW layer on Pt

Figure 4.4. A fabrication flow- top view and cross sectional view of lithography

Figure 4.5. Schematic of stepper 8000 with design of reticle: antenna shaped 2 μm, 5 μm, 8 μm, 10 μm, circle and square

Figure 4.6. A fabrication flow- top view and cross sectional view of developing and oxygen plasma ashing after exposure

Figure 4.7. Illustration of Ni electroplating process and process parameters

Figure 4.8. Fabrication flow used for Ni electroplating to form the Ni hard mask and remove the photoresist

Figure 4.9. Optical images of surface of 10 μm arm size of PZT film after Ni electroplating (a) at 2V and (b) at 1V

Figure 4.10. Fabrication flow: etching of top Pt electrode and the PZT film

Figure 4.11. Fabrication flow: stripping of Ni and TiW

Figure 4.12. Schematic diagram of (a) each feature size antennae structure and (b) final sample structure with typical line widths of the antenna shaped including 10 μm, 8μm, 5 μm, 2 μm, and square and circle designs

Figure 4.13. (a) X-ray diffraction patterns (asterisks indicate peaks from the silicon or the Pt from radiation wavelengths other than Cu Ka) and (b) surface microstructure of the continuous PZT (52/48) film

Figure 4.14. (a) Frequency dependence of the dielectric constants and tangent loss and (b) the polarization-electric field hysteresis loop of a 0.6 μm thick continuous PZT (52/48) film

Figure 4.15. FESEM micrograph of a 2 μm, 5 μm, 8 μm or 10 μm wide arms of the antenna patterned 0.6 μm PZT (52/48) film. Dry etching was completed using a Ni hard mask.

Figure 4.16. (a) Frequency dependence of the dielectric constants and (b) tangent loss of a 0.6 μm thick antenna shaped PZT (52/48) film

Figure 4.17. (a) The field dependence of dielectric constant and (b) reversible (ε_{init}) and irreversible Rayleigh (α) coefficient as a function of aspect ratio

Figure 4.18 (a) P-E hysteresis loop and (b) remanent polarization film for a 0.6 μm thick antenna shaped PZT (52/48) film as function of lateral feature size

Figure 5.1. Images of (a) HALT system, which was composed of a Keithley 6517A electrometer/high resistance meter, temperature controller and box for electronics and (b) sample stage with wirebonded sample on 24 DIP package

Figure 5.2. Current density– time characteristics of a patterned 0.6 μm PZT (52/48) thin film measured (a) at various temperatures (120 °C, 150 °C and 180 °C) with applied electric field of 225 kV/cm and (b) at three different voltages (100 kV/cm, 150 kV/cm, 225 kV/cm) at 150°C

Figure 5.3. Plots of comparing the influence of the shape parameters on the Weibull distributions for different functions

Figure 5.4. The bathtub curve of the failure rate, modified from Ref (18)

Figure 5.5. Weibull distribution with varying scale parameters (η)

Figure 5.6. Weibull plots of time to failure of patterned PZT (52/48) thin film (a) at three different temperatures of 120 °C, 150 °C and 180 °C with 225 kV/cm and (b) at three different electric fields of 100, 150 and 225 kV/cm at constant temperature of 150°C

Figure 5.7. Mean time to failure, calculated from Weibull distribution function, as a function of (a) temperature at 225 kV/cm and (b) electric field at 150 °C for 0.6 μm thick patterned PZT (52/48) thin film

Figure 5.8. The S- shaped curved of cumulative percent failure plot (adapted from reference [23])

Figure 5.9. Plot of cumulative percentage failure versus time from HALT data of 5 μm feature size PZT (52/48) thin film measured at 150°C and 225kV/cm

Figure 5.10. Mean time to failure, calculated from the cumulative percentage failure plot, as a function of (a) temperature at 225 kV/cm and (b) electric field at 150 ^{o}C for 0.6 μm thick patterned PZT (52/48) thin film

Figure 5.11. Plots of (a) the ln mean time to failure vs 1000/T, (b) the activation energy of all feature sizes under three different temperatures of 120 ^{o}C, 150 ^{o}C and 180 ^{o}C at electric field of 225kV/cm

Figure. 5.12. Schematic mechanisms associated with failure of antennae shaped 2 μm arm size and 10 μm arm size along with a possible energy band diagram

Figure 5.13. Weibull plots of time to failure of HfO_2 ALD coated PZT (52/48) thin film (a) at three different temperatures of 120 ^{o}C, 150 ^{o}C and 180 ^{o}C with 225 kV/cm and (b) at three different voltages of 100 kV/cm, 150 kV/cm and 225 kV/cm with 150°C

Figure 5.14. Comparisons of mean time to failure and activation energy between uncoated and HfO_2 coated 0.6 μm thick patterned PZT (52/48) thin films. (Calculated from the Weibull distribution function)

Figure 5.15. FE-SEM micrograph of surface of Pt/PZT/Pt layers after HALT measurements. (a) the comparison between before and after HALT testing; (b) and (c) are magnified blackened spots on 5 μm bondpad and 8 μm arms respectively

Figure 5.16. Plots of (a) the ln mean time to failure, (b) and (c) the voltage acceleration factor of all feature sizes (data from measurements at 100 kV/cm, 150 kV/cm or 225 kV/cm at a temperature of 150 ^{o}C) to calculate the voltage acceleration factor from the slope of the line (Experimental data were taken from 0.6 μm thick patterned PZT (52/48) thin films without ALD HfO_2 coating)

Figure 5.17. The plot and table of comparisons of voltage acceleration factors obtained from the Eyring equation and Garten model (Experimental data were taken from 0.6 μm thick patterned PZT (52/48) thin films without ALD HfO_2 coating).

Figure 5.18. A schematic diagram of Schottky emission; (a) a metal and p-type ferroelectric thin film with labeled metal and ferroelectric work function ϕ_M, ϕ_F, Fermi energy (E_{FM}) (b) deformed energy band structure after contact. ϕ_B: Schottky barrier height

Figure 5.19. The schematic diagram of the Poole - Frenkel emission

Figure 5.20. I-V characteristics of 0.6 μm patterned PZT (52/48) measured from 0V to 50V at room temperature

Figure 5.21. ln (J/T^2) versus $E^{0.5}$ as function of temperature for 0.6 μm thick patterned PZT films with different lateral feature sizes (The current is fitted well with Schottky emission model at high electrical fields)

Figure 5.22. ln (J/E) versus $E^{0.5}$ as function of temperature of 0.6 μm patterned PZT film (The current is fitted well with Poole- Frenkel emission model at high electrical fields)

Figure 5.23. Plots of the experimental refractive index as a function of temperature extracted from Schottky and Pool-Frenkel emission models

Figure 5.24. Evaluation of the barrier height for the Schottky emission model. In the table, values of barrier heights for all feature size are listed

Figure 6.1. Schematic diagram of the polarization-electric field (P-E) hysteresis loop showing strongly pinched curve on aging [1]

Figure 6.2. Aging of the dielectric, piezoelectric coupling factor and resonance frequency constant of poled PZT (modified from [2])

Figure 6.3. Illustrations of volume effect for aging: (a) a defect dipole within the unit cell, in practice distributed defect dipoles are also possible; (b) domain stabilization by defect complexes interacting with the spontaneous polarization; (c) Aligned defect dipoles by the reorientation of oxygen vacancy within the octahedron

Figure 6.4. Schematic diagram of the domain wall-based aging mechanism

Figure 6.5. Schematic diagram of grain boundary effect on aging phenomena (modified from [24])

Figure 6.6. Images of (a) aging system with built in temperature controller, and (b) sample stage with a high temperature ceramic socket for wirebonded sample on 24 pin DIP package

Figure. 6.7. The dielectric constant as a function of ac electric field of poled (at 150 kV/cm for 10 min) 0.6 μm thick patterned PZT (52/48) thin films with different lateral feature sizes (as shown in the caption)

Figure 6.8. Variation of (a) ε_{init} and (b) α values of 0.6 μm thick patterned PZT (52/48) thin films as a function of poling time with the top electrode at positive bias. Films were poled at 150 kV/cm, which is two times the coercive field of the film

Figure 6.9. Variation of (a) ε_{init} and (b) α values of 0.6 μm thick patterned PZT (52/48) thin films as a function of room temperature poling and hot poling with the top electrode at positive bias

Figure 6.10. Comparison of the aging rate of Rayleigh parameters for 0.6 μm thick patterned PZT (52/48) thin films patterned by reactive ion etching

Figure 6.11. (a) The P-E hysteresis loops and (b) plot of internal fields after imprint for unpoled, room temperature poled, and hot poled antenna patterned PZT (52/48) thin films

Figure 6.12. Plots of the ratio of irreversible to reversible Rayleigh parameters ($\alpha/\varepsilon_{init}$) as function of time after imprint

Figure. 6.13. Comparison of the aging rate of the ratio of $\alpha/\varepsilon_{init}$ for 0.6 μm patterned PZT (52/48) thin films after imprint

Figure 6.14. Comparison of percent changes in $\alpha/\varepsilon_{init}$ response for the aging period of 30000 seconds for unpoled, room temperature poled and hot poled patterned PZT (52/48) thin films

Figure 7.1. Schematic of TSDC field and temperature profile (taken from [2])

Figure 7.2. Images of (a) AC HALT system, which was composed of LCR meter, pA meter, amplifiers, temperature controller and sample holder and (b) sample stage with wirebonded sample on a 28 pin DIP package.

Figure 7.3. Schematic of two different etching process, FIB fabrication and Ar ion milling, of PZT thin film; (a) the patterned PZT capacitor can be fabricated by using focused ion beam milling (FIB) with trenches around the perimeter of patterned PZT and (b) PZT thin film will etch using Ar ion milling to pattern

LIST OF TABLES

Table 2.1. Possible polarization directions in a perovskite relative to the cubic prototype cell

Table 3.1. Reported approaches for etching of ferroelectric films

Table 3.2. Parameters used for ion-milling PZT and Pt

Table 4.1. Typical sputtering parameters for the Pt film growth and post-annealing conditions

Table 4.2. Typical sputtering parameters for the TiW layer growth

Table 4.3. Oxygen plasma ashing parameters

Table 4.4. Reactive ion etch parameters for top Pt and PZT layers. (ICP = inductively coupled plasma)

Table 5.1. Reported resistance degradation mechanisms of bulk and thin film of lead based perovskite materials (modified from reference [12])

Table 5.2. Mean time to failure (MTTF) and Weibull parameters measured at temperatures of 120 ^{o}C, 150 ^{o}C or 180 ^{o}C for an electric field 225 kV/cm for patterned PZT (52/48) thin films

Table. 5.3. Mean time to failure (MTTF) and Weibull parameters measured at electric fields of 100, 150 or 225 kV/cm and a constant temperature of 150 ^{o}C for patterned PZT (52/48) thin films

Table 5.4. Example of failure data with cumulative frequency and percentage

Table 5.5. Mean time to failure (MTTF) obtained from a cumulative percentage failure plot measured at electric fields of 100, 150 and 225 kV/cm at constant temperature of 150°C and also at 120°C, 150°C and 180°C at constant electric field 225 kV/cm for 0.6 μm thick patterned PZT (52/48) films

Table 5.6. Summary of comparisons of results between blanket film PZT thin films and patterned 2 μm arm size PZT (52/48) thin film

Table 5.7 The comparison of lifetime between blanket film PZT thin films and patterned 2 μm arm size PZT (52/48) thin film

Table 5.8. Comparison between 2 μm and 10 μm feature size PZT (52/48) thin films

Table 5.9. Atomic layer deposition parameters for the patterned PZT films

Table. 5.10. Mean time to failure (MTTF) and Weibull parameters measured at (a) three different temperatures of 120 ^{o}C, 150 ^{o}C and 180 ^{o}C with 225 kV/cm (150 kV for 2 μm) for ALD coated PZT (52/48) thin films

Table 5.11. Mean time to failure (MTTF) and Weibull parameters measured at three different electric fields of 100, 150 and 225 kV/cm at constant temperature of 150 ^{o}C for HfO_2 ALD coated PZT (52/48) thin film

Table 5.12. Lists of conduction mechanisms

Table 5.13. The refractive index as a function of temperature extracted from Schottky and Poole - Frenkel emission models

Table 6.1. Reported permittivity aging rate for PZT

Table 7.1. Summary of different etching techniques

ACKNOWLEDGEMENTS

I would not have been able to finish my PhD without considerable help from many people on both the scientific and human sides. So I would like to thank all of them.

My first thought goes to Prof. Susan Trolier-McKinstry, who gave me the opportunity to study again; she provided direction and guidance not only in terms of scientific knowledge, but also as a parent and human as well. I cannot tell her how much I appreciate what she has done. I truly thank her for patience, support, great advice and comments. I would like to say that “Thank you again and always respect you”.

Also I wish to thanks my committee members, Professors Clive Randall, Gopalan Venkatraman and Srinivas Tadigadapa for their encouragement, useful comments, and directions.

Very special gratitude to the MRL staff: Paul Moses and Jeff Long for electrical measurement setups used in this research. Thanks also to the staffs of the Nanofab and MCL: Bill Drawl, Guy Lavallee, Kathy Gehoski, Bangzhi Liu, Chad Eichfeld, Andrew Fitzgerald, Michael Labella, Beth Jones, Shane Miller, Jaime Reish, Nichole Wonderling, and Maria Di Cola. I was able to finish my work because of their never-ending support. Thanks to Susie Sherlock and Amanda Brooks for their happy smiles and advice on how to deal with kids.

I must thank the whole STM group, past and present; I had the happiness to know them, and to discuss and chat about scientific knowledge and life in State College. I feel that I am so lucky to meet you all: Aaron, Adarsh, Charley, Dan M, Derek, Raegan, Hong Goo, Lauren, Sun Young, Wanlin, Julian, Smitha, Jon, Margeaux, Trent, Betul, Ryan, Dixiong, Lyndsey, Carl and Tianning.

Another special thanks to the Jung family (Yun Sik, Eun Ju, Esther and Angela); They took care of my three kids with great love and showed me how to love other people. I could not finished my PhD without their support and prayers. I really appreciate what they have done and I miss them so much.

My warmest thanks to my family. My life can be divided into before marriage and after marriage. First of all, I would like to warmest thanks to before marriage family members: my parents (Ki Ju and Yong Za), sister (Yun Jeong) and brother (Tae Young) for their endless support and love. Especial thanks to my mom. I can feel and understand your love and tears. I love you Mom! Also, I would like to thank my after marriage family members: my mother-in-law and father-in-law for their prayers and support and to my sister-in-law(Doo Hee) and brother-in-law(Tom). Finally, my hearty thanks to my husband, Song Won, my daughter, Ellie, son Eric and my daughter Laya. During this PhD, we made a big family. My friend, colleague and lover, Song Won was always with me to help and guide me. “Thank you a lot and love you so much Song Won”. Sometimes, it was beyond my capacity to deal with both family and research, but their love, smiles and happiness made me cheer up and feel encouraged again. So, I could achieve this work.

Chapter 1

Thesis Organization and Statement of Goals

This first chapter describes the organization of the thesis. The remainder of the dissertation is organized as follows:

Literature review (Chapter 2)

This chapter provides fundamental background related to the characteristic of piezoelectric and ferroelectric materials. Also, the intrinsic and extrinsic contributions to the dielectric and piezoelectric properties are reviewed. Finally, the Rayleigh law is introduced to describe the dielectric nonlinearity.

Effect of Feature Size on Dielectric Nonlinearity of Serpentine Patterned $PbZr_{0.52}Ti_{0.48}O_3$ Films (Chapter 3)

PZT 52/48 thin films were patterned into serpentine designs including different lateral sizes of squares and 100 μm, 50 μm and 10 μm feature size using ion beam milling. To investigate the dielectric nonlinearity in the patterned PZT thin films, the Rayleigh law was used to explain the behavior of Rayleigh parameters as a function of feature size. It was found that ε_{init} and α increased for smaller feature sizes; this was attributed to changes in the potential energy wells associated with substrate clamping and sidewall damage.

Fabrication and Electrical Properties of Reactive Ion Etched Antenna Patterned PZT Thin Films (Chapter 4)

This chapter introduces experimental procedures for developing patterned PZT thin films with different feature sizes, from large squares to antenna-shaped patterns with 10 μm, 8 μm, 5 μm or 2 μm feature sizes using reactive ion etching. Also, the baseline of electrical properties, including dielectric constant and dielectric loss, P-E hysteresis and Rayleigh parameters were examined to establish possible origins for the electrical property changes on decreasing the lateral feature size.

DC Electrical Field Reliability and Conduction Mechanisms of Patterned PZT Films (Chapter 5)

This chapter examines the time-dependent dielectric breakdown and lifetime characteristics as a function of feature size by applying highly accelerated lifetime test (HALT), as well as the current-voltage (I-V) characteristics. The breakdown behavior of the patterned PZT (52/48) thin films were evaluated using a Weibull distribution. Also, the procedures for calculation for the median time to failure, the activation energy and the voltage acceleration factor were introduced. The relative roles of the feature sidewalls and the bulk of the PZT film were examined. Also, I-V measurement was performed as function of different temperatures ranging to investigate possible conduction mechanisms in patterned PZT thin film.

Aging Behavior in Patterned PZT (52/48) Thin Films (Chapter 6)

The time dependence of the nonlinearity of the dielectric response for antennae structures were investigated via measurement of the Rayleigh law as a function of lateral feature size and

poling conditions. The effect of room temperature poling field and time on the Rayleigh parameter were determined as a function of lateral feature size. Also, the dielectric nonlinearities and aging behaviors following hot poling were studied to improve the dielectric reliability.

Conclusions and Future Work (Chapter 7)

This chapter summarizes the primary results of the thesis, as well as suggestions for future work.

Chapter 2

Literature Review

This chapter provides an overview of the literature relevant to the current work. First, a general background on the characteristics of piezoelectric and ferroelectric materials is offered. Piezoelectricity and ferroelectricity are reviewed along with ferroelectric domain formation and the different contributions (intrinsic and extrinsic) to the dielectric and piezoelectric properties. Finally, the chapter will conclude with a review of the Rayleigh law.

2.1. Piezoelectric Materials

In 1880, Jacques and Pierre Curie discovered the direct piezoelectric effect. The piezoelectric effect is possible in 20 out of 32 point groups; all of the piezoelectric groups are non-centrosymmetric as shown in Figure 2.1.[(1)(2)] For example, quartz exhibits this effect. In the second world war, barium titanate ($BaTiO_3$), lead zirconate titanate (PZT) and lead titanate ($PbTiO_3$) replaced natural piezoelectrics.

Piezoelectric materials convert between the mechanical and electric energies. For instance, when a mechanical stress is applied to piezoelectric materials, the atomic positions change and a dipole moment is generated (or changed).[(2),(3)(4)] To develop a net polarization in the crystal, the dipole cannot be neutralized by other dipoles in the unit cell. Therefore, the piezoelectric material should be non-centrosymmetric.

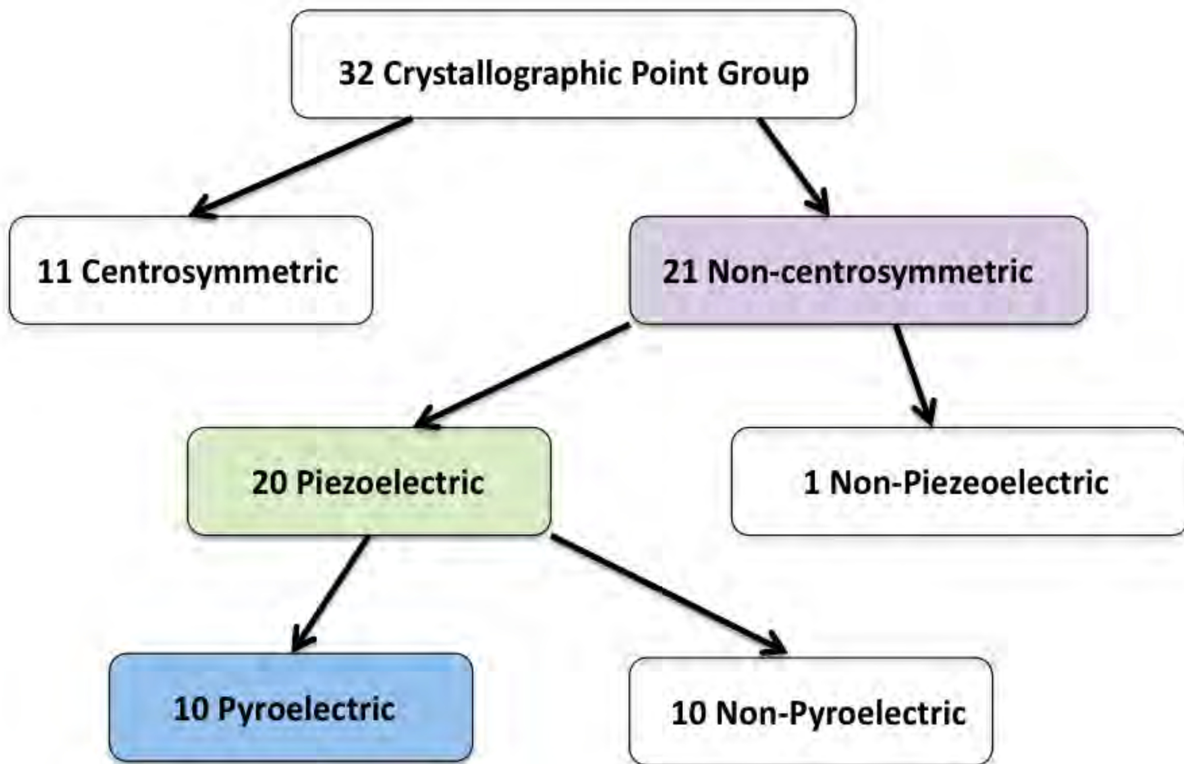

Figure 2.1. Schematic showing the classification of the 32 crystallographic point groups

To explain the direct and converse piezoelectric effects, it is useful to define the polarization in several ways. First the polarization can be defined as the dipole moment per unit volume, as described by equation 2.1. [4]

$$P = \frac{\sum \mu}{V} \qquad \text{Equation (2.1)}$$

where P is the polarization, μ is the dipole moment and V is the volume.

In a piezoelectric material, a surface charge will develop due to a change in the polarization when a stress is applied, if the crystal is homogenous. The polarization (P) can be designated as the charge (Q) per unit area (A) developed on the surface as shown in equation 2.2. [4]

$$P = \frac{Q}{A}$$ Equation (2.2)

$[C/m^2] = [C]/[m^2]$

For a piezoelectric material, the polarization is directly proportional to the applied stress (called the direct effect), as described by equation 2.3: [4]

$$P = d\sigma$$ Equation (2.3)

$[C/m^2] = [C/N]\,[N/m^2]$

where P = polarization, d = piezoelectric coefficient, σ = stress.

Conversely, when an electric field is applied to a piezoelectric material, the material experiences a dimension change, such as an expansion or contraction of the unit cell. The change in dimension is called the converse effect, as described by equation 2.4. [4]

$$\varepsilon = dE$$ Equation (2.4)

Unitless $= [m/V][V/m]$

where ε = strain, d = piezoelectric coefficient, E = electric field.

The direct and converse piezoelectric effects are illustrated in Figure 2.2 (a) and (b) respectively.

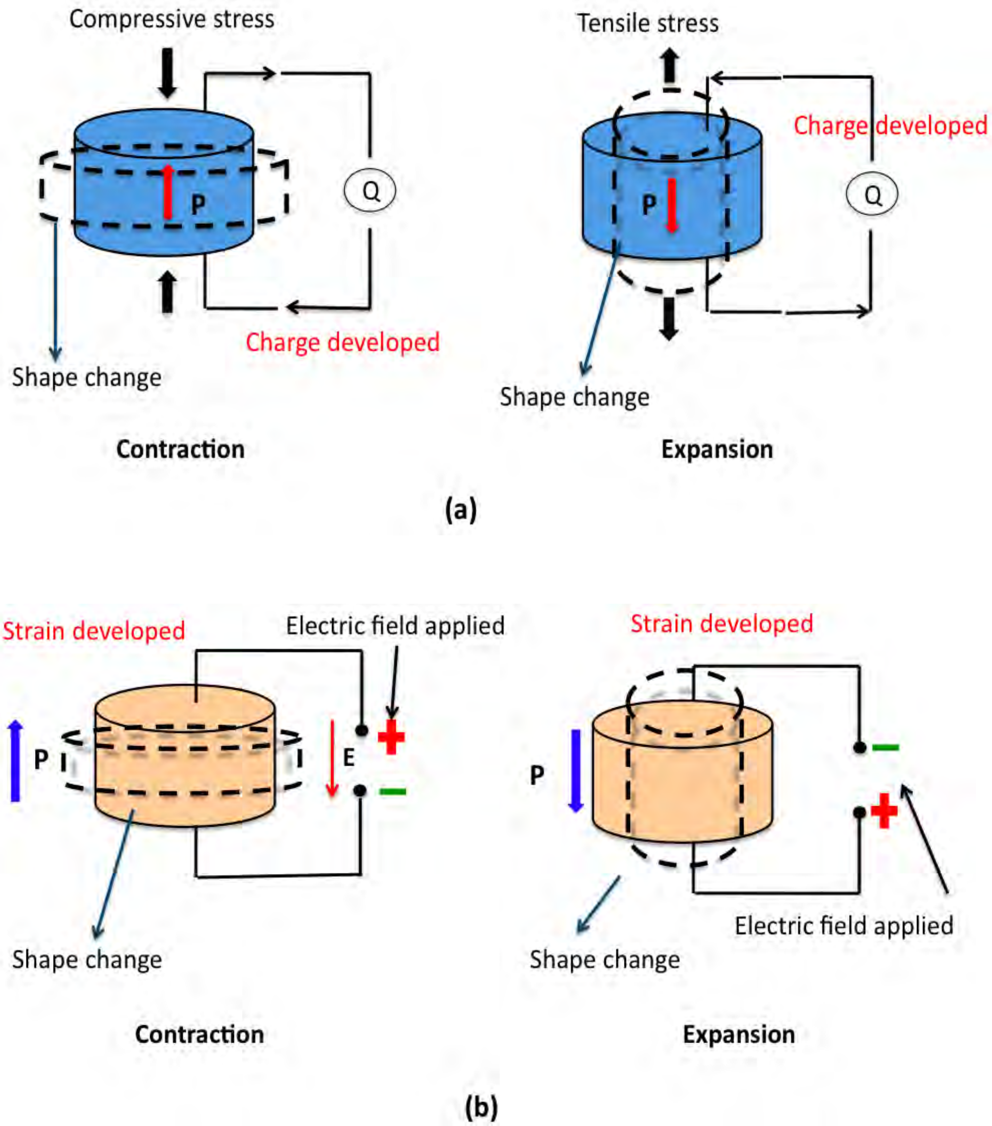

Figure 2.2. A schematic of (a) the direct piezoelectric effect: surface charges are generated on the surface upon the application of compressive and tensile stress and (b) the converse effect: a strain (dimensional change) develops upon the application of an electric field. The solid lines show the original dimensions and the dotted lines indicate a change in the dimension of the material.

2.2 Ferroelectric Materials

Ferroelectrics are materials in which the spontaneous polarization can be re-oriented between crystallographically-defined states by the application of an electric field. As shown in Figure 2.3, all ferroelectrics are piezoelectric and pyroelectric, but not all piezoelectrics are ferroelectric.[(1)(2)(3)(4)(5)] Pyroelectric materials have a temperature dependence of the spontaneous polarization. For example, when temperature is increased, most pyroelectric materials experience a decrease in their polarization.

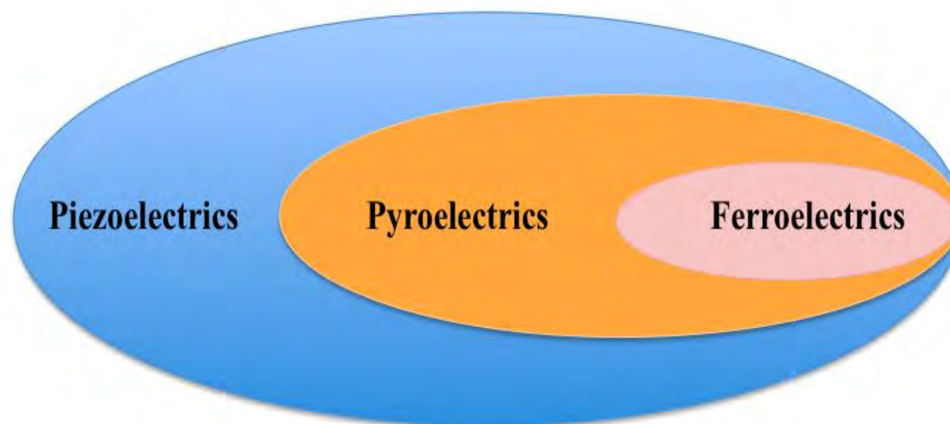

Figure 2.3. Schematic diagram showing the relationships among piezoelectrics, pyroelectrics and ferroelectrics

Ferroelectrics are a sub-group of the pyroelectric crystal classes. Some ferroelectric materials like PZT and $BaTiO_3$ transform from a paraelectric phase at high temperature into the ferroelectric phase at the Curie temperature (T_c). One of the most well-known crystal structure

for ferroelectrics is the perovskite structure. In the perovskite structure, the general formula is ABO_3 (see Figure 2.4), where, A-site and B-site cations can have from +1 to +3 and +3 to +6 charges, respectively. (5)(6)

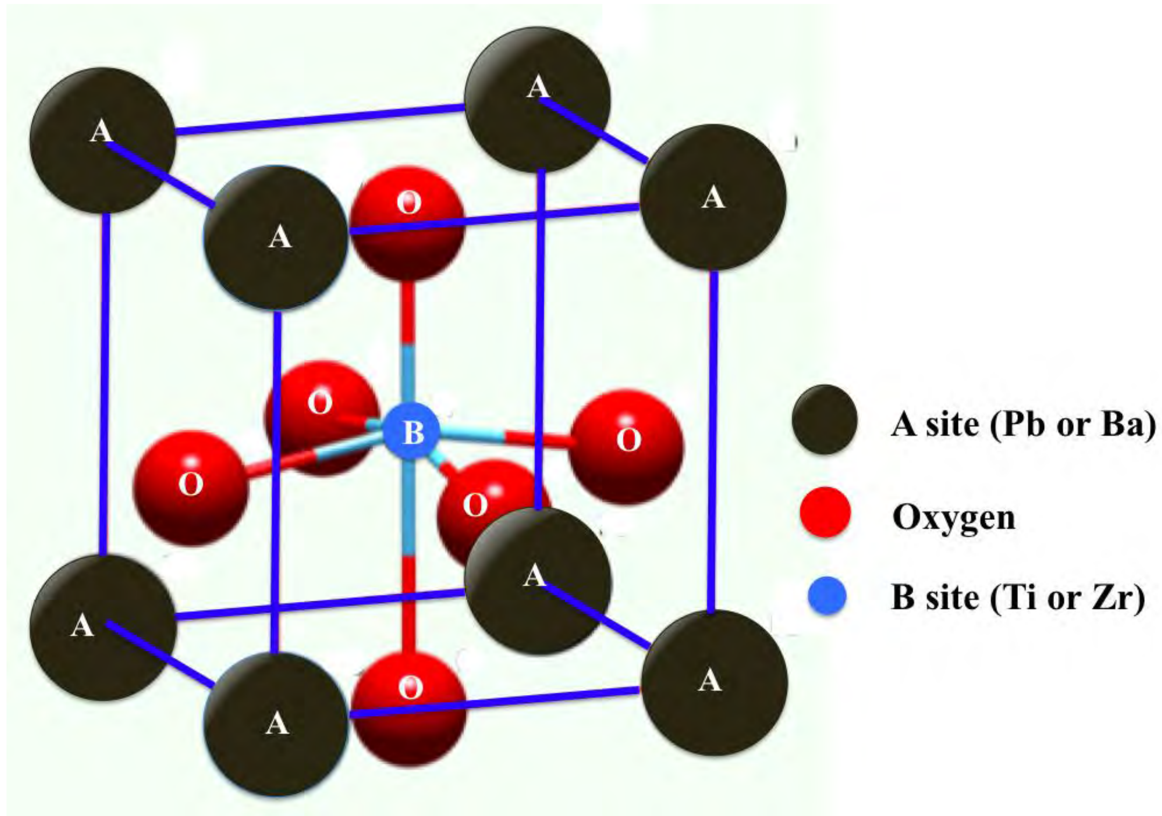

Figure 2.4. Schematic representation of the unit cell of perovskite structure of ABO_3

An example of ferroelectric material with the perovskite structure is $BaTiO_3$, for which the Ba atoms are placed at the unit cell corners (the A sites), oxygen atoms occupy the face centers, and the smaller Ti atoms sit at the B sites. As shown in Figure 2.5, $BaTiO_3$ undergoes polymorphic phase transitions. Above 130°C, $BaTiO_3$ is cubic. When cooled through ~ 130°C,

the unit cell distorts to a tetragonal phase with an accompanying motion of the Ti atom along one of the <100> directions. On cooling to ~5°C, the material undergoes a phase transformation to an orthorhombic phase with the polarization along one of the <101> directions of the cubic cell. At temperature below ~-90°C, the orthorhombic phase undergoes a transition to a rhombohedral phase, with the Ti atom moving along one of the <111> directions of the cubic cell.(3)(4)

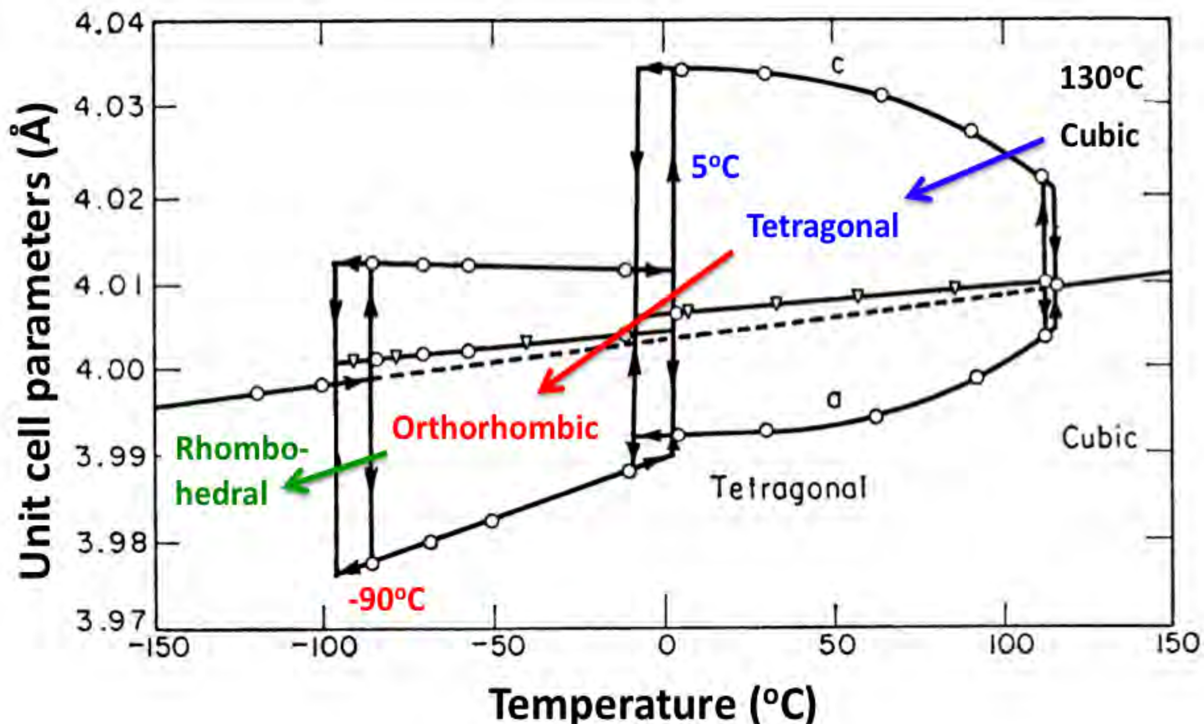

Figure 2.5. Unit-cell distortion of the $BaTiO_3$ polymorphs (modified from reference [3])

The most important characteristic of ferroelectric materials is polarization switching between crystallographically defined states by an electric field. A reorientable spontaneous polarization occurs at T_c in each unit cell of the material. The polarization can be reoriented into different equilibrium states under an application of electric field, leading to ferroelectricity. The polarization-electric field (P-E) hysteresis loops describe the net polarization of the material

under AC voltage excitation. As shown in Figure 2.6, the saturation polarization, P_{sat}, is the linear extrapolation at zero field of the high field polarization. The remanent polarization, P_r, is the actual value of polarization at zero field. The coercive field, E_c, is the field at a net zero polarization. [(5)(6)(7)]

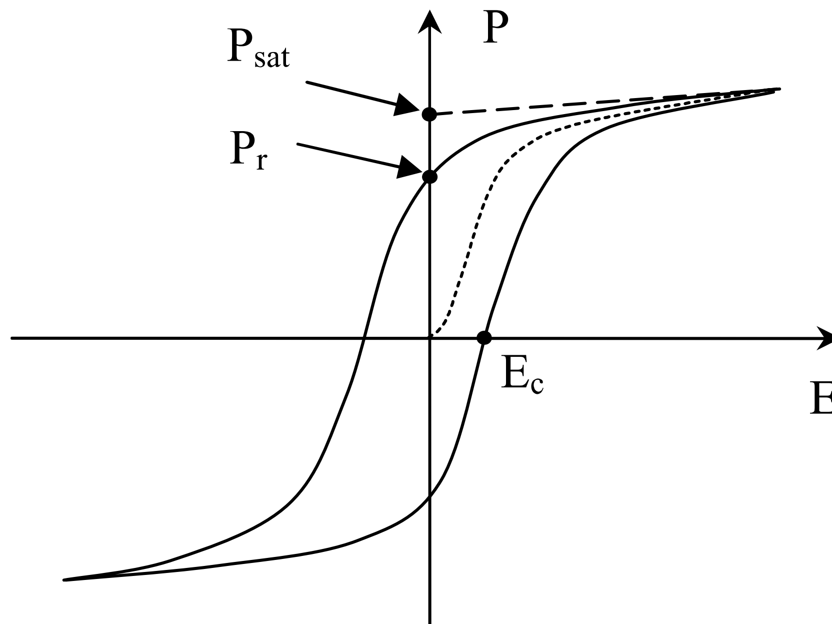

Figure 2.6. A typical polarization – electric field (P-E) hysteresis loop for a polycrystalline ferroelectric sample. (taken from reference [7]).

Figure 2.7 shows the relation between one possible domain configuration and the P-E loop for a ferroelectric crystal. Starting at point (1), the ferroelectric is depolarized. In this case, for small values of the applied alternating electric field, the polarization increases approximately linearly with the field amplitude. Such small fields do not switch domains with an unfavorable polarization direction (point (2)). When a large dc field is applied, domains begin to reorient (point (3)); the polarization becomes saturated at point (4). When the field strength is reduced,

some domains back-switch, but at zero field some domain alignment is retained. This polarization is called the remanent polarization (P_r). If the field is reversed, domains with the opposite direction nucleate and grow at point (5). At the coercive field, a zero net polarization state is attained (point (6)). When the field is increased in the negative direction, in the limit of an appropriately oriented single crystal, a new single domain state will be achieved (point (7) and (8)).[(5)(6)(7)]

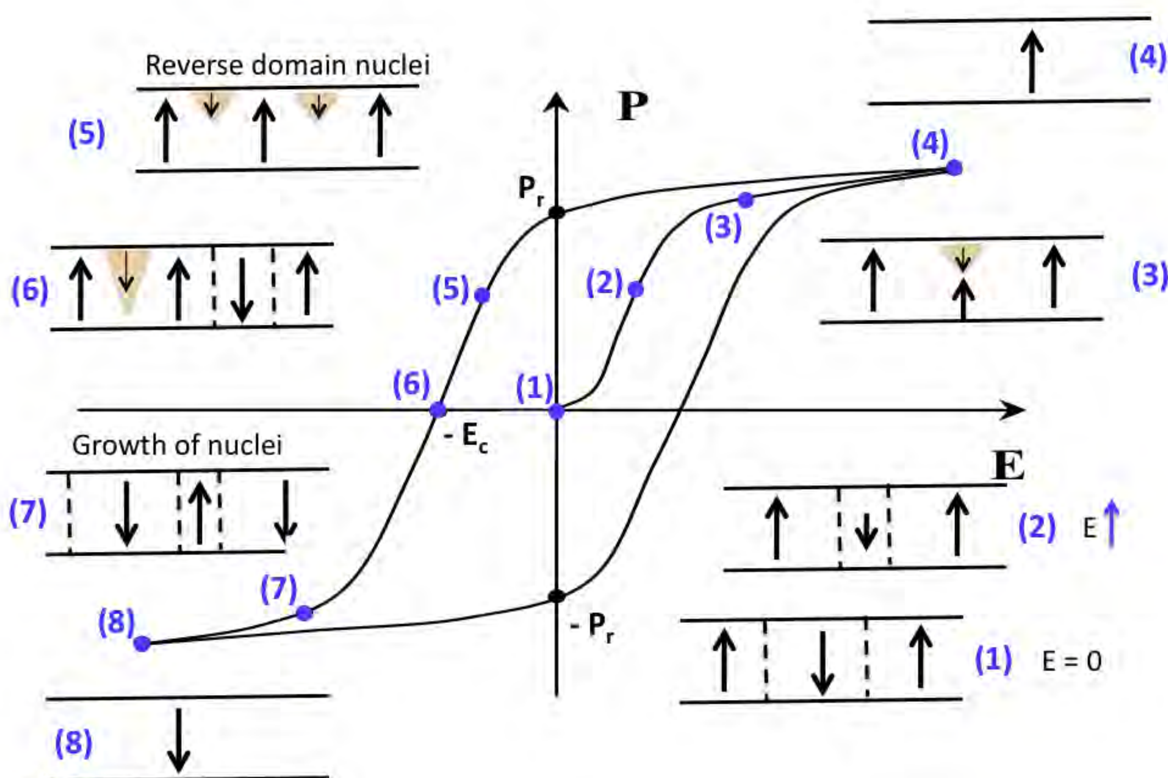

Figure 2.7. Schematic showing the relation between a P-E loop and domain configurations at selected points in a uniaxial ferroelectric single crystal. [(7)]

2.3 Ferroelectric Domain Structure and Formation

Below the phase transition temperature (T_c), ferroelectric materials like $BaTiO_3$ develop a dipole moment that results from the displacement of the relative position of the oxygen octahedra and the central atom, as mentioned in section 2.2. A volume in which all dipole moments are aligned in the same direction (or nearly so) is called a domain; the interface between two domains is called a domain wall. The polarization directions can vary depending on the crystal system as shown in Figure 2.8 and summarized in Table I.

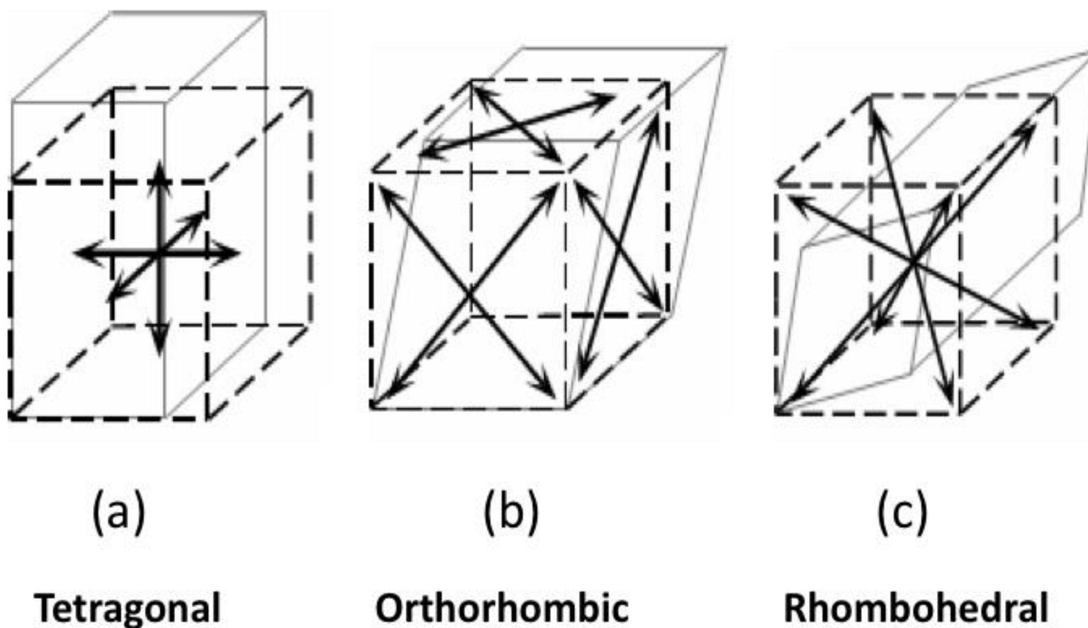

Figure 2.8. Possible polarization directions referenced to the cubic prototype for (a) tetragonal perovskite with 6 equivalent <001> directions, (b) orthorhombic distortion with 12 equivalent <110> directions, or (c) rhombohedral with 8 equivalent <111> directions. [7][8][9][10][11]

Table 2.1. Possible polarization directions in a perovskite relative to the cubic prototype cell

Crystal system	Polarization direction	Number of equivalent directions
Tetragonal	<100>	6
Orthorhombic	<110>	12
Rhombohedral	<111>	8

Also, the types of domain wall that can be formed depend on the crystal structure and symmetry of a material. For example, in a rhombohedral perovskite ferroelectrics, 180°, 71° and 109° domain walls are allowed as shown in Figure 2.9. Figure 2.10 shows a schematic representation of the available polarization directions of a rhombohedral perovskite. (7)(8)(9)(10)(11)(12)

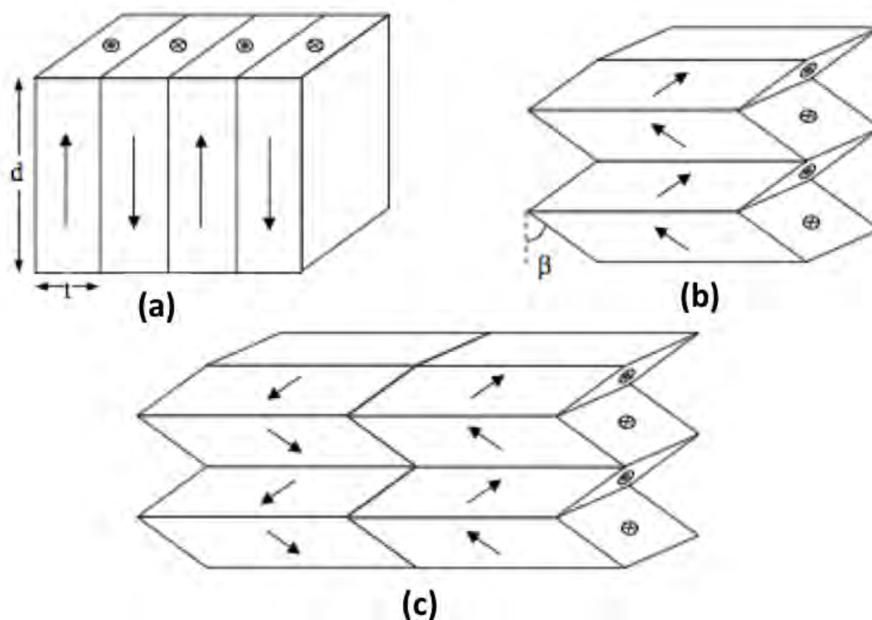

Figure 2.9. Schematic diagrams of (a) 180° domain walls and (b) non-180° domain walls and (c) a mixed domain structure in a ferroelectric crystal (from reference [7]).

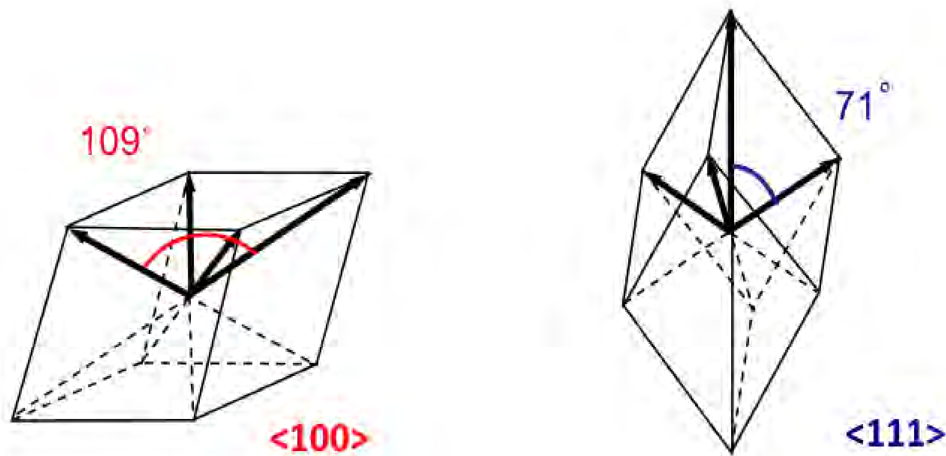

Figure 2.10. Illustration of the possible polarization directions in a rhombohedral perovskite. (Only the upward polarization directions are indicated) (from reference [7]).

In the tetragonal perovskite structure like $BaTiO_3$, there are 6 possible directions of the spontaneous polarization and the available domain walls can be 180° or 90° walls, as shown in Figure 2.11. 180° walls are separated by domains which have oppositely oriented polarization directions; 90° walls separate regions with perpendicular polarization directions.(14)(15) 90° domain walls can be the consequence of mechanical constraints related to the stresses induced by the ferroelectric phase transition. In this case, the non-180° domain walls act to minimize the elastic energy as shown in Figure 2.11. The net driving force for the formation of domains and domain walls in ferroelectric materials is minimization of the electrostatic energy of the depolarizing field (E_d), and the elastic energy related to the mechanical strains, including those created by the phase transition.(11)(12)(13)(14)(15)

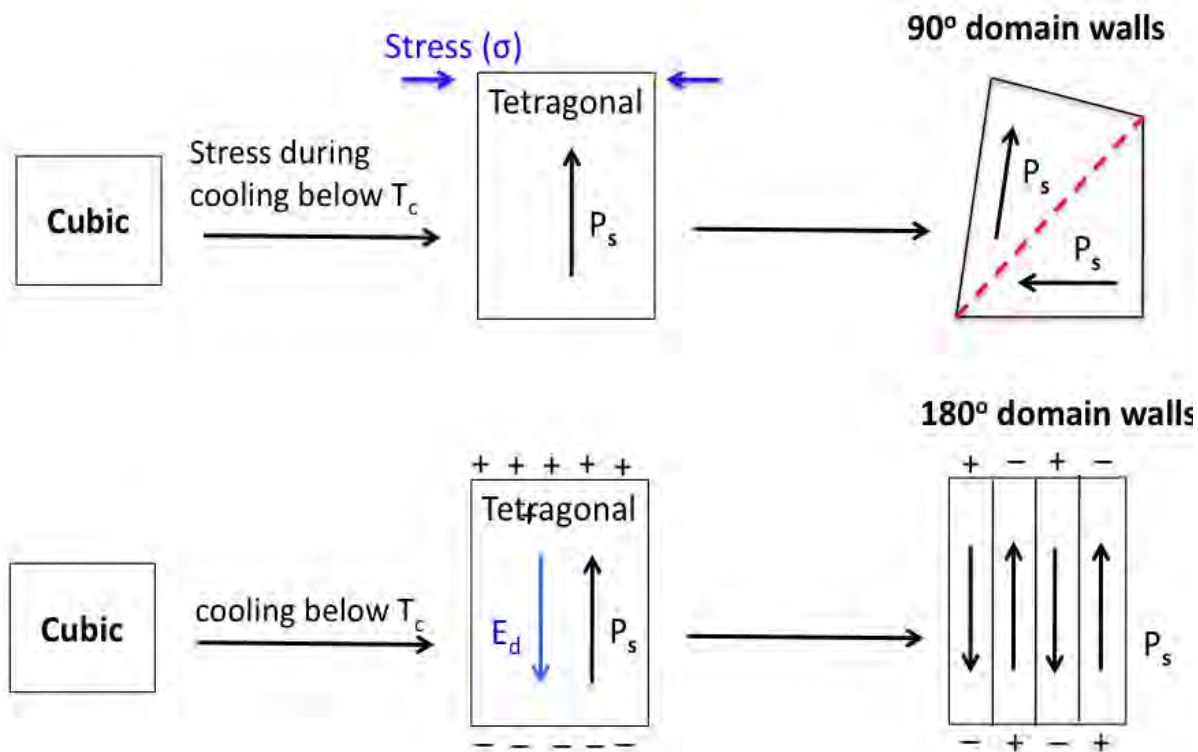

Figure 2.11. Schematic illustration of 180° and 90° domain walls in the tetragonal perovskite crystal like $BaTiO_3$ (E_d: the depolarizing field, P_s: spontaneous polarization) (modified from reference [13])

2.4. Lead Zirconate Titanate (PZT)

The $PbZrO_3$-$PbTiO_3$ phase diagram is shown in Figure 2.12. (3)(4)

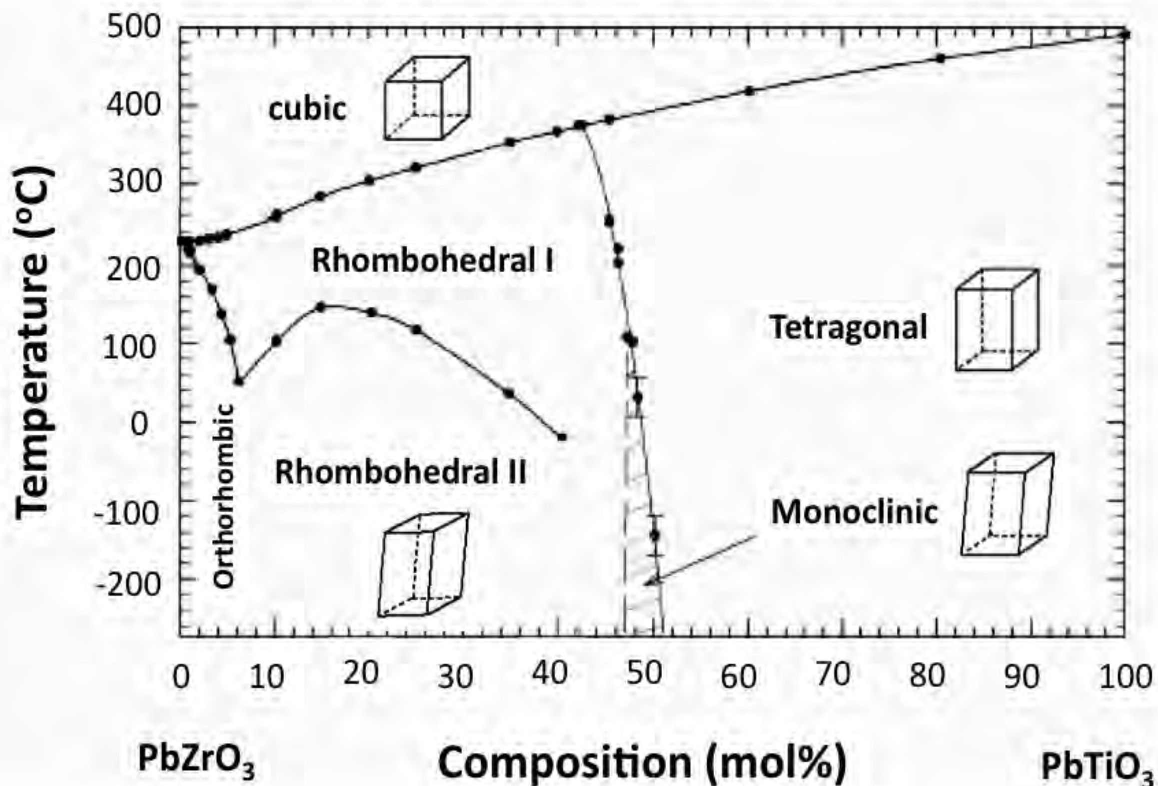

Figure 2.12. PZT phase diagram (established in Jaffe et al. (1971) [3] and Noheda et al. [8] (2000). The figure is modified from reference [3])

Above 230°C, $PbZrO_3$ is cubic and below this temperature, it undergoes a phase transition to an orthorhombic phase. On the other hand, $PbTiO_3$ is cubic above 490°C; below this temperature, it experiences a phase transition to tetragonal ferroelectric phase. Above the Curie temperature, PZT has a cubic unit cell and is paraelectric. The larger Pb cation and oxygen anions form a face-centered cubic lattice and the smaller Ti and Zr occupy the octahedral site in the cubic lattice. On cooling through the Curie temperature, it experiences a phase transition from the cubic structure (paraelectric state) to a tetragonal one for titanium-rich compositions and a rhombohedral one for zirconium-rich compositions (ferroelectric state).(3)(4)

The piezoelectric and dielectric properties of both bulk and film PZT peak at a Zr/Ti ratio of 52/48. In Figure 2.12, the morphotropic phase boundary (MPB) is the abrupt structural change with composition near the Zr/Ti ratio of 52/48. For MPB compositions, the composition dependence of the dielectric and piezoelectric properties of PZT is shown in Figure 2.13. (3)(4)(5)(16) At the MPB, there is a peak of dielectric constant and piezoelectric properties of PZT as calculated by Haun et al..(3)(17) The large dielectric and piezoelectric properties near the MPB make PZT very attractive candidate for electronic devices.

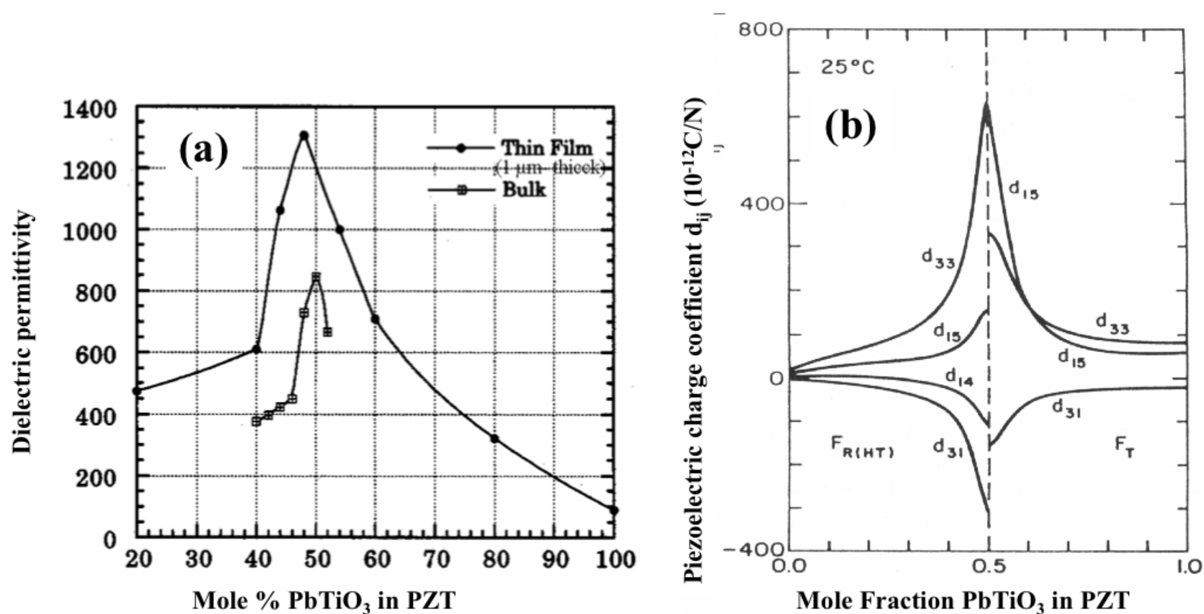

Figure 2.13. Composition dependence of (a) the dielectric constant and (b) the piezoelectric charge coefficient of PZT (from references [16][17])

2.5. Intrinsic and Extrinsic Contributions to the Dielectric and Piezoelectric Response

In general, the dielectric and piezoelectric properties of ferroelectric materials are dependent on both intrinsic and extrinsic contributions. The intrinsic contributions are the result of an average of the response of single domains present in the material. Changes in the polarization of the unit cell lead to a change in the unit-cell volume. The extrinsic contribution is associated with the motion of domain walls and/or phase boundaries under an applied electric field.[18][19] As a result of extrinsic contributions, the dielectric and piezoelectric response of ferroelectric materials depend on the magnitude of the applied electric field and frequency. The field amplitude dependence of the response of dielectric permittivity has been studied and reported by several researchers to analyze the intrinsic and extrinsic contributions.[18][20] At small ac electric fields, the relative dielectric permittivity ε_r, is dominated the intrinsic contribution and reversible domain wall motion .[21][22] When the ac field is increased, the dielectric permittivity of ferroelectric materials often becomes a function of the electric field, as shown in Figure 2.14. [22] This phenomenon is called dielectric nonlinearity, and is due to extrinsic behavior. The extrinsic contribution, which is associated with the interaction of domain walls or phase boundaries with pinning centers in the material, is a significant part of dielectric and piezoelectric response in bulk ferroelectric materials. Domain wall movement produces both hysteretic and nonlinear behavior polarization or strain behavior. The dielectric and piezoelectric nonlinearity of ferroelectric materials under an ac electric field magnitude higher than the threshold field (E_{th}) can be quantified and explained by using the Rayleigh law. [7][20]

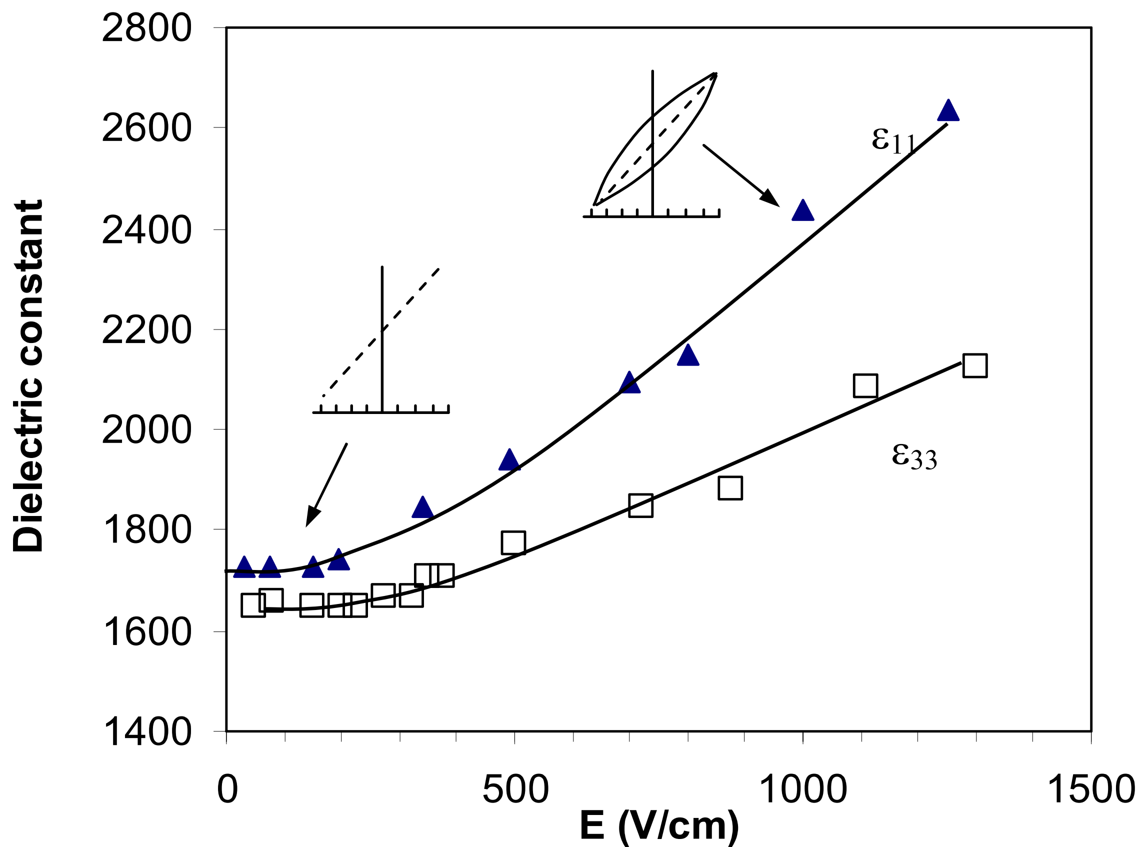

Figure 2.14. The dielectric nonlinearity ε_{11} and ε_{33} under an application of AC field in soft PZT ceramics, after Li et al. (taken from reference [22])

2.6. Rayleigh Law

The Rayleigh law, first developed for ferromagnetic materials to explain the nonlinear response of the magnetization to an applied magnetic field, can be used to describe the field dependence of the dielectric and piezoelectric properties in many ferroelectric materials.(23) In reality, there are plenty of defects in real ferroelectric materials, so that moving domain walls interact with pinning centers.(24) This is depicted schematically in Figure 2.15, where the domain

wall travels a potential energy landscape with some potential wells, which is controlled by the local distribution of elastic and electric fields. When the applied electric field is small, the domain wall can be moved moderately, but cannot go beyond an energy barrier. (25)(26)(27)

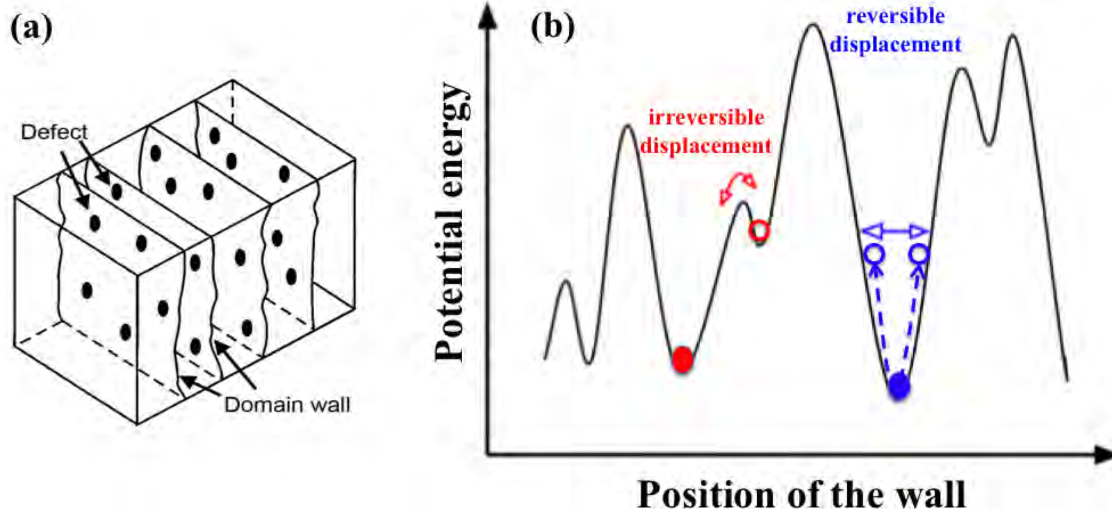

Figure 2.15. Illustration of (a) the interaction of domain walls with randomly distributed pinning centers and (b) the corresponding energy profile associated with the domain wall position. (taken from reference [27])

Therefore, the domain wall will return to its original position when the electric field is removed. This corresponds to a linear dielectric or strain response due to reversible domain wall motion. At higher fields, the domain wall exceeds the energy barrier and hops to another well, increasing the dielectric or piezoelectric constants due to irreversible domain wall motion. At still higher fields, the dielectric and piezoelectric response become super or sub linear due to nucleation and growth of new domains. In many cases, for fields up to ~ 1/3-1/2 of the coercive

field, the properties are a linear function of the amplitude of the ac field. This corresponds to the Rayleigh regime expressed (for the dielectric response) by: [7][20]

$$e_r = e_{init} + a_r E_0 \qquad \text{Equation (2.6)}$$

$$P(E) = (e_{init} + a_r E_0) \pm \frac{a_r}{2}({E_0}^2 - E^2) \qquad \text{Equation (2.7)}$$

where ε_r is the real component of the dielectric permittivity, ε_{init} is the reversible Rayleigh coefficient, which is due to the intrinsic lattice and reversible domain wall motion. α_E is the irreversible Rayleigh coefficient, which is due to the irreversible domain wall or phase boundary movement. P is the measured dielectric polarization, and E_0 is the amplitude of the driving field.

Figure 2.16 shows three main zones in the dielectric permittivity (or piezoelectric coefficient) as a function of AC electric field.[29]

1. **Low field region**: the dielectric permittivity is constant under an application of low electric field.
2. **Rayleigh region**: the dielectric permittivity corresponds to the applied electric field linearly at the sub - switching field (intermediate field), which often extends to ~ 1/3-1/2 of the coercive field.
3. **High field region**: the dielectric permittivity become nonlinear because of the onset of polarization switching.

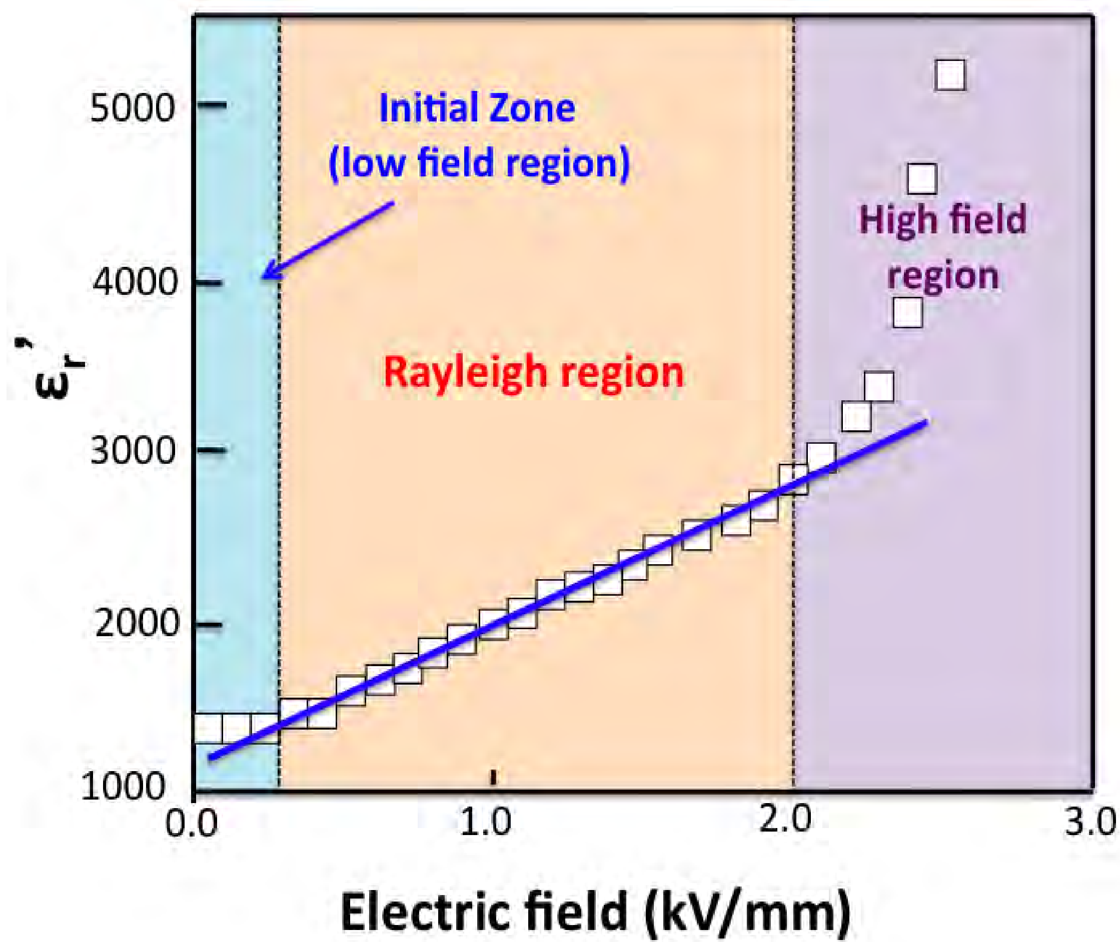

Figure 2.16. Illustration of the AC field dependence of the dielectric permittivity of hard PZT ceramic (modified from reference [29])

2.7. References

1. R. E. Newnham, "Properties of materials: anisotropy, symmetry, structure," pp. 392. Oxford University Press: Oxford, NY, (2005).

2. J.F. Nye, *Physical properties of crystals*, Oxford University Press, New York, NY, 1990.

3. Jaffe, B., Cook, W.R. & Jaffe, H. Piezoelectric Ceramics, (R.A.N., Ohio, 1971)

4. Moulson, A.J. & Herbert, J.M. Electroceramics, (Chapman & Hill, New York, 1990)

5. An American national standard IEEE standard definitions of terms associated with ferroelectric and related materials, IEEE Trans. Ultras. Ferro. Freq. Control, 50, pp. 1-32, (2003)

6. D. Damjanovic, "Ferroelectric, dielectric and piezoelectric properties of ferroelectric thin films and ceramics," *Rep. Prog. Phys.,* **61** [9] 1267-324 (1998).

7. N. B. Gharb, "Dielectric and piezoelectric nonlinearities in oriented $Pb(Yb_{1/2}Nb_{1/2})O_3$-$PbTiO_3$ thin films," PhD thesis in Materials Science and Engineering, the Pennsylvania State University (2005).

8. B. Noheda, J. A. Gonzalo, L.E. Cross, R. Guo, S. E. Park, D.E. Cox, G. Shirane, "Tetragonal-to-monoclinic phase transition in a ferroelectric perovskite: The structure of $PbZr_{0.52}Ti_{0.48}O_3$," *Phys Rev. B*, vol. 61, pp. 8687 -8690 (2000)

9. A. F. Devonshire, "Theory of ferroelectrics," Adv. in Physics, vol. 3, pp. 85-130 (1954)

10. R. G. Polcawich, "Design, fabrication, test, and evaluation of rf MEMS series switches using lead zirconate titanate (PZT) thin film actuators," PhD thesis in Material Science and Engineering, the Pennsylvania State University (2007).

11. W. L. Warren, J. Robertson, D. Dimos, B. A. Tuttle, G. E. Pike, and D. A. Payne, "Pb displacements in $Pb(Zr,Ti)O_3$ perovskites," Phys. Rev. B, vol. 53, pp. 3080 –3087 (1996).

12. R.V. Wang, D.D. Fong, F. Jiang, M.J. Highland, P.H. Fuoss, C. Thompson, A.M. Kolpak, J.A. Eastman, S.K. Streiffer, A.M. Rappe, G.B. Stephenson, Reversible chemical switching of a ferroelectric film. Phys. Rev. Lett. **102**, 047601 (2009)

13. Dragan Damjanovic, " Chapter 4. Hyesteresis in piezoelectric and ferroelectric materials", The Science of hysteresis, Volume 3; I. Mayergoyz and G.Bertotti (Eds.); Elsevier (2005)

14. L.E. Cross, "Ferroelectric ceramics: Tailoring properties for specific application," in the book of Ferroelectric Ceramics; tutorial review, theory, processing, and applications, pp. 1-85, edited by N. Setter and E. Collar, Birkhauer Verlag Basel (1993)

15. E. J Bondarenko, V.Y.Topolov and A.V. Turik, “The role of 90 degrees domain wall displacements in forming physical properties of perovskite ferroelectric ceramics, “Ferro. Lett. Sect., 13, 13, (1991)

16. H. D. Chen, K. R. Udayakumar, C. J. Gaskey, and L. E. Cross, "Electrical properties' maxima in thin films of the lead zirconate-lead titanate solid solution system," Appl. Phys. Lett., **67** [23], pp. 3411-13 (1995)

17. M.J. Haun, E. Furman, S. J. Jang and L.E. Cross, “Thermodynamic theory of the lead zirconate titanate solid solution system, part I: Phenomenology,” Ferroelectrics, Vol. 99, Issue 1, pp. 13-25 (1989)

18. B. Lewis, “Energy loss processes in ferroelectric ceramics,” Proc. Phys. Soc. (London), Vol. 73, No. 1, pp. 17-24 (1958)

19. D. Damjanovic and M. Demartin, “Contribution of the irreversible displacement of domain walls to the piezoelectric effect in barium titanate and lead zirconate titanate ceramics,” J. Phys. Condens. Matter **9, pp.** 4943-4953 (1997)

20. Nazanin Bassiri-Gharb, Ichiro Fujii, Eunki Hong, Susan Trolier-McKinstry, David V. Taylor, and Dragan Damjanovic, “Domain wall contributions to the properties of piezoelectric thin films”, J Electroceram. 19, pp. 47–65 (2007)

21. M.E. Lines, A.M. Glass, “Principles and applications of ferroelectrics and related materials,” (Oxford University Press, New York, 1977)

22. S. Li, W. Cao, L.E. Cross, “The extrinsic nature of nonlinear behavior observed in lead zirconate titanate ferroelectric ceramic,” J. Appl. Phys. 69, pp. 7219-7224 (1991)

23. Lord Rayleigh, “Notes on electricity and magnetism: on the behavior of iron and steel under the operation of magnetic forces,” Phil. Mag. 5, pp. 225-245, (1887)

24. C. Ang and Z. Yu, “Dielectric behavior of $PbZr_{0.52}Ti_{0.48}O_3$ thin films: Intrinsic and extrinsic dielectric response,” Appl. Phys. Lett., 85, pp. 3821-3823 (2004)

25. D.V. Taylor and D. Damjanovic, “Domain wall pinning contribution to the nonlinear dielectric permittivity in Pb(Zr, Ti)O_3 thin films, “Appl. Phys. Lett., 73, pp. 2045-2047, (1998)

26. F. Xu, S. Trolier-McKinstry, W. Ren, B. Xu, Z.L. Xie, K.J. Hemker, “Domain wall motion and its contribution to the dielectric and piezoelectric properties of lead zirconate titanate films,” J. Appl. Phys. 89, pp. 1336-1348 (2001)

27. Ichiro Fujii, "Dielectric nonlinearity of ferroelectrics”, PhD thesis in Materials Science and Engineering, the Pennsylvania State University (2010)

28. D. Damjanovic, "Nonlinear piezoelectric response in ferroelectric ceramics," pp. 125-35 in *Piezoelectric materials: advances in science, technology, and applications*. *NATO science series. Series 3, High technology* edited by C. Galassi, M. Dinescu, K. Uchino, and M. Sayer. (Kluwer Academic Publishers, Dordrecht, 2000)

29. D.A. Hall and P.J. Stevenson, "High field dielectric behavior of ferroelectric ceramics," Ferroelectrics, 228, 139, (1999)

Chapter 3

Effect of Feature Size on Dielectric Nonlinearity of Serpentine Patterned $PbZr_{0.52}Ti_{0.48}O_3$ Films

3.1. Abstract

Lead zirconate titanate, PZT (52/48) thin films with a $PbTiO_3$ seed layer were patterned into features of different widths, including various sizes of squares and 100 μm, 50 μm and 10 μm serpentine designs, using argon ion beam milling. Patterns with different surface area/perimeter ratios were used to study the relative importance of damage produced by the patterning. It was found that as the pattern dimensions decreased, the remanent polarization increased, presumably due to the fact that the dipoles near the feature perimeter are not as severely clamped to the substrate. This investigation is in agreement with a model in which clamping produces deep wells, which do not allow some fraction of the spontaneous polarization to switch at high field. The domain wall mobility at modest electric fields was investigated using the Rayleigh law. Both the reversible, ε_{init}, and irreversible, α, Rayleigh coefficients increased with decreasing serpentine line width for de-aged samples. For measurements made immediately after annealing, ε_{init} of 500 μm square patterns was 1510 ± 13; with decreasing serpentine line width, ε_{init} rose from 1520 ±10 for the 100 μm serpentine to 1568 ± 23 for the 10 μm serpentine. The irreversible parameter, α, for the square patterns was 39.4 ± 3.2 cm/kV and it increased to 44.1 ± 3.2 cm/kV as the lateral dimension is reduced. However, it was found that as the width of the serpentine features decreased, the aging rate rose. These observations are consistent with a

model in which sidewall damage produces shallow wells that lower the Rayleigh constants of aged samples at small fields. These shallow wells can be overcome by the large fields used to measure the remanent polarization and the large unipolar electric fields typically used to drive thin film piezoelectric actuators.

The majority of this chapter is reproduced from J. I. Yang, R. G. Polcawich, L. M. Sanchez, and S. Trolier-McKinstry (published in the Journal of Applied Physics, 117, 014103 (2015)

3.2. Introduction

Ferroelectric materials such as lead zirconate titanate ($Pb(Zr,Ti)O_3$, PZT) have been researched extensively for devices such as capacitors, transducers, actuators, sensors and nonvolatile memories. [(1)(2)(3)] In many cases, fabrication of these devices requires that the ferroelectric layer be laterally patterned. Several etching methods have been utilized, including ion beam milling (IBE) [(4)], reactive ion etching (RIE) [(5)(6)(7)], wet chemical etching [(8)], inductively coupled plasma etching [(9)], etc.

However, some patterning processes induce damage that affects the electrical and piezoelectric properties. For example, according to Pan *et al.*, RIE damage of Pt/PZT/Pt is due to a combination of surface contamination and displacement damage from the ion bombardment. As a result, the hysteresis loop shifted after etching due to internal field development, reducing the remanent polarization.[(10)(11)] Stanishevsky *et al.* indicated that there can be a significant modification in the chemical composition of the damage layer due to loss of lead and oxygen, ion implantation, and amorphization of material.[(12)] Soyer *et al.* evaluated the surface damage PZT due to Ar ion bombardment.[(13)(14)]

There are also numerous reports on minimization of etch-induced damage. For example, Desu *et al.* report that the damaged layer produced by dry etching process of a ferroelectric capacitor acts as a voltage drop layer.[(15)] Treatment of the damaged layer using an oxygen RF-plasma reduced the leakage currents. Similarly, Torii *et al.* compared the leakage current densities between micron-size capacitors and larger ones.[(16)] It was shown that as the capacitor perimeter increased, the leakage current density increased due to leakage along the damaged capacitor sidewall. Lee *et al.* showed that the leakage current, remanent polarization and coercive field could be improved by eliminating the etch-induced damage layer using wet cleaning.[(17)]

Control of etch damage is also important in manufacture of ferroelectric film devices. For example, Tegal Corporation introduced a capacitively coupled high density plasma etch reactor for PZT stack etch to overcome ion milling limitations. Their method is characterized by a low removal rate of platinum (~400Å/min) and induced residues due to re-deposition of etched materials along the edge of the etch mask and veils or fences after the etch mask is removed. They reported that the platinum and PZT etch rates improved using the high density plasma etch reactor (~1000Å/min) and that good etch profiles with no post-etch residue could be produced.[(18)] Also, Toshiba Corp. Semiconductor Company and Infineon Technologies NA Corporation showed high temperature plasma etching processes of PZT capacitor stack for high density FERAMs. They obtained highly anisotropic etch profiles, with low re-deposition and good uniformity, while eliminating micromasking effects through control of etching temperature and gas chemistries.[(19)] These results are summarized in Table 3.1.

The observed properties as a function of feature size are expected to be influenced both by any local electric/elastic fields induced by the patterning, and by the progressive elimination of clamping imposed by the substrate.[(20)] To date, comparatively less information on how patterning affects the low and intermediate field properties of ferroelectrics is available. Therefore, the goal of this research is to understand how and why the electrical properties of PZT thin films patterned by Argon ion milling is influenced by lateral feature size. The competition between clamping and sidewall damage are assessed via measurements of the dielectric and ferroelectric properties.

Table 3.1. Reported approaches for etching of ferroelectric films

Reference	Material	Patterning method	Post-etch treatment	Conductivity	Ferroelectric properties	Comments
Pan *et al.* [10][11]	Pt/PZT/Pt	Reactive ion etching using Ar and $CHClFCF_3$ etch gases with RF power of 150 W and the chamber pressure between 50 mTorr and 125 mTorr	Thermal annealing at 400°C for 30min in oxygen	Leakage current increased after etching	P_r decreases after etching	The reduction of P_r is attributed to an internal field development due to positive ion bombardment and charge accumulation.
Stanishevsky *et al.* [12]	Pt/LSCO/PZT/ LSCO/Pt	Focused ion beam	Thermal recovery annealed at 650°C for 1h in oxygen	Leakage current decreases after annealed		
Torii *et al.* [16]	Pt/PZT/Pt	Single photolithography process, Top and bottom Pt electrode etched by Ar-sputter etching and PZT dry etched with CF_4-Ar mixture	Oxygen RF –plasma	Leakage current decreases after oxygen plasma treatment		Incomplete recovery reported
Lee *et al.* [17]	Pt/PZT/Pt	Tegal dry etcher with a Ar-Cl_2-C_2F_2 gas mixture	Cleaning in a mixture of acetic acid, hydrofluoric acid, and ethanol	Leakage current decreases after wet cleaning	E_c decreases	The wet clean-up etch may change the etch profile and the lateral dimension of the pattern

Reference	Material	Patterning method	Post-etch treatment	Ferroelectric properties	Comments
Liang *et al*. [21]	$LaNiO_3$/PZT/Pt	Focused ion milling of amorphous precursor film		E_c decrease as the island size decreases after FIB of amorphous PZT film	FIB etching before PZT crystallization
Lee *et al* [22]	Pt/PZT/Pt	Reactive ion etching with Ar for sputtered top Pt electrode	Annealed at 600°C and 700°C temperature	Good symmetrical P-E loop at annealed 600°C and 700°C	The voltage shift and the deformation of polarization are caused by charge trapping at electrode interfaces and at defect levels in the film
Kim *et al*. [23]	Pt/PZT/Pt	A planar inductive coupled plasma (ICP) with Cl_2/CF_4/Ar and $Cl_2/CF_4/O_2$ gas mixture	Thermal annealed 600°C for 30min under the oxygen atmosphere with $Cl_2/CF_4/O_2$ gas mixture	Degraded the remnant polarization	Cl_2/ CF_4/Ar plasma, the etching damage cannot be recovered by the O_2 annealing.
Chung *et al*. [24]	Pt/RuOx/PZT/Pt/ RuOx	Inductively coupled plasma (ICP) with $Cl_2/C2F_6$/Ar gas at coil power of 400 W, dc-bias voltage of 300W	Thermal annealing at 550°C for 15 min in O_2	Hysteresis loop shifted and internal field increased	After heat treatment, the trapped charges near PZT surface are released

3.3. Experimental Procedure

3.3.1. Chemical Solution Deposition Processing

10% Pb excess 0.4 M $Pb(Zr_{0.52}Ti_{0.48})O_3$ (PZT) and 30% Pb excess 0.15 M $PbTiO_3$ solutions were used to grow films using chemical solution deposition (CSD). Typically, a 30% lead (Pb)-excess $PbTiO_3$ solution is fabricated to serve as the seed layer for PZT. 10% Pb excess 0.4 M $Pb(Zr_{0.52}Ti_{0.48})O_3$ (PZT) and 30% Pb excess 0.15 M $PbTiO_3$ solutions were synthesized using a modification in a process originally reported elsewhere.[(25)] A measured amount of lead (III) acetate trihydrate (Puratronic) was mixed with 150 mL of 2-methoxyethanol (2-MOE) (Sigma Aldrich). It was refluxed at 120°C for 20 minutes in a Heidolph Laborata 4000 rotary evaporator with flowing nitrogen (N_2). Vacuum distillation was performed in the rotary evaporator to remove impurities at a pressure between 260-330 mbar, until a white foam appeared. While the lead (III) acetate trihydrate and 2-MOE mixed in the rotary evaporator, Titanium n-isopropoxide (70 wt% in n-propanol) (Alfa Aesar) was dissolved in 2-MOE on a magnetic stirrer. Once the Pb solution finished the vacuum distillation step, the Ti solution was combined with the Pb solution and was allowed to reflux for 210 minutes. A second vacuum distillation at 925 mbar was performed followed by a N_2 purge. The solution was transferred to a storage container where 4 volume% formamide was slowly added to the solution to act as a drying control agent. The final solution was stirred overnight on a magnetic stirrer and 7 volume% of acetic acid was added to the solution once ready for use. The 10% Pb-excess PZT (52/48) was also fabricated in a similar process except that the zirconium (IV) n-propoxide precursor (Alfa Aesar) was added to the titanium (IV) n-isopropoxide and 2-MOE mixture.

3.3.2. Deposition and Crystallization of PZT Thin Film with a PT Seed Layer

To obtain films, the solution was spin coated on platinized silicon substrates with 500nm thermal oxide elastic layer underneath the electrode. Approximately 30 nm of Ti was sputtered onto the wafer using the Unaxis Clusterline 200 deposition system at 40°C. The wafer was then furnace annealed at 750ºC in a Bruce Technologies tube furnace in 10 SLM flowing oxygen for 30 minutes. The resulting TiO_2 film was approximately 36 nm thick. Following this, 100 nm Pt was sputtered at 500ºC for use as a bottom electrode. Finally, a $PbTiO_3$ solution was deposited to improve orientation, as reported elsewhere.(26) The film was pyrolyzed on a hotplate at 350°C for 120 s. An A.G. Associates 610 rapid thermal anneal (RTA) furnace was used for the crystallization at 700°C for 60 s in 7-9 sccm of oxygen with a heating ramp rate of ~200ºC/second in order to produce a seed layer ~20 nm in thickness. PZT solution was spin-coated on the $PbTiO_3$ seed layer at 2000 rpm for 20 s. The PZT film was pyrolyzed at 350°C for 120 s and crystallized at 700°C for 60 s in the RTA with a heating ramp rate of ~200ºC/second. Deposition, pyrolysis, and crystallization steps were repeated until a film thickness of approximately 500nm was achieved. Platinum top electrodes with a thickness of ~100nm were deposited onto the PZT surface by a Unaxis Clusterline 200 (CLC) sputter deposition system with a substrate temperature of 350 ^{o}C. To improve adhesion of the platinum and minimize any sputtering-induced damage, the wafers were annealed using the RTA at 350°C for 2 minutes in flowing O_2.

3.3.3. Patterning and Etching Process of PZT with PT Seed Layer Thin Film

After the film deposition, patterning was done by surface micromachining; the process flow is shown in Figure 3.1. The patterning process for the top electrode and the PZT was achieved using a 2 μm thick layer of Clariant AZ 5214E resist which was spread for 5 s at 500

rpm, spun for 40 s at 2000 rpm using an EVG 120 automated resist processing system, and cured at 110°C for 60 s. The photoresist was exposed for 3.2 seconds in a Karl Suss MA/BA6 contact aligner and subsequently developed in the EVG 120 using AZ 300MIF developer for 90 s. After the photolithography was completed, the wafers were exposed to a low-power 200 sccm O_2 plasma for 5 min at pressure 525mT and power 200W in Metroline/IPC plasma photoresist stripper to remove any resist residues. Afterwards, the resist was UV hardened at 220°C and 275 mW/cm^2 using an Axcelis UV photostabilizer.

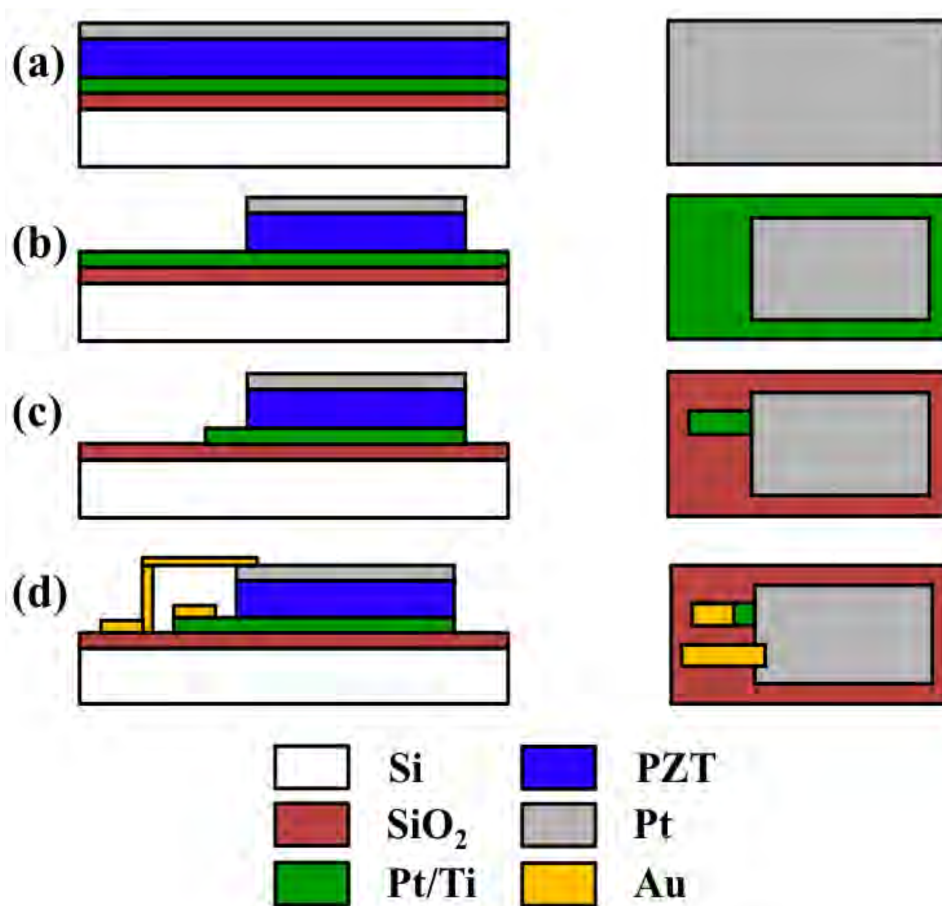

Figure 3.1. Fabrication process flow of 0.5 μm patterned PZT (52/48) with $PbTiO_3$ seed layer (right side is cross-section view and left side is top view).

The Ar ion-milling was accomplished with a combination of a high power etch and a dual angle low power etch. The, 85° angle high power etch is used to etch through a bulk of the material and the 50° dual angle low power etch is used for 30-50 s to clean up the sidewalls of the etched material. The conditions of each Ar ion-milling step are described in Table 3.2.

Table 3.2. Parameters used for ion-milling PZT and Pt

Items	High power etch	Low power etch
Beam voltage	650 V	400 V
Beam current	700 mA	400 mA
Acceleration voltage	195 V	150 V
N_2 – Ar flow	20.85 sccm	20.85 sccm
Keeper current	1.5 A	1.5 A
Cathode current	0.5 A	0.5 A
Cathode Ar flow	13.9 sccm	13.9 sccm
Spin speed	5 rpm	5 rpm

After ion-milling, the resist mask was removed in a Metroline / IPC plasma photoresist stripper using an O_2 plasma for 20 min at a pressure of 1000 mTorr and a power of 400W, followed by a wet clean in DI water using an ultrasonic bath to remove residues from the wafer surface. To minimize parasitic bond pad capacitance, metal traces consisting of Au/Pt/Ti (730nm/20nm/20nm) were routed on the exposed SiO_2. A gold air bridge was used to make contact from the top Pt electrode to the metal traces. To fabricate the air bridges, a photoresist sacrificial layer was patterned. Next, a 2 µm thick Au layer was deposited via electron beam evaporation with a Evatech BAK 641 electron Beam evaporator and patterned via a liftoff technique with acetone. For the sake of assessment of the relative importance of declamping and

etch damage on the evolution of the film properties with lateral feature sizes, four different patterns were made in this study as shown in Figure 3.2: a 500 μm square, as well as 100 μm, 50 μm, and 10 μm wide serpentines. All patterns were designed to have the same surface area of 2.5×10^{-3} cm^2. The measured surface areas (which in fact varied very little) were used to calculate the dielectric and ferroelectric properties after patterning; the different geometries allow the electrode area/perimeter ratio to be changed by a factor of 13 while the film microstructure is held constant. In this way, it is possible to assess the relative importance of changes in the stoichiometry/crystallinity of the sidewalls in influencing the relative mobility of domain walls in the patterned features.

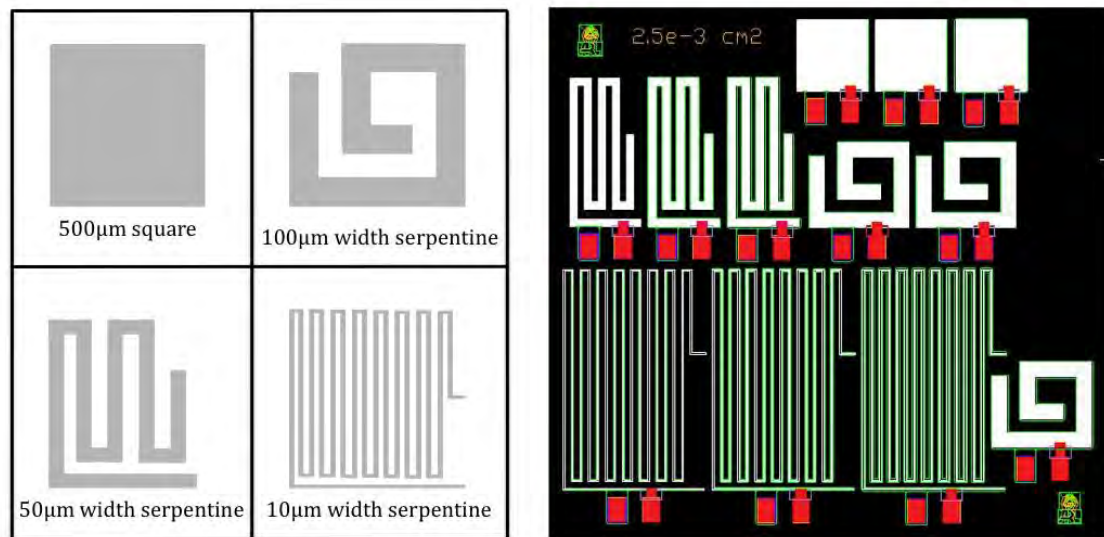

Figure 3.2. Device layout of patterned 0.5 μm thick PZT (52/48) with $PbTiO_3$ seed layer.

3.3.4. Structural and Microstructural Characterizations

Patterned PZT thin films were characterized using x-ray diffraction (Panalytical X'pert Pro MPD) to study the orientation of the perovskite phase. All of the microstructure images in

this chapter were taken on a Leo 1530 field emission scanning electron microscope. The range of an accelerating electric voltage was 3-5 kV with 2-5 mm of working distance. Image J software was used to calculate the average grain size.

3.3.5. High and Low Field Ferroelectric and Dielectric Characterization

Polarization – electric field hysteresis loop measurements were carried out an RT-66A Ferroelectric Test System (Radiant Technology, Inc.). The measurement frequency was 100 Hz and the applied voltage range from 5 to 35 volts. Low field measurements of the dielectric constant, loss tangents, Rayleigh parameter, and aging were measured using a Hewlett-Packard (4284A LCR meter) at a frequency of 10 kHz at 30mV.

3.4. Results and Discussion

Figure 3.3 shows the XRD pattern of the PZT(52/48)/$PbTiO_3$ film stack following an anneal at 550°C for 1min in O_2 to remove massive pinching in the hysteresis loop. The film shows strong {100} orientation. The films had Lotgering factors of 94% in the {100} orientation as calculated from a Bragg-Brentano θ-2θ pattern.

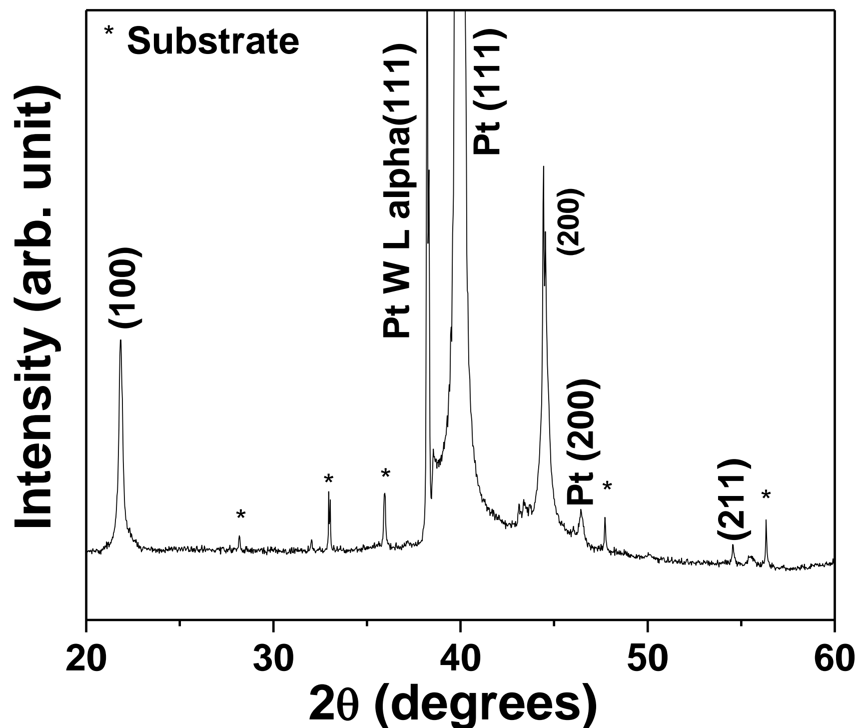

Figure 3.3. XRD patterns of 0.5 μm patterned PZT (52/48) with $PbTiO_3$ seed layer. The starred peaks arise from the substrate.

FESEM image were used to determine the sidewall angle and line width of the patterned PZT films. Figure 3.4 (a) and (b) show FESEM micrograph of a 10 μm serpentine patterned PZT (52/48) on a $PbTiO_3$ seed layer. Figure 3.4 (a) is the cross-sectional image and (b) top surface of a 10 μm serpentine. Under the aforementioned etching conditions, it is observed that the sidewall angle of all features is ~74°.

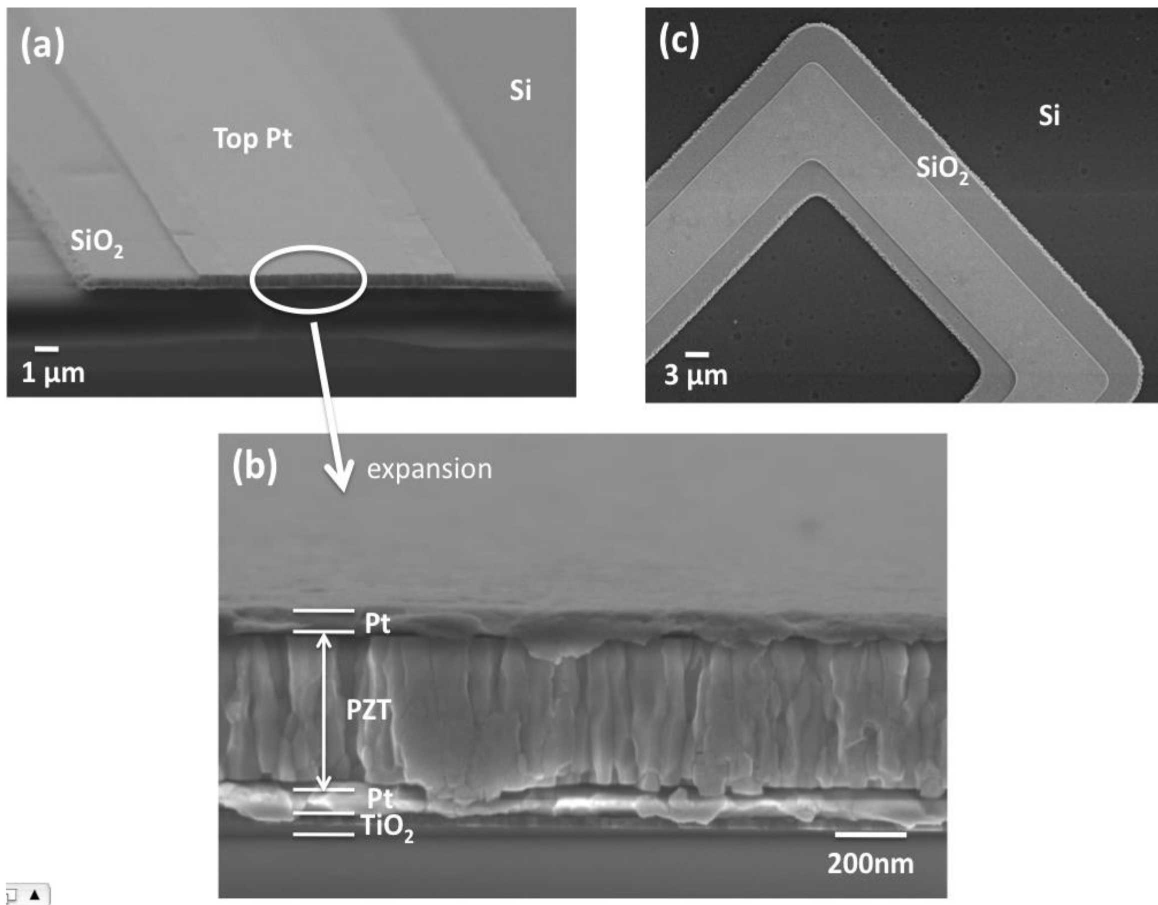

Figure 3.4. FESEM micrograph of a serpentine patterned PZT (52/48) on a $PbTiO_3$ seed layer (a) the cross-sectional image, (b) the expansion of the cross-sectional image and (c) top surface of 10 µm serpentine line width

The frequency dependence of the dielectric constant and dielectric loss of the film is shown in Figure 3.5 for different pattern geometries. All measurements were performed after annealing the samples at 550 ^{o}C for 1 minute in O_2. At low frequency, the measured dielectric constants are almost equivalent ($\varepsilon_r \sim 1300$). The apparent dispersion above 1 kHz is more obvious for the finer feature sizes. Electrically, an RC circuit characterized by its frequency f= 1/2π RC, where *R* is the resistance of the circuit and *C* is the capacitance of the PZT thin film. The resistance, *R*, of a

serpentine patterned PZT is given by R= ρ l/A where ρ are the electrical resistivity of the material, l is the length of the conductor and *A* is the cross-section area of the conductor respectively. The resistance ratio of 100 μm and 10 μm serpentine to square perimeter is 5.3 and 175.8 respectively. Therefore, features with decreasing serpentine line widths had larger resistances, and hence a lower RC time constant for the capacitors studied. This is an artifact associated with the comparatively higher resistance of the electrodes on the fine serpentine features. To avoid this, only permittivity measurements below ~ 10^4 Hz were utilized; loss tangents were utilized below 1 kHz only.

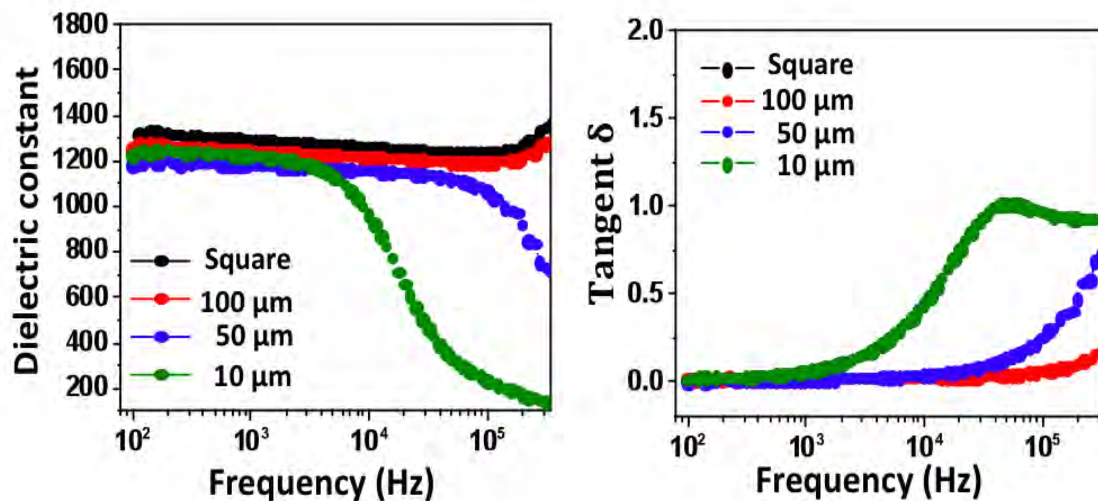

Figure 3.5. The frequency dependence of the dielectric constants and tangent loss for 0.5 μm PZT (52/48) with a $PbTiO_3$ seed layer. High frequency data for serpentine structures are contaminated by artifacts associated with the RC time constant for the capacitors studied.

It is hypothesized that any sidewall damage that produces pinning centers should influence the mobility of domain walls at sub-switching fields.[27][28] In order to assess this, the Rayleigh law was used to investigate the nonlinear dielectric response at low electric fields.[29][30][31] The irreversible Rayleigh constant is associated with motion of domain walls, so an increase should be tied to an increase either in the domain wall concentration or the domain wall mobility. After recovery annealing the samples at 550 ^{o}C for 1 minute in O_2, the Rayleigh parameters were immediately measured for different feature sizes at 100Hz in the unpoled state. Figure 3.6 (a) shows the resulting data averaged from 6 different samples for each type. It can be seen that ε_{init} of 500 μm square patterns is 1510 ± 13. With decreasing serpentine line width, ε_{init} increased from 1520 ± 10 for the 100 μm serpentine to 1568 ± 23 for the 10 μm serpentine. The irreversible parameter, α, for the square patterns is 39.4 ± 3.2 cm/kV and α increased from 40.3 ± 2.9 to 44.1 ± 3.2 cm/kV as the lateral dimension is reduced. Thus, immediately following a recovery anneal, both irreversible and reversible contributions to the permittivity increase on patterning. The percentage change in the irreversible coefficient is considerably larger than that in the reversible constant. This is presumably related to an increase in domain wall density or mobility, as described for released diaphragm structures.[32] Results presented in Figure 3.6 (a) suggest that the ratio of the irreversible to reversible Rayleigh parameters may increase slightly for the 10 μm serpentine after recovery annealing. The increase in the α value for 10 μm serpentine after recovery annealing can be attributed to a change in the potential energy profile due to the patterning by ion milling.

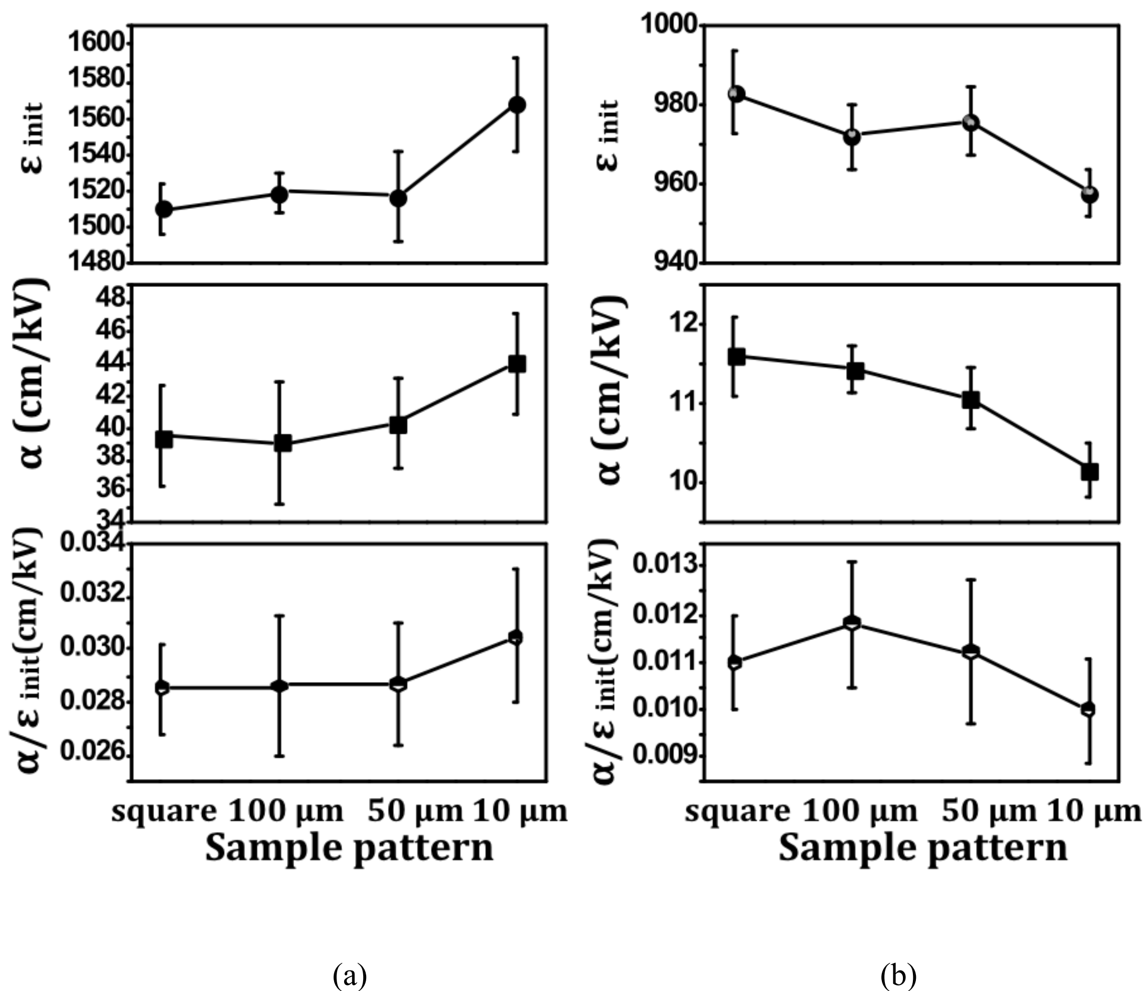

(a) (b)

Figure 3.6. Rayleigh parameter of a 0.5 μm thick patterned PZT (52/48) on a $PbTiO_3$ seed layer (a) after recovery annealing and (b) after aging for 9 months.

One question is why any change is observable in ε_{init} and α, given that the height:width aspect ratio of the smallest features is 1:20, i.e. comparatively large for purely a declamping effect. Nagarajan *et al*. showed that reduced clamping in discrete islands of a ferroelectric layer with an aspect ratio of 1:3 facilitated domain wall motion.[20] Bintachitt *et al.* demonstrated that in comparable PZT thin films, that domain walls moved in clusters, with a typical cluster size in

the range from 0.5 to 2 μm.[33] Griggio *et al.* reported that when a PZT film was declamped by removal of the substrate to make a suspended diaphragm, the extent of domain wall motion increased markedly, and that the clustering disappeared.[32] This suggests that the film-substrate interface provides a significant source of pinning for domain wall motion. Presuming an interaction width comparable to a typical cluster size, the volume of material that is influenced by the sidewalls would be somewhere between 10 and 40% of the PZT measured for the 10 μm wide serpentine. This would account for the observed changes.

In contrast, as shown in Figure 3.6 (b), the ε_{init} and α value of samples that were aged for 9 months after the recovery anneal *decreased* with decreasing serpentine line width. Among the possible mechanisms for aging are defect dipole reorientation,[34] space charge formation or redistribution [35] and drift of charge carriers [36][37] resulting in the stabilization of the domain structure corresponding to a lower domain walls motion. Data retention and imprint in nonvolatile memories with ferroelectric capacitors (FRAM) are also a function of the reliability and aging behavior of patterned devices. For example, Alexe *et al.* reported the development of a non-switchable polarization in the perimeter of PZT capacitors with decreasing feature size. They described the shift as being due to the pinning of ferroelectric domains at the free lateral surface and interface between ferroelectric and electrode.[38] Imprint and data retention difficulties in FRAM stem from stabilization of the domain state and immobility of domain walls because of trapped charge carriers, defect dipole complexes and space charge formation. [39] Here, it appears that the pinning centers produced by degradation of the PZT surface and/or sidewall damage is responsible for the difference in aging behavior.

To assess this, the Rayleigh behavior was tracked as a function of time to directly investigate aging of the dielectric response.[40][41] This measurement was performed at 100Hz

after recovery annealing the samples at 550 ^{o}C for 1 minute in O_2. It was found that the ε_{init} and α values aged more rapidly with decreasing serpentine line width as shown in Figure 3.7. Since all of the patterns came from one film (and therefore one microstructure and one set of processing conditions) this difference should be attributed to the longer perimeter formed during the etch process. Aging is a consequence of the gradual stabilization of the domain state in response to local elastic or electric fields. Etching relieves the global elastic constraints in the sidewall region, which would reduce the relative importance of pinning sites from the film-substrate interface. Thus, it is likely that the origin of the increased aging rate is domain pinning due to local non-stoichiometry or altered crystallinity at the sidewalls.

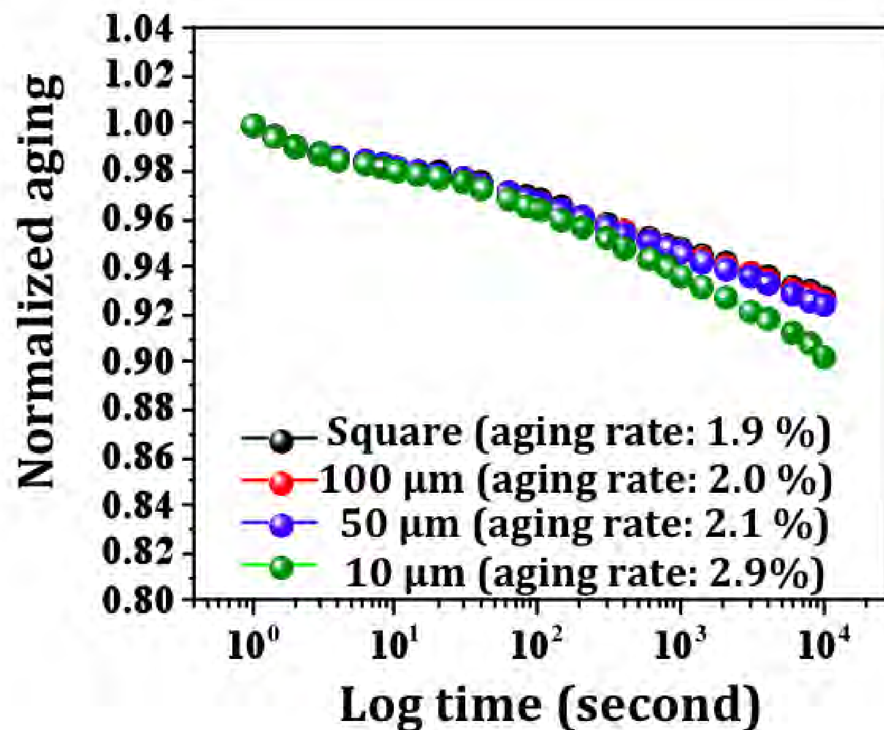

Figure 3.7. Normalized aging of the dielectric permittivity

The polarization – electric field hysteresis loops of the different patterned features are shown in Figure 3.8 (a) and (b) (measured applied voltage at 25V and frequency at 100Hz). The P-E measurements were performed at 10V, 15, 20V, 25V, 30V. It was found that the remanent polarization, P_r, of the 10 μm serpentine sample ($P_r \sim 10$ μC/cm^2) considerably exceeded that of the other patterned ($P_r \sim 5$ μC/cm^2) features as shown in Figure 8(b). Two points should be considered regarding this result; one is the smaller remanent polarization of these samples than is shown by other MPB PZT films with similar orientation and thickness. It is supposed that the PZT milling process (or some ancillary step associated with the milling) produces considerable damage. Damaged layers on either the film surface and/or sidewall then produce the lower remanent polarization. For example, Pan *et al.* reported a reduction in remanent polarization due to development of an internal field resulting from positive ion bombardment after reactive ion etching (RIE).[(10)]

The second point to notice is that the remanent polarization of the 10 μm serpentine sample is larger than that of the other patterned features at all values of the applied voltage. These results are in agreement with the work of Nagarajan *et al.*[(20)], where it was shown that when the ferroelectric is patterned into discrete islands, clamping from the substrate is significantly reduced. It is expected that the 10 μm serpentine patterns have a smaller volume of material that is mechanically clamped by the substrate than do the other parts. Therefore, their domain patterns are less controlled by residual stress and so they may have larger polarization values.

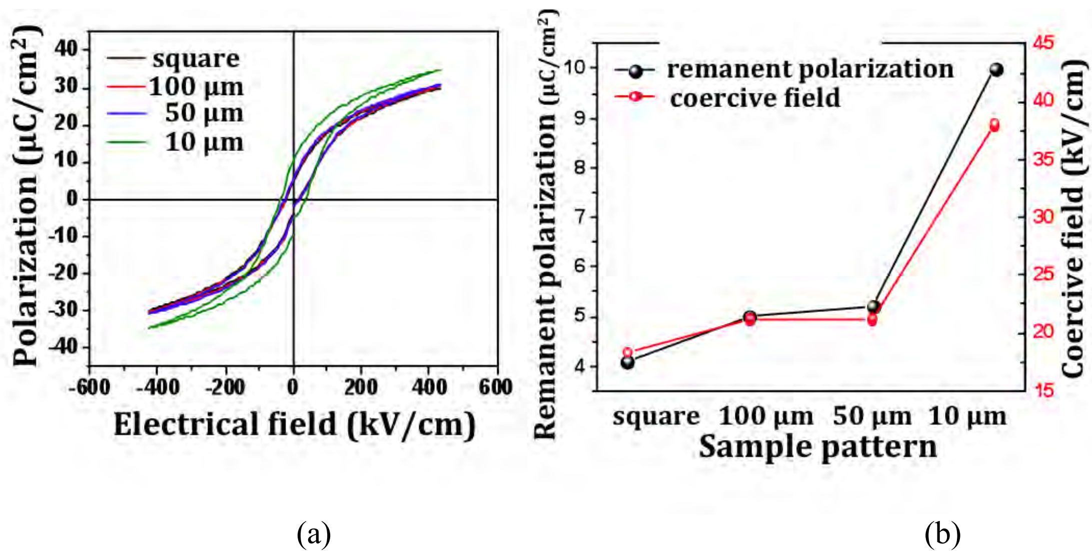

(a) (b)

Figure 3.8. (a) P-E hysteresis loop measured at 100 Hz at 25V on serpentine structures with varying degrees of substrate clamping. (b) Change in remanent polarization and coercive field of 0.5 μm patterned PZT (52/48) on a $PbTiO_3$ seed layer

The polarization switching data showed that larger switchable polarizations were achieved in the finer serpentine patterns, while the aging data show that the same patterns are more susceptible to pinning at weak fields. This suggests that the pinning sites associated with the sidewalls must be comparatively shallow in energy. As a result, while domain walls can be pinned in those wells provided the electric field excitation is small, higher fields are able to free the walls from these traps. In contrast, clamping by the substrate produces deep wells, which prevent some fraction of the spontaneous polarization to switching at high fields. A schematic, which would be consistent with this model, is shown in Figure 3.9. It can be seen that the potential energy profile is effectively smoothened with decreasing feature size by the introduction of shallow wells and the elimination of deeper wells associated with the film-substrate interface.

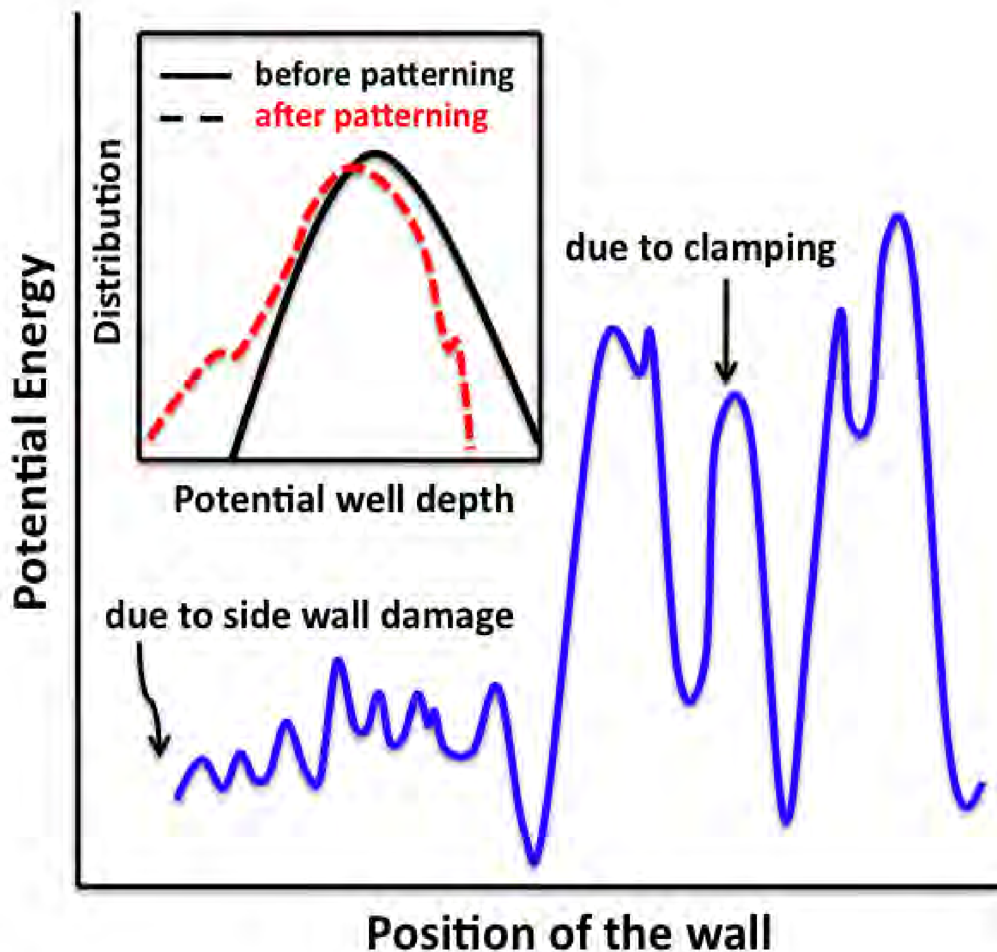

Figure 3.9. A schematic of a potential energy landscape associated with the domain wall position: energy profile of shallow well due to side wall damage and surface degradation and deep well due to clamping.

3.5. Conclusions

The dielectric and ferroelectric properties of patterned PZT (52/48) thin films patterned using Ar-ion milling were investigated. It was found that the 10 μm serpentine patterns were less clamped by the substrate than was the case for the other features; this resulted in larger

polarization values, presumably due to the reduction in clamping/residual stress. A physical model that can explain this observation is one in which clamping at the film/substrate interface produces deeper wells that prevent some fraction of the spontaneous polarization from switching at high field.

The dielectric nonlinearity in the patterned PZT thin films was described using the Rayleigh law at modest ac electric fields. After recovery annealing, it was observed that ε_{init} and α increased for smaller feature sizes. The increased Rayleigh parameters (ε_{init} and α) were attributed to reduction in the number of deep potential wells associated with substrate clamping, perhaps with commensurate changes in the length scale over which domain walls interact. However, etched patterns also aged more rapidly. It is conjectured that the sidewall damage produces shallow wells. Domains can be excited out of these shallow potential wells at the large fields used to measure the remanent polarization and the large unipolar electric fields typically used to drive thin film piezoelectric actuators. In contrast, clamping at the film/substrate interface produces deeper wells, which prevent some fraction of the spontaneous polarization to switching at high field.

3.6. References

1. J. F. Scott and C. A. Paz de Araujo, "Ferroelectric memories," Science 246, 1400 (1989)

2. C. A. Paz de Araujo, J. D. Cuchiaro, L. D. McMillan, M. C. Scott, and J.F. Scott, "Fatigue-free ferroelectric capacitors with platinum electrodes," Nature London, 374, pp. 627-629 (1995)

3. D. Dimos, S. J. Lockwood, and R. W. Schwartz, "Thin-film decoupling capacitors for multichip modules," IEEE Trans. Compon. Packag. Manuf. Technol., Part A 18, pp. 174-179 (1995)

4. T. Kawagughi, H. Adachi, K. Setsune, O. Yamazaki, and K. Wasa, "PLZT thin-film waveguides," Appl. Opt. 23, pp. 2187-2191 (1984)

5. K. Saito, J. H. Choi, T. Fukuda, and M. Ohue, "Reactive ion etching of sputtered $PbZr_{1-x}Ti_xO_3$ thin films," Jpn. J. Appl. Phys., 31,pp. L1260-L 1262, Part 2. No. 9A (1992)

6. D. P. Vijay, S. B. Desu, and W. Pan, "Reactive ion etching of lead zirconate titanate (PZT) thin film capacitors," J. Electrochem. Soc. 140, pp. 2635-2639 (1993)

7. W. Pan, S. B. Desu, I. K. Yoo, and D. P. Vijay, "Reactive ion etching of $PbZr_{1-x}$ Ti_xO_3 and RuO_2 films by environmentally safe gases," J. Mater. Res. 9, pp. 2976-2980 (1994)

8. S. Mancha, “Chemical etching of thin film PLZT,” Ferroelectrics 135, pp. 131-137 (1992)

9. J. Jung and W. Lee, “Dry etching characteristics of Pb(Zr, Ti)O_3 films in CF_4 and Cl_2/CF_4 inductively coupled plasmas,” Jpn. J. Appl. Phys., part 1, No. 3A,Vol. 40, pp. 1408-1419, (2001).

10. W. Pan, C. L. Thio, and S. B. Desu, “Reactive ion etching damage to the electrical properties of ferroelectric thin films,” J. Mater. Res., Vol.13, Issue 2, pp. 362-367 (1998)

11. D. P. Vijay, S. B. Desu, and W. Pan, “Reactive ion etching of lead zirconate titanate (PZT) thin film capacitors,” J. Electrochem. Soc., Vol.140, Issue 9, pp. 2635-2639 (1993)

12. A. Stanishevsky, B. Nagaraj, J. Melngailis, R. Ramesh and L. Khriachtchev, “Radiation damage and its recovery in focused ion beam fabricated ferroelectric capacitors,” J. Appl. Phys. 92, pp. 3275- 3278 (2002)

13. C. Soyer, E. Cattan, D. Re`miens and M. Guilloux-Viry, “Ion beam etching of lead–zirconate–titanate thin films: Correlation between etching parameters and electrical properties evolution,” J. Appl. Phys., Vol. 92, No. 2, pp. 1048-1055 (2002)

14. C. Soyer, E. Cattan, and D. Rèmiens, “Electrical damage induced by reactive ion-beam etching of lead-zirconate-titanate thin films,” J. Appl. Phys. 97, 114110-1-7 (2005)

15. J. Lee, T.Y Kim, I. Chung and S. Desu, “Characterization and elimination of dry etching damaged layer in Pt/Pb($Zr_{0.53}Ti_{0.47}$)O_3/Pt ferroelectric capacitor,” J. Appl. Phys. Lett. 75, pp. 334 – 336 (1999)

16. K. Torii, K. Shoji, H. Kawakami, T. Kumihashi, T. Itoga, N. Yokoyama, M. Moniwa, T. Kaga, and Y. Fujisaki, “Fabrication and properties of one-mask-patterned ferroelectric integrated capacitors,” Electr. Eng. Jpn. 121, pp. 43-50 (1997)

17. J. K. Lee, Y. Park, I. Chung, S. J. Oh, D. J. Jung, Y. J. Song, B. J. Koo, S. Y. Lee, K. Kim and S. B. Desu, “Improvement in the electrical properties in Pt/Pb($Zr_{0.52}Ti_{0.48}$)O_3/Pt ferroelectric capacitors using a wet cleaning method,” J. Appl. Phys., Vol. 86, No. 11, pp. 6376-6381 (1999)

18. P. Werbaneth, J. Almerico, L. Jerde and S. Marks, “PZT stack etch for MEMS devices in a capacitively coupled high-density plasma reactor,” Proc. SPIE Vol. 4592, pp. 267- 273 (2001)

19. U. Egger, K. Tomioka1, G. Stojakovic, Y. Taniguchi, R. Bruchhaus, H. Zhuang, H. Kanaya, G. Beitel and S. Sugimoto, “High temperature plasma etching of PZT capacitor stacks for high density FERAMs,” Mat. Res. Soc. Symp. Proc. Vol. 748, pp. U 1.7.1-6 (2003).

20. V. Nagarajan, A. Roytburd, A. Stanishevsky, S. Prasertchoung, T. Zhao, L. Chen, J. Melngailis, O. Auciello and R. Ramesh, "Dynamics of ferroelastic domains in ferroelectric thin films," Nature Materials, 2 pp. 43-47 (2003)

21. R. H. Liang, D. Rémiens, D. Deresmes, C. Soyer, D. Troadec, X. L. Dong, L. H. Yang, R. Desfeux, A. Da Costa, and J. F. Blach, "Enhancement in nanoscale electrical properties of lead zirconic titanate island fabricated by focused ion beam," J. Appl. Phys. 105, 044101-1-6 (2009)

22. E. G. Lee, D.J. Wouters, G. Willems, and H. E. Maes, "Voltage shift and deformation in the hysteresis loop of $Pb(Zr, Ti)O_3$ thin film by defects," Appl. Phys. Lett. 69 (9), 26, pp. 1223-1225 (1996)

23. K. Kim and M. Kang, C. Kim, "Study on the etching damage characteristics of PZT thin films after etching in Cl-based plasma," Microelectronic Engineering, 71, pp. 294-300, (2004)

24. C. W. Chung and C. J. Kim, "Etching effects on ferroelectric capacitors with multilayered electrodes," Jpn. J. Appl. Phys., Part 1 36, pp. 2747-2753 (1997)

25. L. M. Sanchez, D. M. Potrepka, G. R. Fox, I. Takeuchi, K. Wang L. A. Bendersky and R. G. Polcawich, "Optimization of $PbTiO_3$ seed layers and Pt metallization for PZT-based piezoMEMS actuators," J. Mater. Res., Vol. 28, Issue 14, pp. 1920-1931 (2013)

26. L. M. Sanchez, D. M. Potrepka, G. R. Fox, I. Takeuchi, and R. G. Polcawich, "Improving PZT thin film texture through Pt metallization and seed layers," Mater. Res. Symp. Proc. Vol. 1299, pp. 53-58 (2011)

27. S. Li, W. Cao, and L. E. Cross, "The extrinsic nature of nonlinear behavior observed in lead zirconate titanate ferroelectric ceramic," J. Appl. Phys. 69, pp. 7219-7224 (1991)

28. D. Damjanovic, "Stress and frequency dependence of the direct piezoelectric effect in ferroelectric ceramics," J. Appl. Phys. 82, pp.1788-1797 (1997)

29. N. Bassiri-Gharb, I. Fujii, E. Hong, S. Trolier-McKinstry, D. V. Taylor, and D. Damjanovic, "Domain wall contributions to the properties of piezoelectric thin films", J. Electroceram., 19[1], pp. 47-65 (2007)

30. D. V. Taylor and D. Damjanovic, "Evidence of domain wall contribution to the dielectric permittivity in PZT thin films at sub-switching fields", J. Appl. Phys., 82, pp. 1973-1975 (1997)

31. D. A. Hall, “Rayleigh behavior and the threshold field in ferroelectric ceramics”, Ferroelectrics, 223, pp. 319-328 (1999)

32. F. Griggio, S. Jesse, A. Kumar, O. Ovchinnikov, H. Kim, T. N. Jackson, D. Damjanovic, S.V. Kalinin, and S. Trolier-McKinstry, “Substrate clamping effects on irreversible domain wall dynamics in lead zirconate titanate thin films”, Phys. Rev. Lett. 108, pp. 157604-1-5 (2012)

33. P. Bintachitt, S. Jesse, D. Damjanovic, Y. Han, I. M.Reaney, S. Trolier-McKinstry, and S.V. Kalinin, “Collective dynamics underpins Rayleigh behavior in disordered polycrystalline ferroelectrics,” Proc. Natl. Acad. Sci. U.S.A. 107, pp. 7219-7224 (2010)

34. U. Robels and G. Arlt, “Domain wall clamping in ferroelectrics by orientation of defects”, J. Appl. Phys., 73, pp. 3454–3460 (1993)

35. M. Takahashi, “Space charge effect in lead zirconate titanate ceramics caused by the addition of impurities,” Jpn. J. Appl. Phys., 9, pp.1236–46 (1970).

36. H. J. Hagemann, “Loss mechanisms and domain stabilisation in doped $BaTiO_3$”, J. Phys. C: Solid State Phys., 11, pp. 3333–44 (1978).

37. Y. A. Genenko and D. C. Lupascu, “Drift of charged defects in local fields as aging mechanism in ferroelectrics,” Phys. Rev. B, 756, 149907-1-24 (2007).

38. M. Alexe, C. Harnagea, D. Hesse, and U. G sele , “Polarization imprint and size effects in mesoscopic ferroelectric structures,” Appl. Phys. Lett., Vol. 79, No. 2, pp. 242- 244 (2001)

39. W. L. Warren, D. Dimos, G. E. Pike, B. A. Tuttle, M. V. Raymond, R. Ramesh, and J. T. Evans Jr., “Voltage shifts and imprint in ferroelectric capacitors,” Appl. Phys. Lett., Vol. 67, No. 6, pp. 866- 868 (1995)

40. R. G. Polcawich, C.N. Feng, S. Kurtz, S. Perini, P. Moses and S. Trolier-McKinstry, “AC and DC electrical stress reliability of piezoelectric lead zirconate titanate (PZT) thin films,” International J. Microcircuits and Electronic Packaging, Vol. 23, pp. 85-91 (2000)

41. R. G. Polcawich and S. Trolier-McKinstry, “Piezoelectric and dielectric reliability of lead zirconate titanate thin films,” J. Mater. Res. Vol. 15, pp. 2505-2513 (2000)

Chapter 4

Fabrication and Electrical Properties of Reactive Ion Etched Antenna Patterned PZT Thin Films

This research described in this chapter is aimed at understanding how and why property stability, aging and reliability are influenced by lateral feature size in PZT thin films patterned by reactive ion etching. The previous chapter demonstrated that the electrical properties of PZT thin films patterned by argon ion milling are influenced by the lateral feature size. A physical model was established describing possible origins for the property changes on decreasing lateral feature size to 10 μm. This chapter focuses on developing antenna patterned PZT film with feature sizes down to 2 μm using a reactive ion etching process. The experimental procedures for patterning the antenna shaped features are given, along with the baseline electrical properties. The influence of this patterning on highly accelerated life tests and the property stability as a function of time are described in chapter 5 and chapter 6, respectively.

4.1. PZT Film Preparation

4.1.1. PZT Deposition

15wt% PZT (52/48) solution with 10% Pb excess made by Mitsubishi Materials was used in this research. 4 inch platinized silicon wafers (Nova Electronics, Richardson, TX) were used as substrates. The silicon substrate had 1 μm thick thermally grown silicon dioxide and Ti/Pt

with thicknesses of 200 Å and 1500 Å, respectively. The substrates were heat treated at 500°C for 60 s in O_2 in a rapid thermal annealing furnace (RTA) (Allwin21 Co. Morgan Hill, CA) prior to depositing the PZT solution to remove organic surface contaminants and moisture.

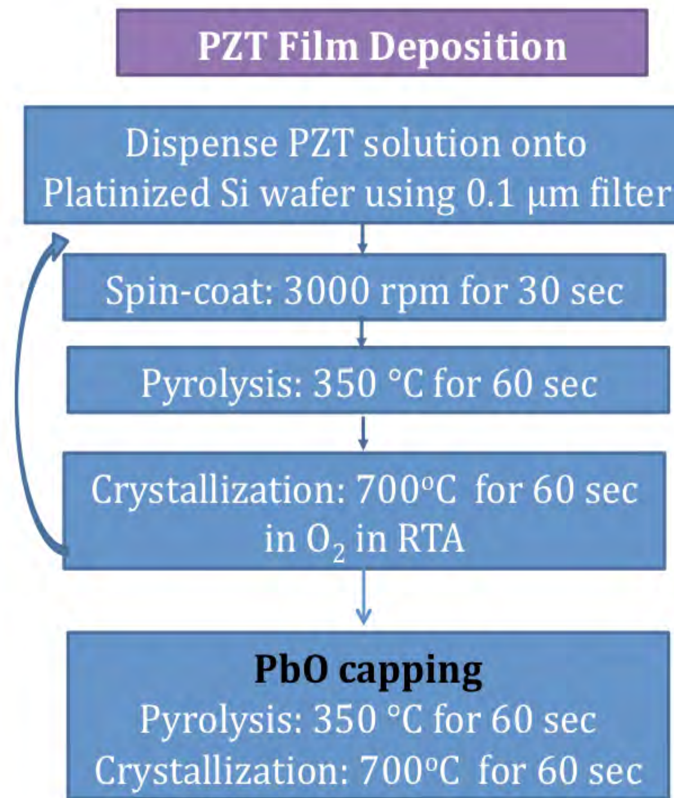

Figure 4.1. Schematic diagram of PZT film deposition

The PZT solution was spun on to the substrate at 3000 rpm for 30 s after dispensing from a 10 ml syringe with a 0.1 µm Whatman filter (GE Healthcare Life Science, Pittsburgh, PA). The first PZT layer was pyrolyzed on a hot plate in air at 350°C for 60 s and crystallized at 700°C for 60 s in 10 sccm O_2 in a rapid thermal annealing furnace, RTA (Allwin21 Co. Morgan Hill, CA). This process was repeated until the desired thickness was achieved. The final PZT film thickness is about 0.6 µm. Figure 4.1 illustrates the procedure for the film deposition.

After all of the PZT layers crystallized, the surface microstructure of the continuous PZT film was imaged on a field emission scanning electron microscope (FE-SEM, Merlin) (Carl Zeiss, Thornwood, NY).

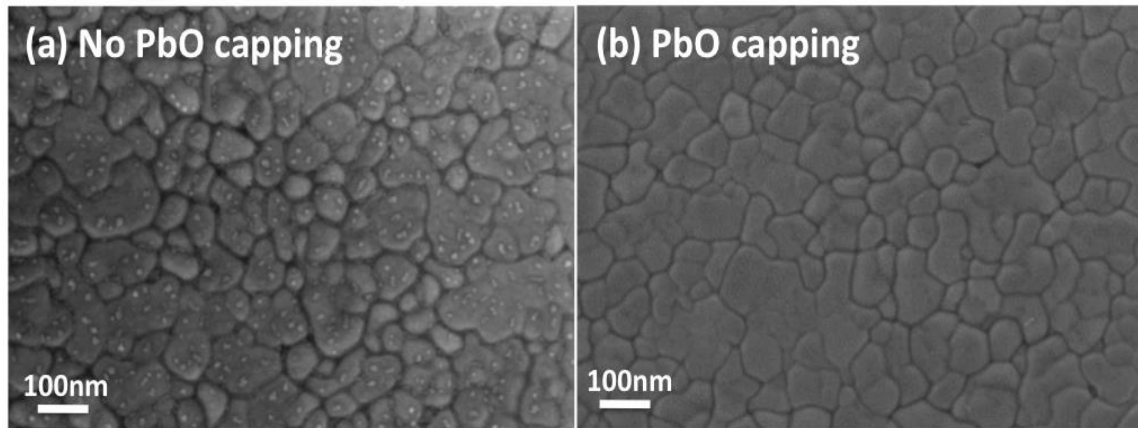

Figure 4.2. FESEM micrograph of a surface of PZT (52/48) (a) before PbO capping image, (b) after PbO capping

As shown in Figure 4.2 (a), pyrochlore phase on the surface of PZT film was observed as the presence of very fine particles due to Pb volatilization.[(1)(2)] Therefore, a PbO capping process was also performed to convert surface lead-deficient phases to the perovskite phase.[(3)] The 0.08 M solution of PbO was deposited on top of the crystallized 0.6 μm thick PZT film at 3000 rpm for 30 s using a 10 ml syringe with a 0.1 μm Whatman filter (GE Healthcare Life Science, Pittsburgh, PA). The PbO capping layer was pyrolyzed on a hot plate in air at 350°C for 60 s and crystallized at 700°C for 60 s in 10 sccm O_2 in a rapid thermal annealing furnace (Allwin21 Co. Morgan Hill, CA). This process was performed once to remove pyrochlore phases on the surface of the PZT film, as shown in Figure 4.2(b).

4.1.2. Top Electrode (Pt) and TiW Deposition

Following the PZT deposition and surface characterization, a 1000 Å thick platinum layer was deposited onto the crystallized PZT as the top electrode using RF sputtering (Kurt Lesker CMS-18 sputtering tool). The Pt target was mounted on a magnetron cathode and the Pt was deposited at 200 W RF power with a 150 mm distance from target to substrate. In order to improve adhesion between the platinum and PZT layer, the gas pressure used was 1.5 mtorr Ar. The deposition rate was 2.0nm/min. The Pt sputtering conditions are summarized in Table 4.1. After Pt deposition, a post-annealing treatment was performed at 500°C for 60 s.

After top Pt deposition, TiW was deposited on the Pt layer using RF sputtering as an adhesion layer for the Ni mask**.** In addition, TiW prevented formation of a Pt-Ni alloy, which may oxidize to produce a difficult-to-remove layer. The TiW sputtering conditions are summarized in Table 4.2.

Table 4.1. Typical sputtering parameters for the Pt film growth and post-annealing conditions

Processing Parameter	Condition
RF power (W)	200 W
Gas pressure (mTorr)	1.5 mTorr
Distance from target to substrate (mm)	150 mm
Deposition rate (nm/min.)	2.0 nm/min.
Substrate temperature (^{o}C)	Room temperature
Post annealing temperature (^{o}C)	500°C
Post annealing time (min.)	1 min.

Table 4.2. Typical sputtering parameters for the TiW layer growth

Parameters	Condition
RF power (W)	300 W
Gas pressure (mTorr)	10 mTorr
Distance from target to substrate (mm)	200 mm
Deposition rate (nm/min.)	1.0 nm/min.
Substrate temperature (^{o}C)	Room temperature

Figure 4.3 shows the fabrication flow for film deposition processes: PZT layer, top electrode Pt layer and TiW layer.

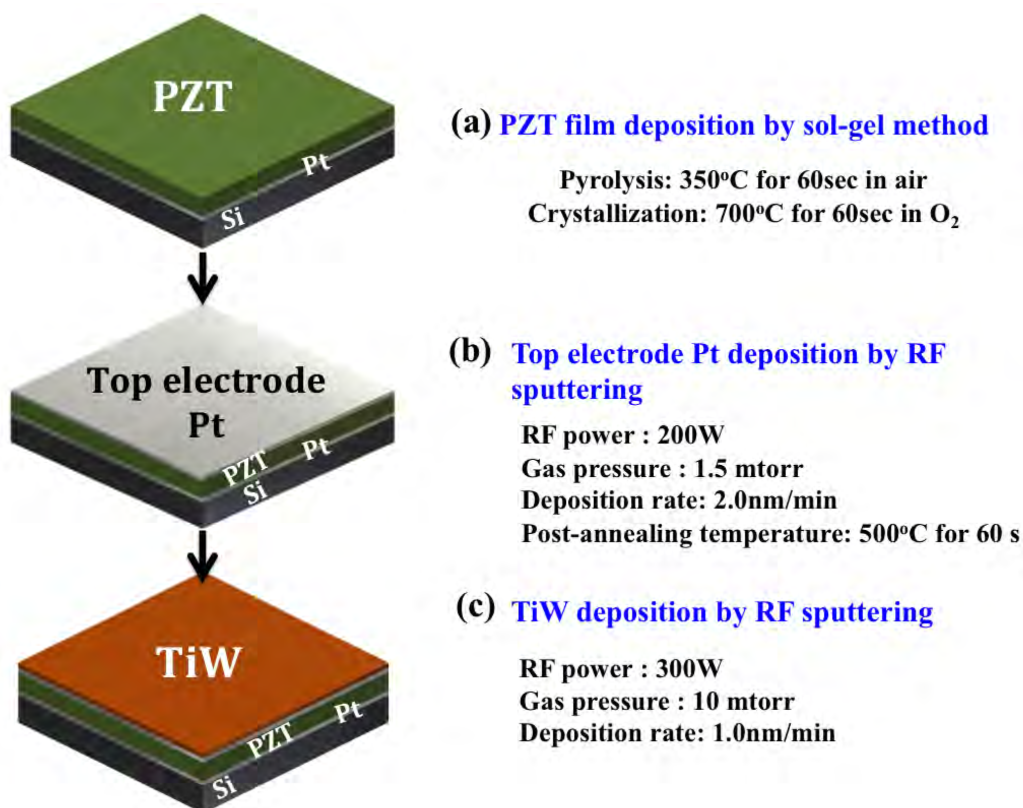

Figure 4.3. Fabrication flow for the stack growth of (a) the PZT layer on platinized Si substrate, (b) the Pt layer on the crystallized PZT film and (c) the TiW layer on Pt

4.2. Film Patterning

4.2.1. Lift – Off Lithography

After the film deposition, patterning was done by lithography, electroplating of a Ni hard mask and a reactive ion etch process with a substantial bombardment component. As shown in Figure 4.4, the lithography process started by spinning SPR 3012 photoresist at 4000 rpm for 40 seconds and baking at 95°C for 1 minute on the top Pt electrode.

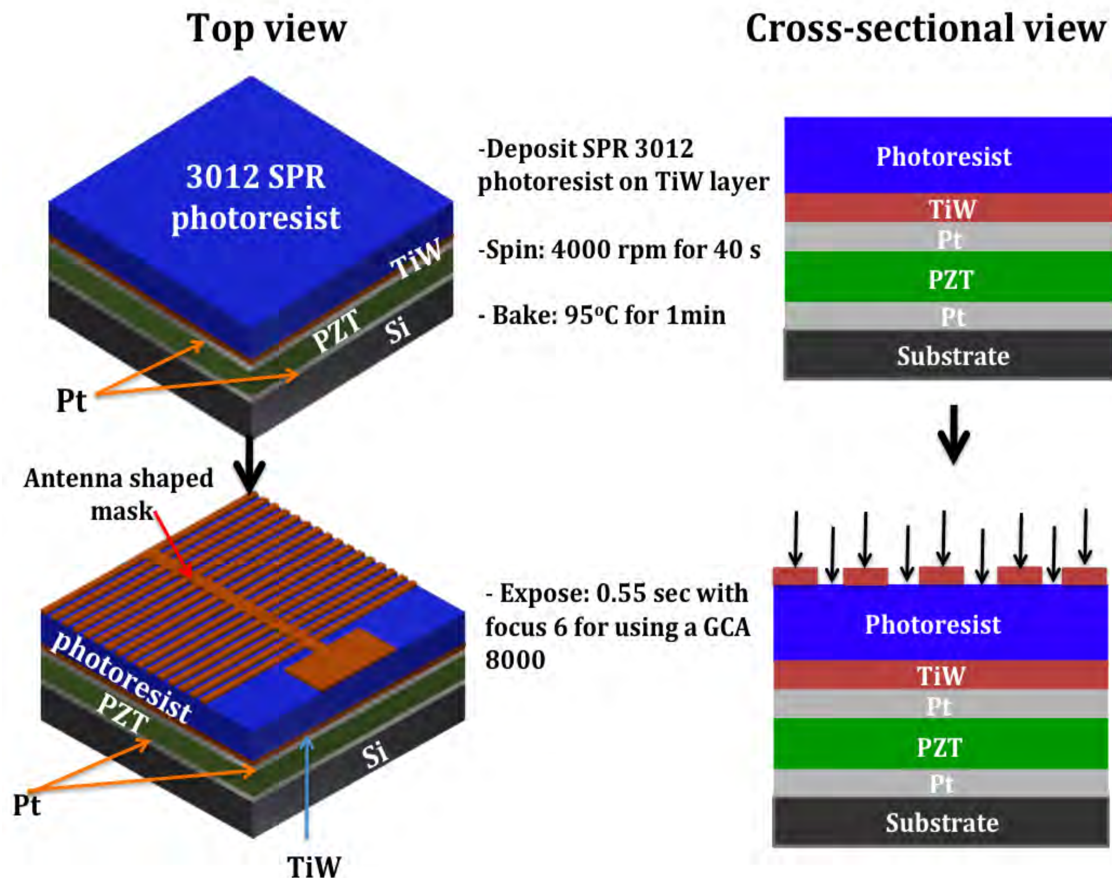

Figure 4.4. A fabrication flow- top view and cross sectional view of lithography

The 1 μm thick 3012 photoresist (Dow Electronic Materials, Malborough, MA) was patterned and exposed for 0.55 sec using a GCA 8000 i-line Stepper and was subsequently developed in MF-CD 26 developer (Rohm and Haas Electronic Materials LLC, Marlborough, MA) for 1min to expose the underlying TiW layer. Finally, it was rinsed with flowing deionized water. Figure 4.5 is a schematic of the GCA 8000 i-line Stepper and the design for a reticle.

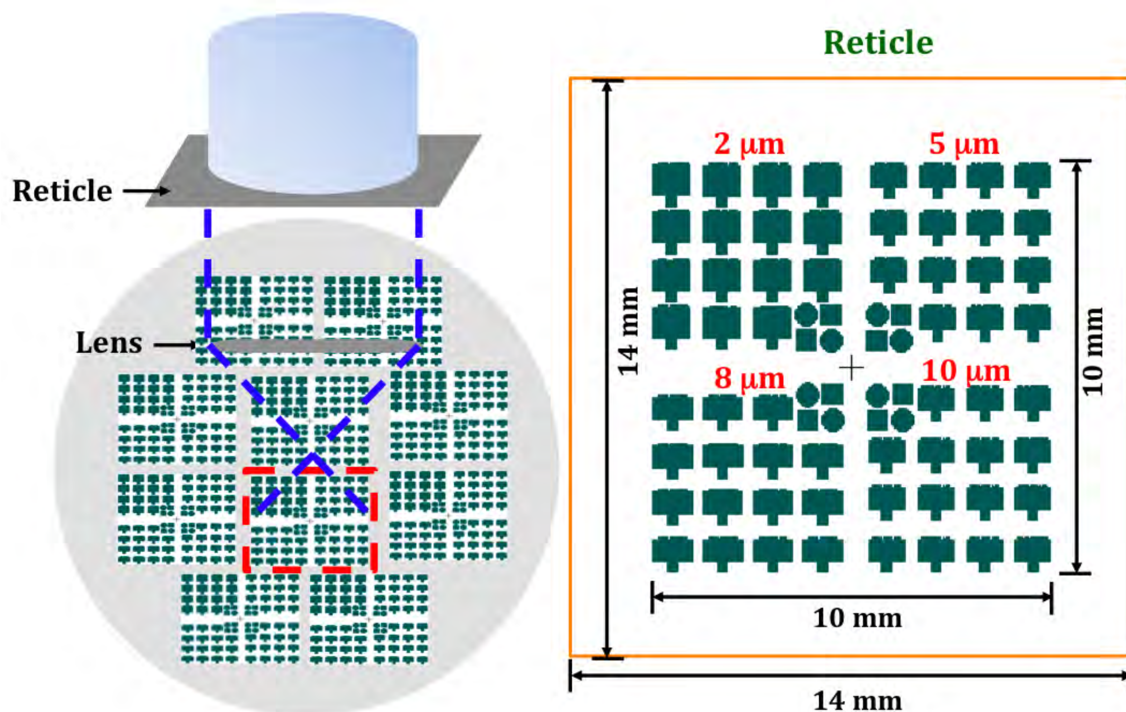

Figure 4.5. Schematic of stepper 8000 with design of reticle: antenna shaped 2 μm, 5 μm, 8 μm, 10 μm, circle and square

To remove any residual resist, the wafer underwent an oxygen plasma ashing process (M4L, MetroLine) as shown in Figure 4.6. The plasma ashing conditions are summarized in Table 4.3.

Table 4.3. Oxygen plasma ashing parameters

Processing Parameters	Condition
O_2 (sccm)	150
He (sccm)	50
Pressure (mTorr)	500
Power (W)	150
Times (min)	2

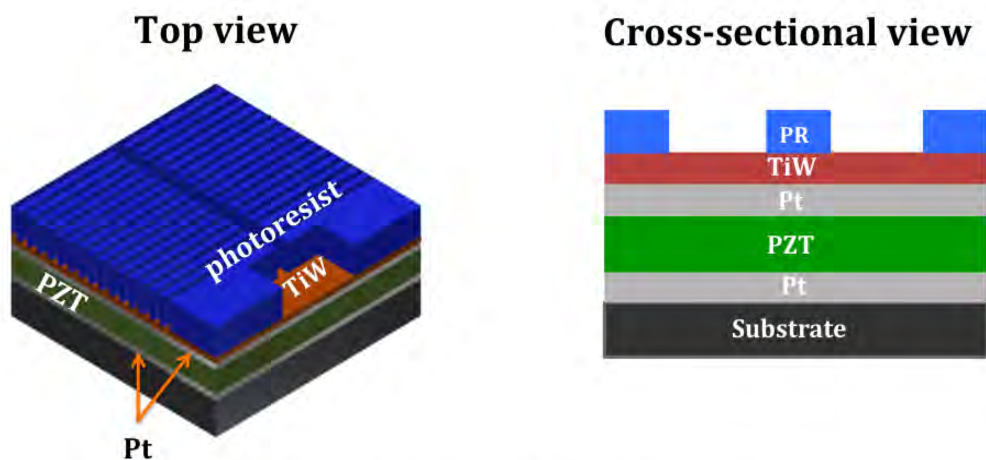

Figure 4.6. A fabrication flow- top view and cross sectional view of developing and oxygen plasma ashing after exposure

4.2.2. Nickel Electroplating

Ni is known to be chemically inert and very resistant to physical sputtering. Thus, a Ni hard mask was chosen in order to etch the PZT and Pt with good anisotropy, selectivity and a reasonably vertical sidewall angle. To fabricate the Ni hard mask, dc electroplating was carried out using a Dynatronix MicroStart Pulse Precise programmable power supply (Dynatronix, Amery, WI) and a Ni sulfamate plating solution (Transene CO Inc. Danvers, MA) into a photoresist mold as shown in Figure 4.7.

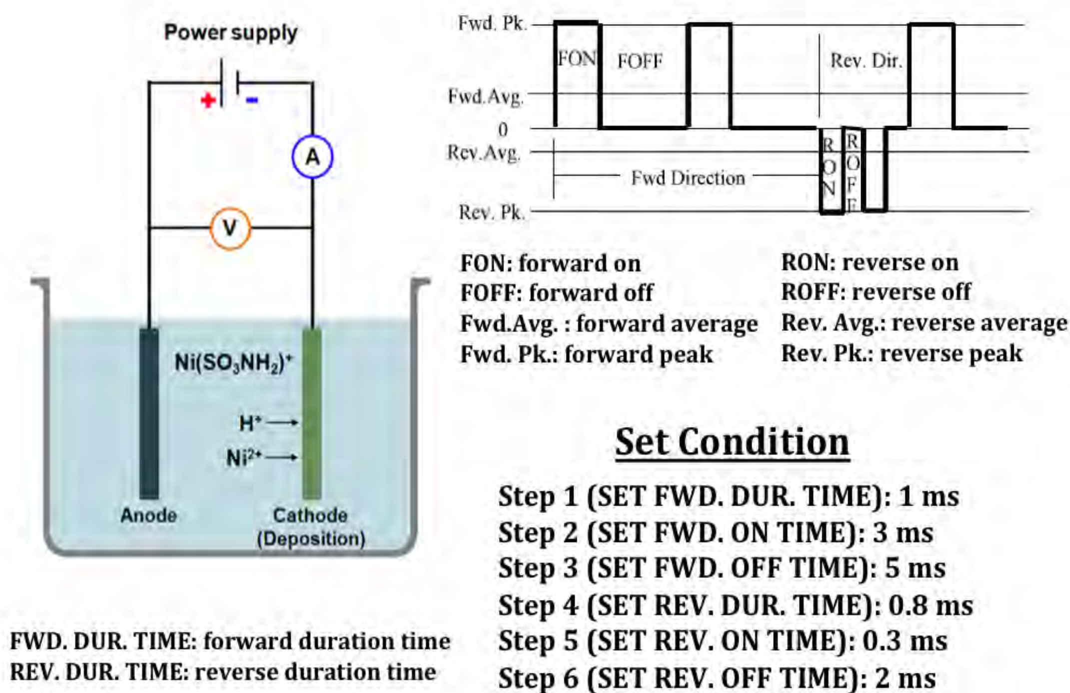

Figure 4.7. Illustration of Ni electroplating process and process parameters

A 350 ~ 450 nm thick Ni hard mask was deposited at 0.9-1.05 volts for 5-10 minutes. The plating conditions were: forward bias 0.25-0.3 V, reverse bias 0.025-0.03 V. Following this

step, the photoresist was removed using a combination of acetone and O_2 plasma ashing (Metroline M4L Plasma Etcher) as shown in Figure 4.8.

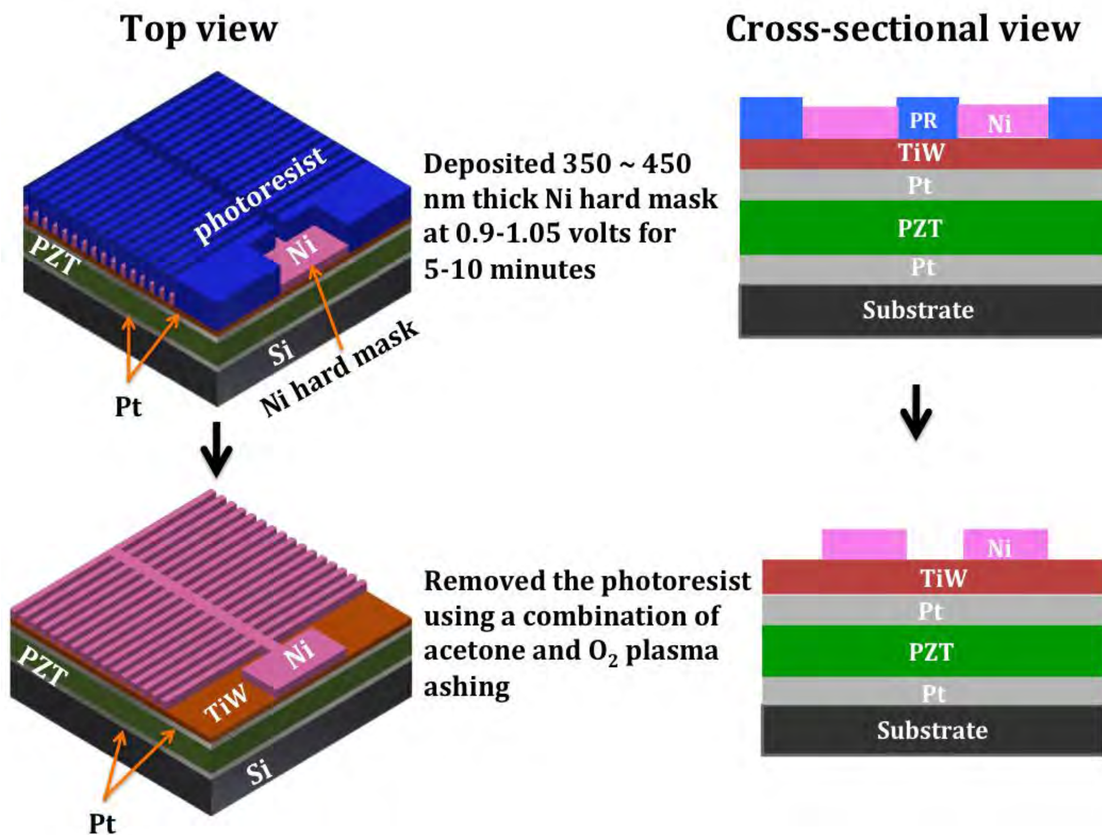

Figure 4.8. Fabrication flow used for Ni electroplating to form the Ni hard mask and remove the photoresist.

Optimization of the conditions for preparation of the Ni hard mask was critical. It was found that the applied voltage should be maintained in the range of 0.9-1.5V, so that the deposition rate was around 55-60 nm/min. When higher voltages were applied (above 1.5V), the Pt top electrode started to flake off from the edge. This resulted in non-uniformity of the Ni layer

as shown in Figure 4.9 (a). When the applied field was below 0.9 V, the deposition rate was too low (30-25 nm/min) so that the films were exposed to the Ni sulfamate plating solution for a long time (Transene CO Inc. Danvers, MA). This resulted in damage to the films and delamination of the top Pt. Figure 4.9 shows good and bad examples of optical images after Ni electroplating depending on the applied voltage.

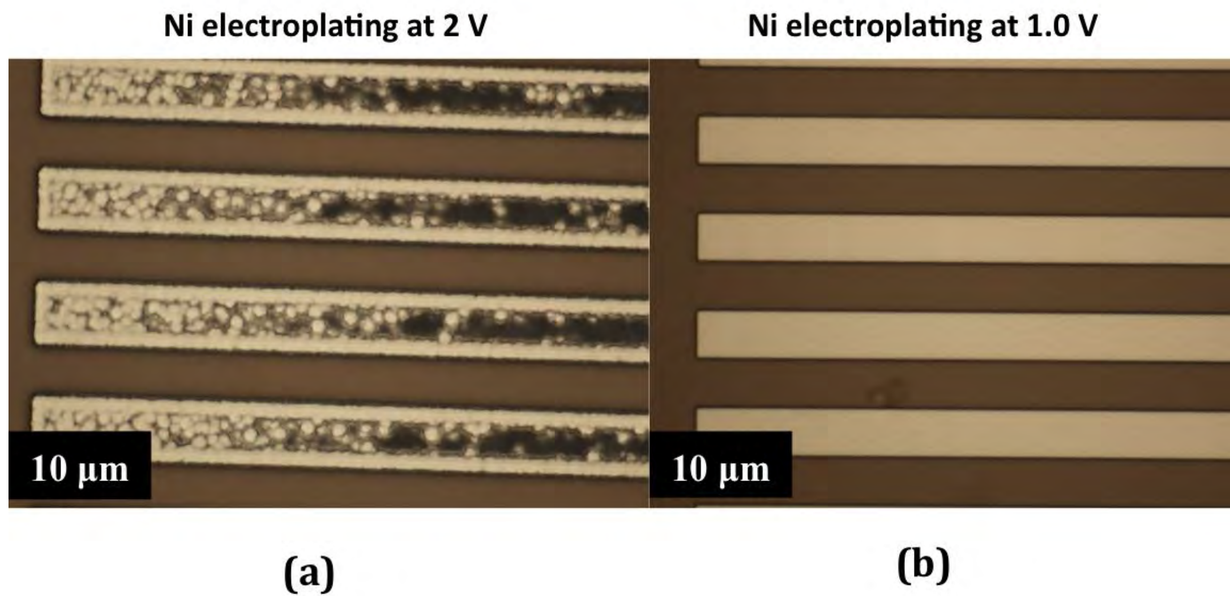

Figure 4.9. Optical images of surface of 10 μm arm size of PZT film after Ni electroplating (a) at 2V and (b) at 1V.

4.2.3. Top Pt and PZT Etching

In the next step, the PZT layer and top Pt layer were removed using an ULVAC NE-550 ICP-RIE tool. The reactive ion etching of Pt and PZT was performed with a Ni hard mask, as shown in Figure 4.10. First, the top electrode Pt was etched in a mixed etch gas (40 sccm Ar and 30 sccm Cl_2) at an inductively coupled plasma (ICP) power of 700 W and an reactive ion etching

(RIE) power of 100 W. The chamber pressure was maintained at 3.5 mTorr. The resultant etch rate was about 50 nm/min. Pt etching steps of 60 s in duration were repeated twice until the surface of PZT layer was exposed. After the top Pt etch step, PZT was etched using three different etch gases: 10 Ar and a 3.5/7 mixture of Cl_2 and CF_4. The chamber pressure was operated at 3.8 mTorr and at ICP power of 600 W and RIE power of 150 W. PZT etching steps of 60 s in duration were repeated four times to reach the bottom electrode Pt. The top Pt and PZT etch conditions are summarized in Table 4.4.

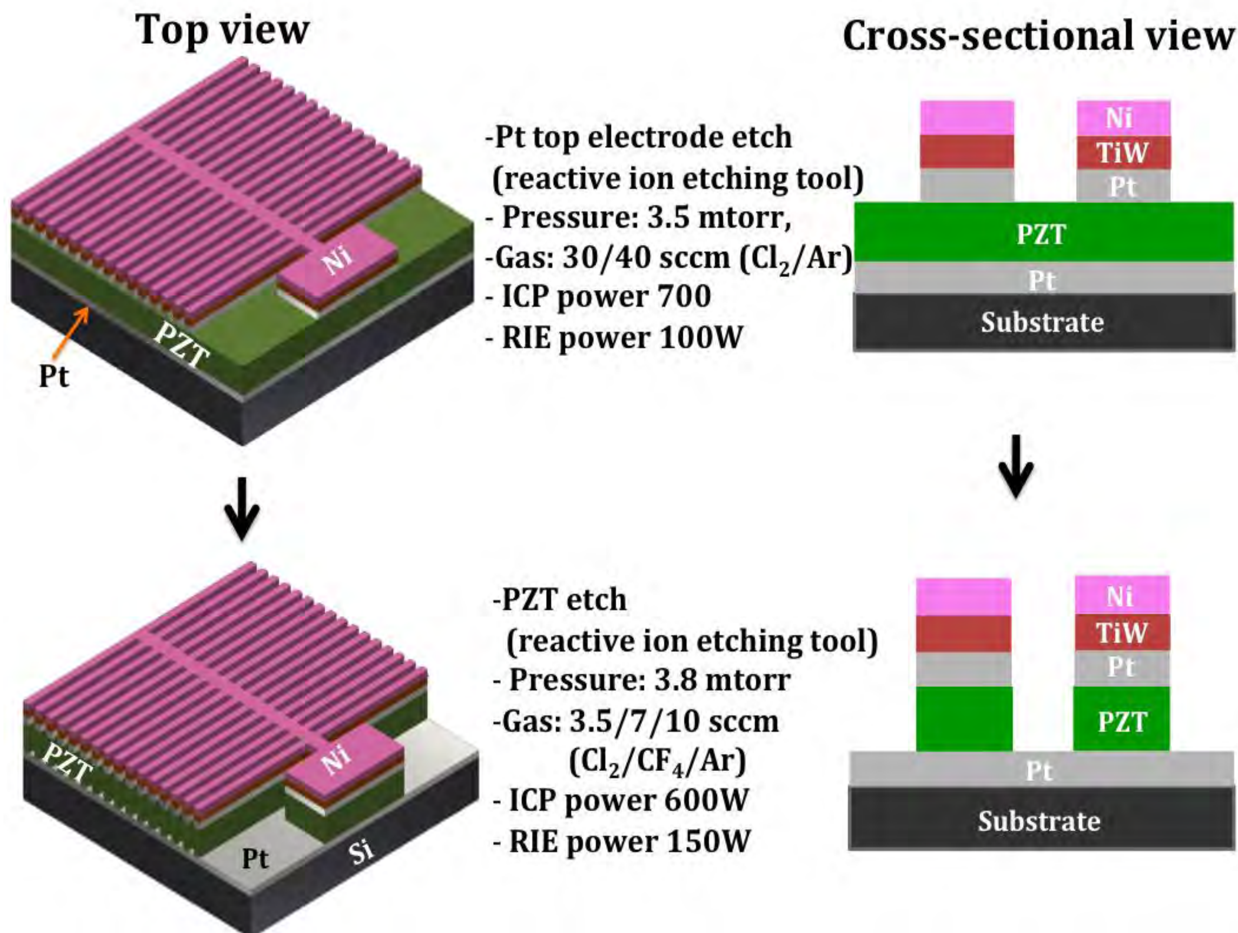

Figure 4.10. Fabrication flow: etching of top Pt electrode and the PZT film

Table 4.4. Reactive ion etch parameters for top Pt and PZT layers. (ICP = inductively coupled plasma)

	Pt	PZT
Pressure (mTorr)	3.5	3.8
Gas (sccm)	30 (Cl_2)	3.5 (Cl_2)
	0	7 (CF_4)
	40 (Ar)	10 (Ar)
ICP (W)	700	600
RIE (W)	100	150
Etch rate (nm/min)	50	120

4.2.4. Stripping of Ni and TiW Layers

To access the top electrode, first, the Ni layer was removed by immersion in Transene Ni etchant Type I for 20 sec at room temperature. Then, the sample was bathed in hydrogen peroxide for 5 min at room temperature to remove the TiW layer, as shown in Figure 4.11. The film was annealed at 500°C for 1 min in RTA to recover any decrease in properties associated with fabrication.

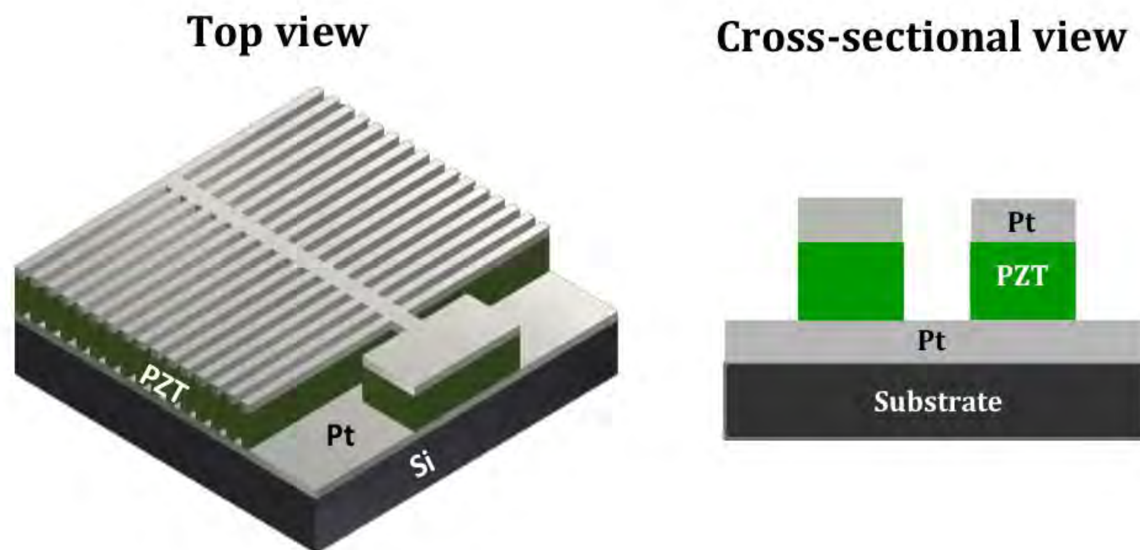

- Etch Ni (300nm) using Transene Type I for 20 sec at room temperature
- Etch TiW (30nm) using hydrogen peroxide for 5min at room temperature
- Recovery annealed at 500°C for 1min in RTA

Figure 4.11. Fabrication flow: stripping of Ni and TiW

Each feature size for the antennae shaped structure and the final sample structure are shown in Figure 4.12. The PZT thin film was patterned into antenna shapes with line widths of 10 μm, 8 μm, 5 μm, or 2 μm. In the same run, square and circle designs were also fabricated to mimic a fully clamped film; all patterns have the same surface area of 309,000 μm^2 but the perimeter increases as the feature size decreases. This allows the effect of the etch perimeter to be evaluated.

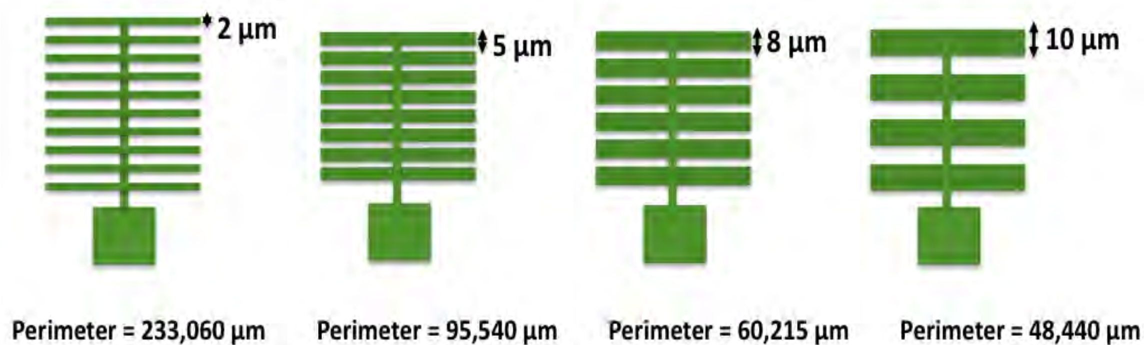

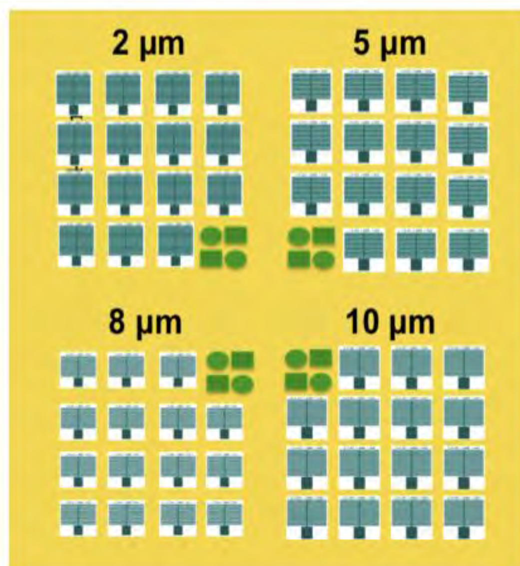

Figure 4.12. Schematic diagram of (a) each feature size antennae structure and (b) final sample structure with typical line widths of the antenna shaped including 10 µm, 8 µm, 5 µm, 2 µm, and square and circle designs

4.3. Structure and Electrical Characterization

The baseline structural and electrical properties of the continuous PZT films were examined. X-ray diffraction (XRD) data were collected for both the 0.6 μm thick continuous and patterned PZT film using a Panalytical X'pert Pro MPD. Scan ranges were from 20 to 60 degrees using a step size is 0.02 degrees with a count time of 1.5 seconds and scan rates of 1.00 ^{o}/minute. An RT-66A multiferroic Test System (Radiant Technology, Inc. Albuquerque, NM) was used to measure the polarization – electric field hysteresis loops at 100 Hz. Measurements of the dielectric constant, loss tangents, Rayleigh parameter, and aging were performed using a Hewlett-Packard 4284A LCR meter (Agilent Technology, Palo Alto, CA).

4.3.1. Continuous PZT (52/48) Thin Films

A. Crystal Structure and Microstructure of Continuous PZT Films

As shown in Figure 4.13 (a), the x-ray diffraction patterns of the 0.6 μm thick continuous PZT (52/48) film showed a phase-pure perovskite structure with predominantly {111} orientation (within X-ray diffraction detection limits). The film microstructure was investigated using a Merlin field emission scanning electron microscope (Merlin FE-SEM) (Carl Zeiss). As shown in Figure 4.13 (b), there is no evidence for pyrochlore phase on the surface of PZT film or for PbO platelets. The average surface grain size was between ~ 115 nm as determined using Image J software.

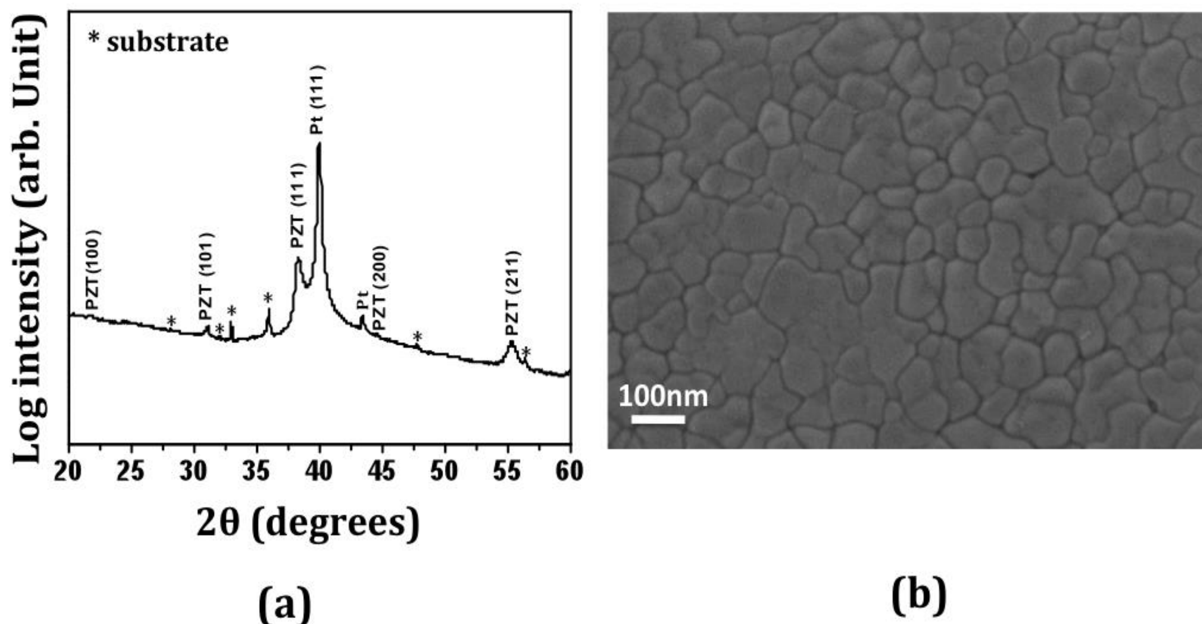

Figure 4.13. (a) X-ray diffraction patterns (asterisks indicate peaks from the silicon or the Pt from radiation wavelengths other than Cu Kα) and (b) surface microstructure of the continuous PZT (52/48) film

B. Electrical Properties of Continuous PZT Film

Figure 4.14 shows the frequency dependence of the dielectric constants and dielectric loss for the continuous PZT film. All measurements were performed after annealing the samples at 500 ^{o}C for 1 minute in O_2. The dielectric constant of the 600 nm thick PZT (52/48) continuous thin films was 920 and the dielectric loss was 0.015~ 0.025, as measured at 10 kHz with 0.03 V_{ac}. The P-E hysteresis loops were well saturated, measured at 400 kV/cm – 500 kV/cm at 100 Hz. The remanent polarization (P_r) was 20 μC/cm^2 and coercive field (E_c) was 50 kV/cm as shown in Figure 4.12.

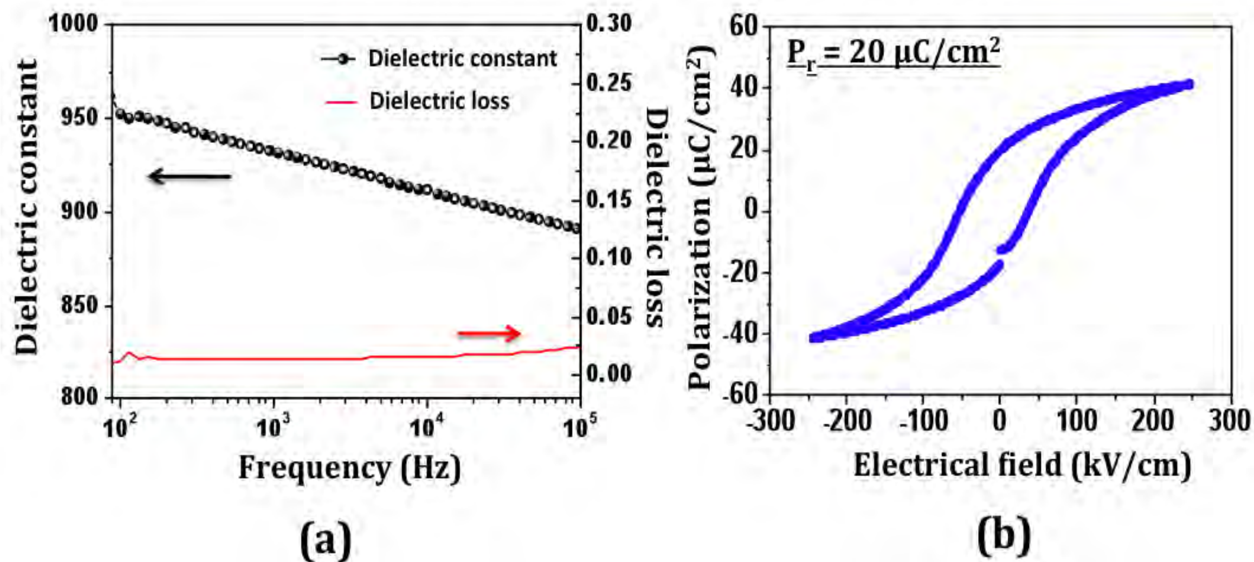

Figure 4.14. (a) Frequency dependence of the dielectric constants and tangent loss and (b) the polarization-electric field hysteresis loop of a 0.6 μm thick continuous PZT (52/48) film

4.3.2. Patterned PZT (52/48) Thin Films

A. Microstructure

Good patterning and relatively steep sidewall angles are shown in Figure 4.15. The etch rate for the PZT film was 120 nm/min and the sidewall angle of all features was ~75°.

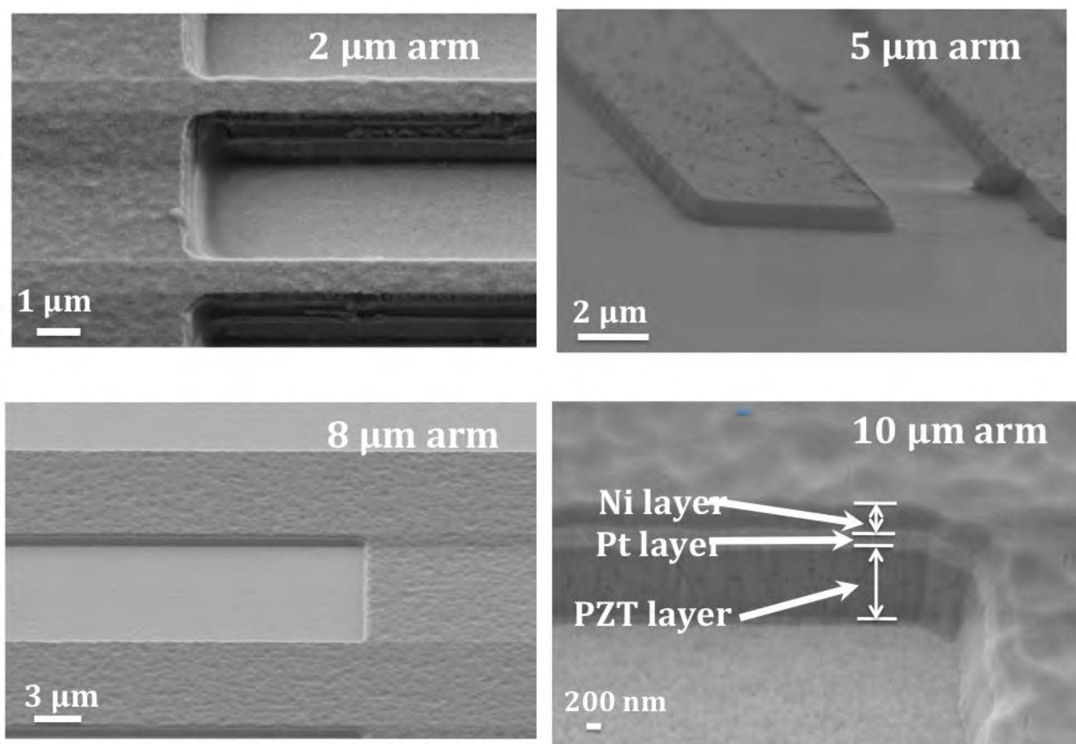

Figure 4.15. FESEM micrograph of a 2 μm, 5 μm, 8 μm, or 10 μm wide arms of the antenna patterned 0.6 μm PZT (52/48) film. Dry etching was completed using a Ni hard mask

B. Dielectric and Ferroelectric Properties

After patterning, the antenna patterned PZT thin films were measured to assess the effect of induced damage and changes in the mechanical clamping. The patterned PZT dielectric properties were recorded for varying arm feature sizes. The dielectric constant ranged between 900 and 1200 and the dielectric loss was 0.015 - 0.05 as a function of frequency, as shown in Figure 4.16 (a) and (b) respectively (note that the apparent increase in loss at high frequencies is

an artifact). An enhancement of the dielectric constant with reduction of lateral feature size was observed due to partial declamping from the substrate.

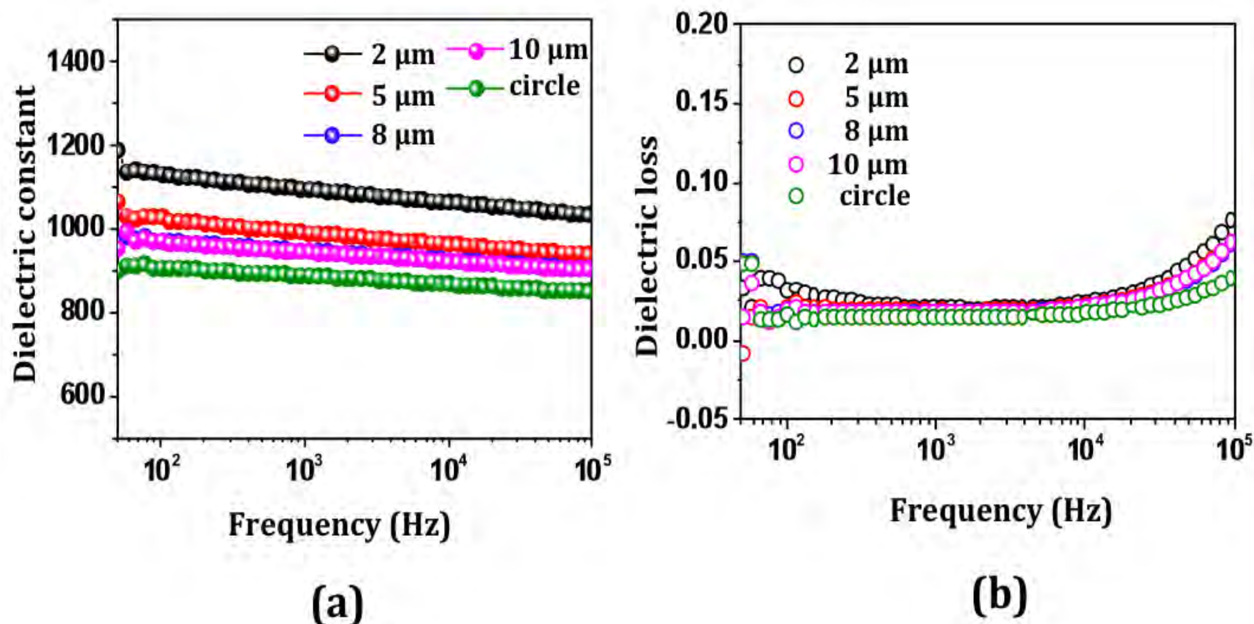

Figure 4.16. (a) Frequency dependence of the dielectric constants and (b) tangent loss of a 0.6 µm thick antenna shaped PZT (52/48) film

As mentioned in Chapter 2, the Rayleigh law was used to investigate the dielectric nonlinearity in the antennae shaped patterned PZT thin films at modest ac electric fields. The dielectric constant is plotted as a function of AC electric field for different lateral feature sizes of PZT (52/48) film in Figure 4.17 (a). To obtain the reversible (ε_{init}) and irreversible Rayleigh (α) parameters, the linear region was fitted for each lateral feature size. The result shows that both reversible (ε_{init}) and irreversible Rayleigh (α) parameters decreased with increasing lateral feature size. The 1:0.25 aspect ratio (2 µm antenna feature size) shows a 10% increase of

reversible coefficient compared with the clamped state (circle or square shape) as shown in Figure 4.17 (b). It is expected that the domain wall movement may increase when a PZT film was declamped from the substrate by patterning. This suggests that the film-substrate interface provides a significant source of pinning for domain wall motion. As the film is patterned to smaller feature sizes, less of the film is clamped by the interface, and so the domain walls are freer to respond to the applied electric field.

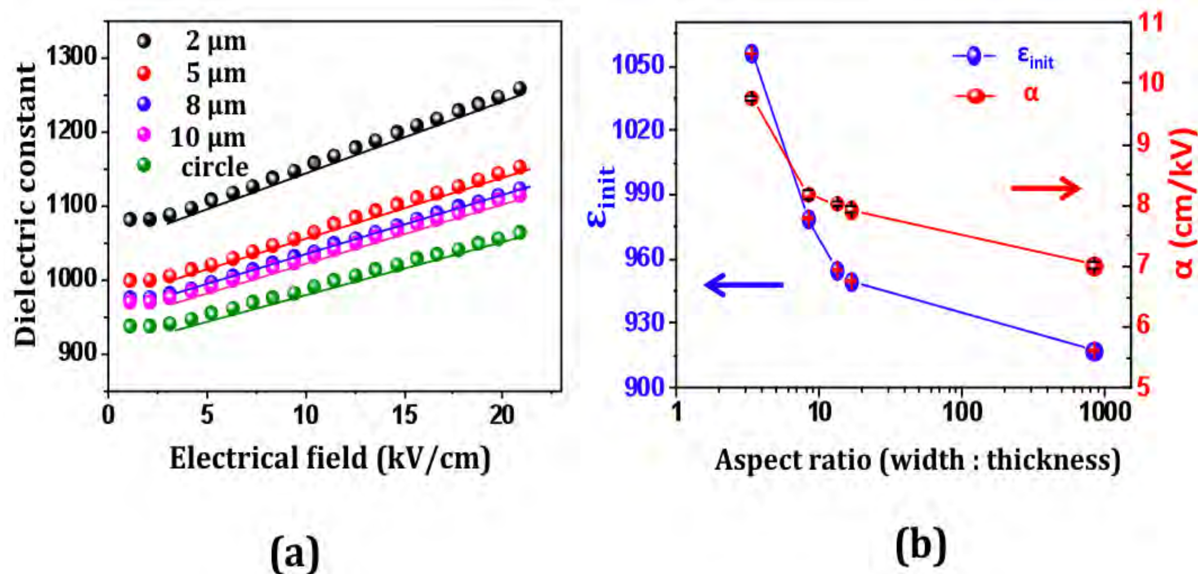

Figure 4.17. (a) The field dependence of dielectric constant and (b) reversible (ε_{init}) and irreversible Rayleigh (α) coefficient as a function of aspect ratio

Figure 4.18 (a) shows the polarization – electric field hysteresis loops of the different patterned features to examine various degrees of declamping from the substrate.

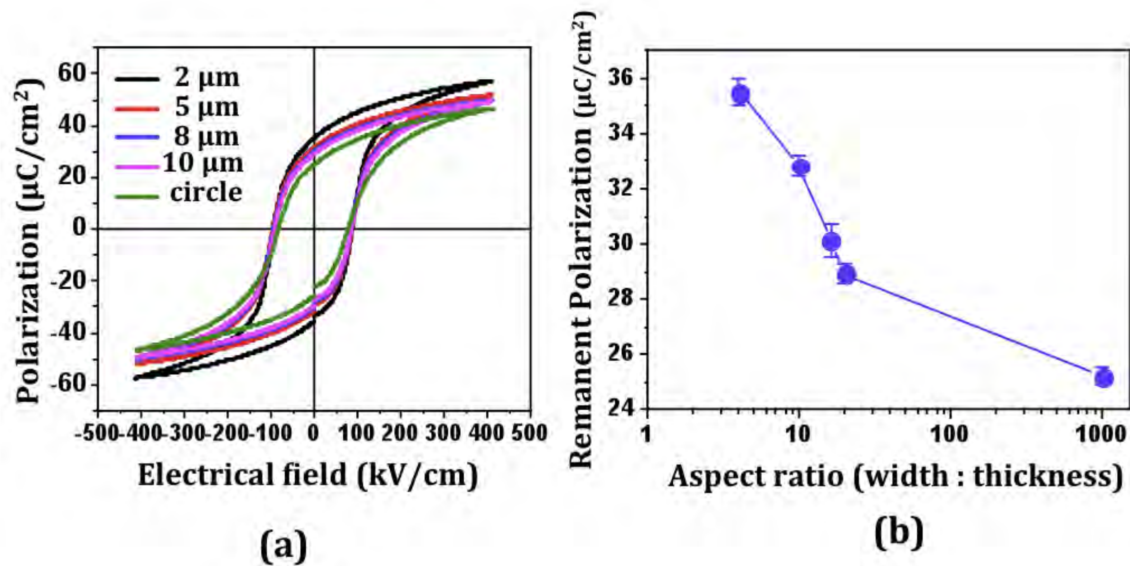

Figure 4.18 (a) P-E hysteresis loop and (b) remanent polarization film for a 0.6 μm thick antenna shaped PZT (52/48) film as function of lateral feature size

It was observed that the remanent polarization increased to 35.7 ± 0.5 μC/cm^2 for the 2 μm arm size, compared to 25 ± 0.3 μC/cm^2 for the clamped circular and square features. As the aspect ratio increased, the remanent polarization decreased as seen in Figure 4.18 (b). The result shows comparable behavior with the data in chapter 3 as well as the results of Nagarajan et al., where it was reported that when the ferroelectric is patterned laterally or into discrete islands, the film is less clamped by the substrate.(4) It is believed that the domain reorientation increases when the substrate-imposed clamping is reduced. As a result of this, the smallest arm size, 2 μm, has larger polarization values, given that the domain state is less controlled by residual stress.

4.4. References

1. Vladimír Koval, "High aspect ratio lead zirconate titanate tube structures: I. Template assisted fabrication - vacuum infiltration method", Processing and Application of Ceramics 6 [1], pp. 37–42 (2012)

2. Takeshi Yoshimura and Susan Trolier-McKinstry, "Growth and piezoelectric properties of $Pb(Yb_{1/2}Nb_{1/2})O_3$-$PbTiO_3$ epitaxial films", J. Appl. Phys., Vol. 92, No. 7, pp. 3979-3984 (2002).

3. T. Tani and D. A. Payne, "Lead oxide coatings on sol–gel-derived lead lanthanum zirconium titanate thin layers for enhanced crystallization into the perovskite structure," J. Am. Ceram. Soc. 77, 1pp. 242-1248 (1994)

4. J. I. Yang, R. G. Polcawich, L. M. Sanchez,and S. Trolier-McKinstry, "Effect of feature size on dielectric nonlinearity of patterned $PbZr_{0.52}Ti_{0.48}O_3$ films," J. Appl. Phys., 117, pp. 014103-1-7 (2015)

Chapter 5

DC Electrical Field Reliability and Conduction Mechanisms of Patterned PZT Films

5.1. Introduction

PZT-based materials have been developed for a wide range of applications such as capacitors, sensors, actuators, non-volatile memories and micro-electromechanical system (MEMS) because of their large dielectric and piezoelectric response.[1][2][3] While initial results of piezoMEMS are promising, there is no available database on the reliability of films under high driving fields, particularly in patterned devices as compared to the original blanket films. The lifetime limiting factors for this application are not expected to be identical to those of ferroelectric memories (e.g. fatigue and data retention).[3][4] Thus, the goal of this chapter is to examine the time dependence of the behavior of patterned PZT films, with an emphasis on the time-dependent dielectric breakdown and leakage current.

Time-dependent dielectric breakdown is a loss of the insulating properties after long exposure to applied electrical fields that the material could originally withstand. Often, to accelerate the process, lifetime experiments are conducted at elevated temperatures. It is likely that the factors that influence the lifetime will also affect the property stability over time. Therefore, an understanding of the factors that control the failure mechanism has become a key to the establishment of piezoMEMS with high reliability.

A number of processes associated with conduction and time dependent breakdown in the alkaline earth titanate perovskites such as $BaTiO_3$ and $SrTiO_3$ have been studied and possible failure mechanisms suggested.[5][10] Waser *et al.* investigated the dc resistance degradation

mechanism in acceptor - doped $SrTiO_3$ ceramics and single crystals. They found migration of oxygen vacancies ($V_o^{\bullet\bullet}$) with subsequent accumulation at the cathode in conjunction with depletion region of oxygen vacancies at the anode. It was proposed that this process was the main dc degradation mechanism. They reported a range of activation energies (from 0.8 to 1.2 eV) for oxygen vacancy diffusion.(6)(7)(8)(9)(10)

However, the breakdown mechanism of lead based perovskites may be affected by PbO volatilization during high temperature processing, or by the presence of unintentional dopants that favor development of oxygen vacancies.(11)(12) For PZT films, Dimos *et al.* showed that the mean time to failure, t_f of donor-doped $Pb_xNb_{0.03}(Zr_{0.40}Ti_{0.60})_{0.97}O_3$ (3/40/60) thin film capacitors is remarkably improved compared with that of undoped PZT (40/60) film. This was attributed to reduction of the oxygen vacancy and hole concentrations ([$V_o^{\bullet\bullet}$] and [$h^{\bullet}$], respectively) that develop in the undoped films due to lead loss.(13) Bouyssou *et al.* studied the low voltage (5V dc field) failure mechanism for decoupling capacitors.(14) They reported that the low voltage (dc stressing of 5V) failure in IrO_2/PZT (52/48) films on platinized Si is related to the trapping-induced formation of defects in the film. Reported possible trapping centers for holes in PZT material were ionized Pb vacancies and transition metal impurities.(11)(13) Other publications state that the degradation rate can be influenced by the grain size, stoichiometry, film thickness and electrode-type as well as the electric field, temperature, composition, and doping.(9)(10)(11)(13) These previous reports are summarized in Table 5.1.

Table 5.1. Reported resistance degradation mechanisms of bulk and thin film of lead based perovskite materials (modified from reference [12])

Reference	Material	Film deposition	Method	Activation energy	Mechanism	Comments
Al-Shareef and Dimos [13]	Donor doped PZT (PNZT (4/50/50), and PLZT (4/50/50) thin film)	Chemical solution deposition (sol-gel)	I-V-T	1.3 eV	Thermally activated field-dependent emission of trapped holes (*h*)in the bulk.	Proposed Frenkel-Poole emission model for conduction mechanism
Bouyssou et al. [14]	IrO_2/PZT (52/48)/Pt thin film	Chemical solution deposition (sol-gel)	I-V	0.9 eV at applied voltage of 5V	Trapping-induced creation of defects in the film. Pb vacancies and transition metal impurities act as trapping centers for holes	Reported low voltage breakdown for decoupling capacitor
Dih and Fulrath [15]	Undoped PZT and Nb-doped PZT bulk		I-V-T	1.4 eV < 650°C	Hole migration associated with Pb vacancies	
Raymond and Smyth [16]	PZT (50/50) bulk		I-V-T	0.3 eV	Hole hopping between Pb^{3+} and Pb^{2+}	

Reference	Material	Film deposition	Method	Activation energy	Mechanism	Comments
Chen et al. [17]	PZT (52/48) thick film	Sol-gel spin coating	I-V-T			8 μm thick film
Robertson et al. [18]	PZT (52/48) bulk		*EPR and band structure calculations	0.26 eV	Hole hopping between Pb^{3+} and Pb^{2+}	*EPR: electron paramagnetic resonance
Kang et al. [19]	(Pb, La)(Zr,Ti)O_3 bulk	Solid state sintering	IS	0.36 - 0.67 eV	Thermal motion of oxygen vacancies	

However, it is anticipated that some of these processes may change as films are patterned into devices laterally, inducing exposed sidewalls, sidewall damage, and simultaneously changing the state of mechanical clamping. Thus the purpose of this study is to understand the breakdown mechanism and lifetime characteristics as a function of feature size by employing highly accelerated lifetime tests (HALT) and by evaluation of the current-voltage (I-V) characteristics.[20][21][22][23][24][25]

5.2. Experimental Procedure

5.2.1. HALT Analysis

0.6 μm thick patterned PZT (52/48) films with different feature sizes were investigated to examine time dependent dielectric breakdown under highly accelerated lifetime test (HALT) conditions. A 15wt% PZT (52/48) solution with 10% Pb excess made by Mitsubishi Materials was used to grow the films on platinized silicon wafers (Nova Electronics, Richardson, TX) by using chemical solution deposition. After film deposition, patterning was done by lithography, electroplating of a Ni hard mask and a reactive ion etch process to obtain lateral feature sizes of 2 μm, 5 μm, 8 μm, 10 μm. The sample fabrication procedures are described in detail in chapter 4.

In brief, the patterned PZT on 4-inch platinized silicon wafers was diced into ~ 1cm by 1cm squares using a 7100 ProVectus-TS Precision Dicing System (Advanced Dicing Technologies, Ltd.) to mount in 24-pin DIP packages (Spectrum Semiconductor Materials, Inc.) with silver paste. After the silver paste dried, the samples were wire bonded to make contact between each top electrode and the gold contact pad of the DIP package with gold wire (Kulicke and Soffa).

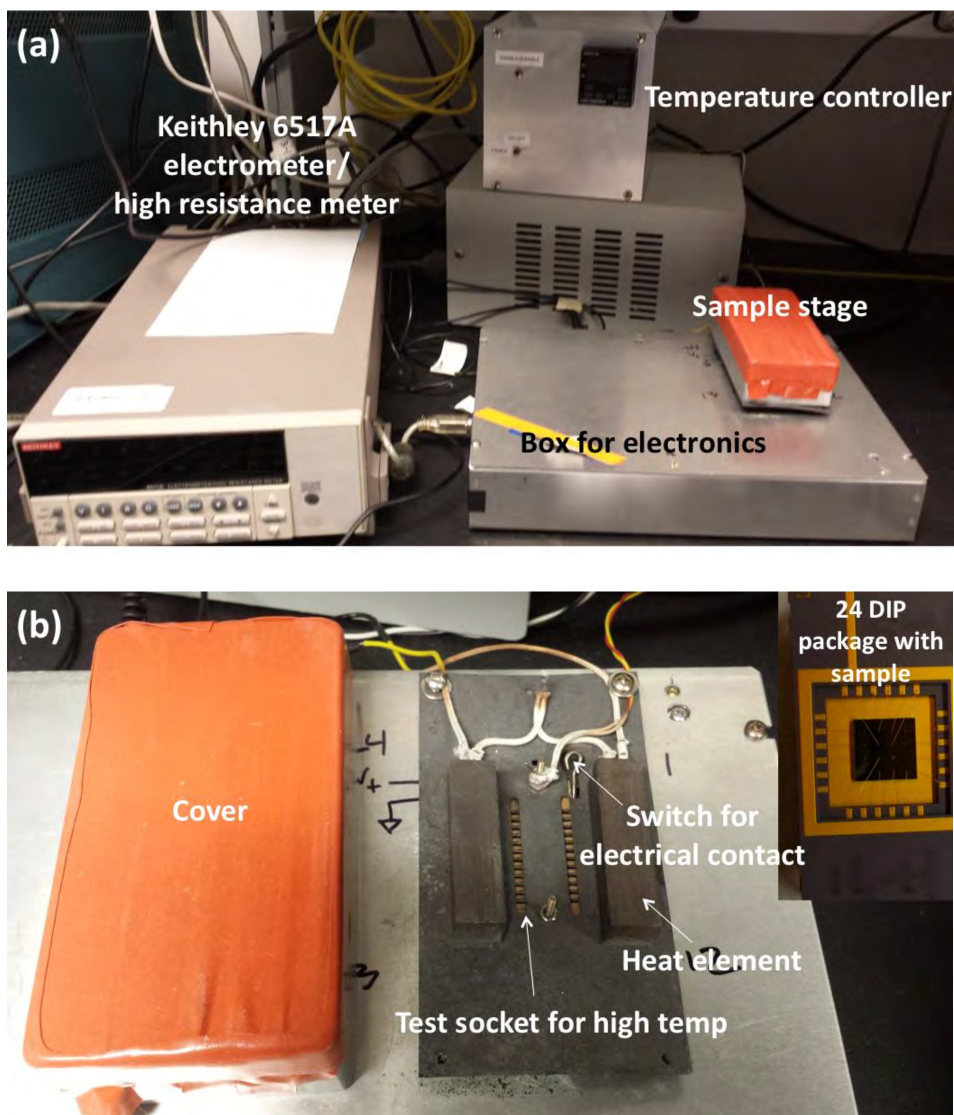

Figure 5.1. Images of (a) HALT system, which was composed of a Keithley 6517A electrometer/high resistance meter, temperature controller and box for electronics and (b) sample stage with wirebonded sample on a 24 pin DIP package

Figure 5.1 shows the image of the HALT system with the high temperature ceramic socket for the 24 pin DIP package. Approximately 15 capacitors per package were wirebonded and five sample sets were measured at various voltages and temperatures. In order to determine

the voltage acceleration factor for failure, packaged samples were measured under three different electric fields of 100, 150 and 225 kV/cm at a constant temperature of 150 ^{o}C. The activation energy was determined from HALT lifetimes at 120 ^{o}C, 150 ^{o}C or 180 ^{o}C at constant field of 225 kV/cm. HALT experiments were performed using Labview software (National Instruments, Austin, TX) to monitor the current-time response at high temperature and voltage. The mean time to failure (MTTF), the activation energy (E_a) and the voltage acceleration factor (N) for failure are inter-related based on the Prokopowicz-Vaskas Lifetime Model: [21]

$$\frac{t_1}{t_2} = \left(\frac{V_1}{V_2}\right)^{-N} \exp\left[\frac{E_a}{k_B}\left(\frac{1}{T_1} - \frac{1}{T_2}\right)\right] \qquad \text{equation (5.1)}$$

where t_1 and t_2 are the MTTF under a voltage V_1 at temperature T_1 and V_2 at temperature T_2, respectively. k_B is Boltzmann's constant, E_a is activation energy and N is the voltage acceleration factor. E_a and N can be used to determine the breakdown mechanism of the patterned PZT thin films.[20][21]

5.2.2. I-V Measurement Procedure

Leakage current measurements were made as a function of the applied voltage using a Hewlett-Packard 4140 PA meter (Agilent Technology, Palo Alto, CA). The steady-state leakage current was evaluated with a step voltage technique.[22] A DC bias was applied and the current was measured after a delay time (t_D) of 60 seconds at each step. The voltage was then increased by 0.5 V and the process was repeated. The measurements were then conducted at several temperatures (room temperature, 50, 75, 100, 125 and 150 ^{o}C).

5.3. Results and Discussion

5.3.1. Reliability of 0.6 μm Thick Patterned PZT (52/48) Thin Films

Figure 5.2 (a) and (b) show the current density – time response of the patterned PZT (52/48) thin films with 2 μm, 5 μm, 8 μm, or 10 μm feature sizes as a function of temperature and applied voltage respectively. The data were taken from HALT data with three different temperatures (120 ^oC, 150 ^oC and 180 ^oC) at 225 kV/cm or three different voltages (100 kV/cm, 150 kV/cm, 225 kV/cm) at 150^oC for all feature sizes (2 μm, 5 μm, 8 μm, and 10 μm). Typically, three regimes can be identified on current – time curves for PZT films: (A) dielectric relaxation in which the current decreases as the time increases. (B) a steady state regime in which the current is constant with time. (C) a resistance degradation regime in which the current increases rapidly.[(10)(11)] Figure 5.2 (a) and (b) illustrate that the change from a steady state regime to resistance degradation occurred gradually. The lifetime (t_f) was defined as the time at which the current increased by two orders of magnitude from the minimum value (J_{min}) of the measured leakage current.[(6)(7)(8)(9)] As expected, as temperature and applied voltage increase, the breakdown takes place more quickly for all feature sizes of the PZT (52/48) thin film.

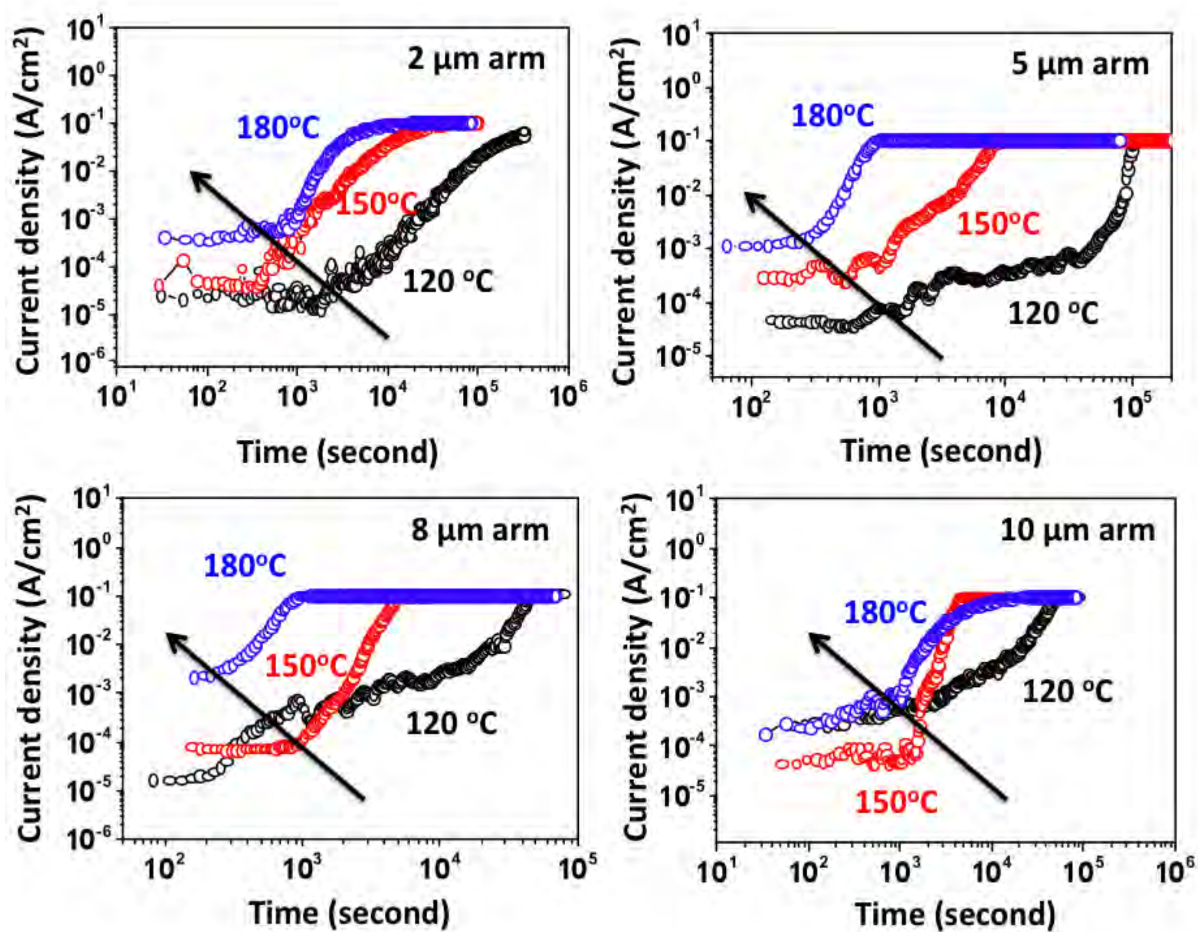

(a)

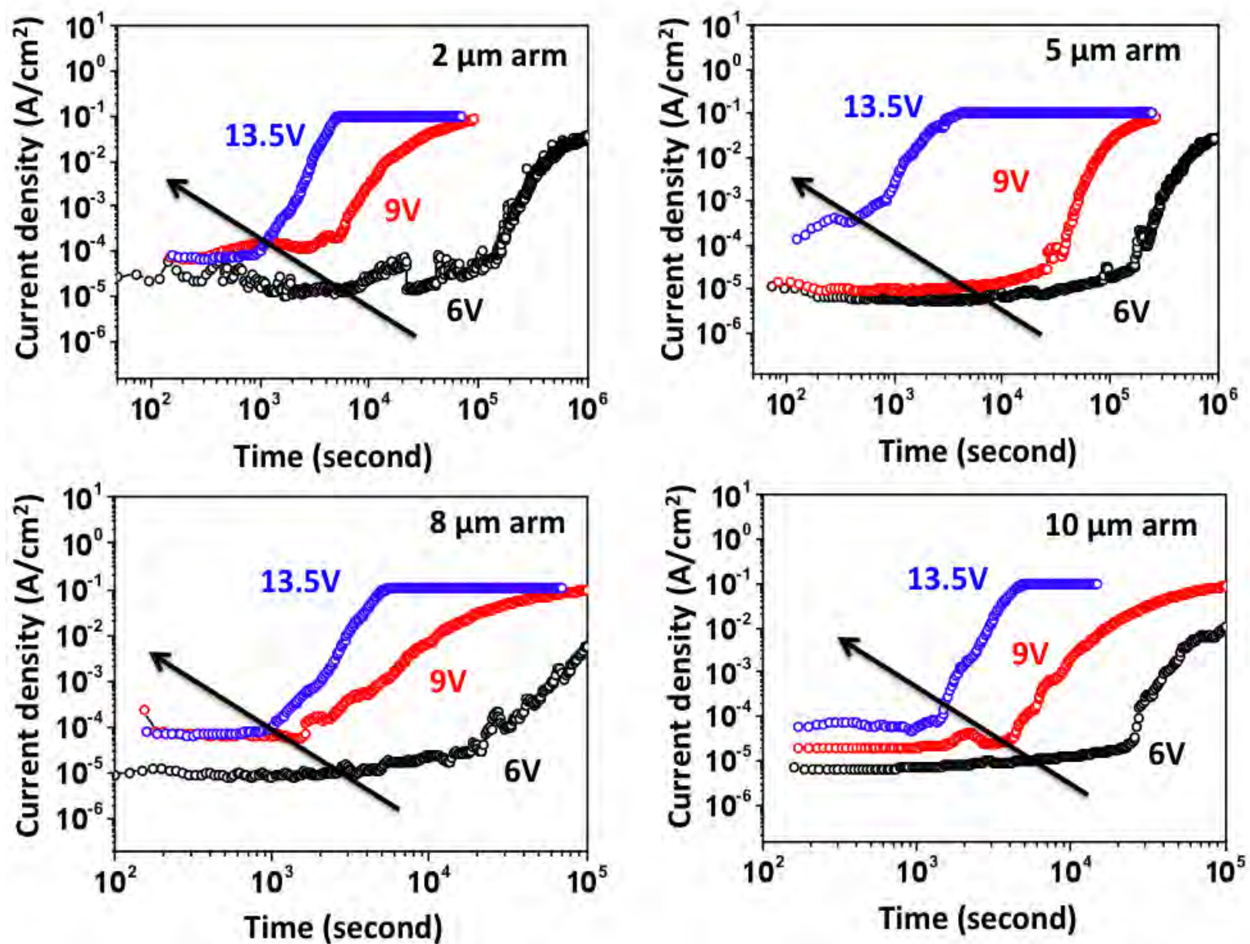

(b)

Figure 5.2. Current density– time characteristics of a patterned 0.6 μm PZT (52/48) thin film measured (a) at various temperatures (120 °C, 150 °C and 180 °C) with applied electric field of 225 kV/cm and (b) at three different voltages (100 kV/cm, 150 kV/cm, 225 kV/cm) at 150 °C

In this research, two principal statistical distributions were used to study the reliability of patterned PZT (52/48) films. One method was the two-parameter Weibull distribution function. The other was a bimodal lognormal distribution. These are described in detail below.

A. Determination of The MTTF (t_{50}) Using The Weibull Lifetime Distribution

The Weibull distribution has been widely used to predict the mean time to failure (MTTF). The two-parameter Weibull cumulative distribution function F(t) for failure is: [23][24][25]

$$F(t) = 1 - \exp[-(\frac{t}{\eta})^{\beta}] \qquad \text{equation (5.2)}$$

where β is the shape parameter, obtained from the slope, η is the scaling parameter and t is the testing time. The shape parameter (β), which is known as the Weibull slope can be expressed differently depending on functions such as the probability density function, the reliability function and the hazard function as shown in Figure 5.3. Figure 5.4 is an example of the effect of the shape parameter (β) on the Weibull distribution. It is called the "bathtub curve" of the failure rate. This curve consists of three regions; for a Weibull distribution with $\beta < 1$, the failure rate decreases as a function of time, as infantile or early-life failures are removed from the system; for Weibull distribution with $\beta = 1$, the failure rate is a constant in the useful life region; for Weibull distribution with $\beta > 1$, failure rate increases as a function of time, due to wear-out failure.

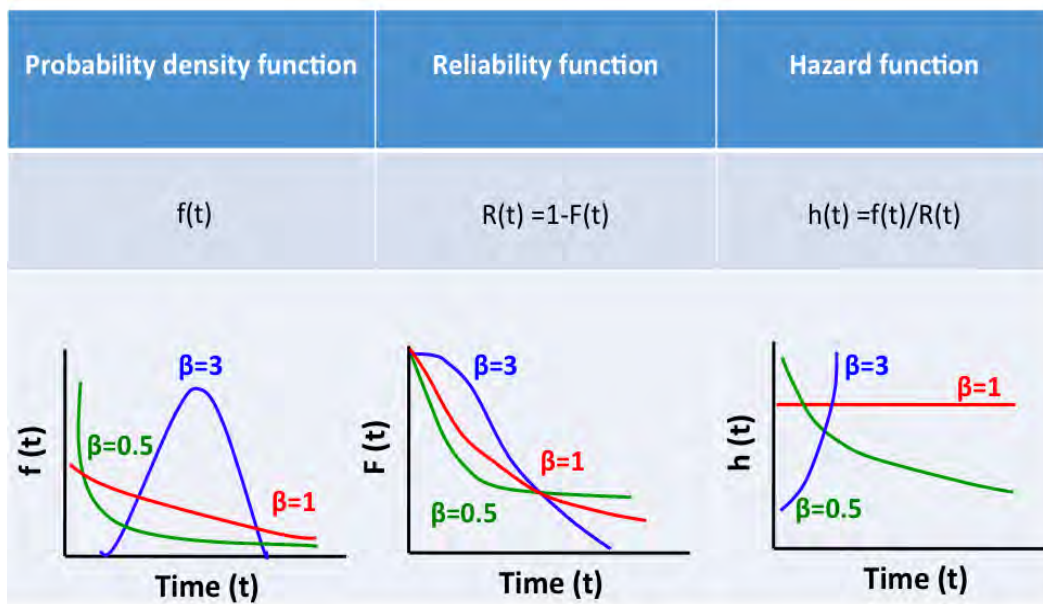

Figure 5.3. Plots comparing the influence of the shape parameters on the Weibull distributions for different functions

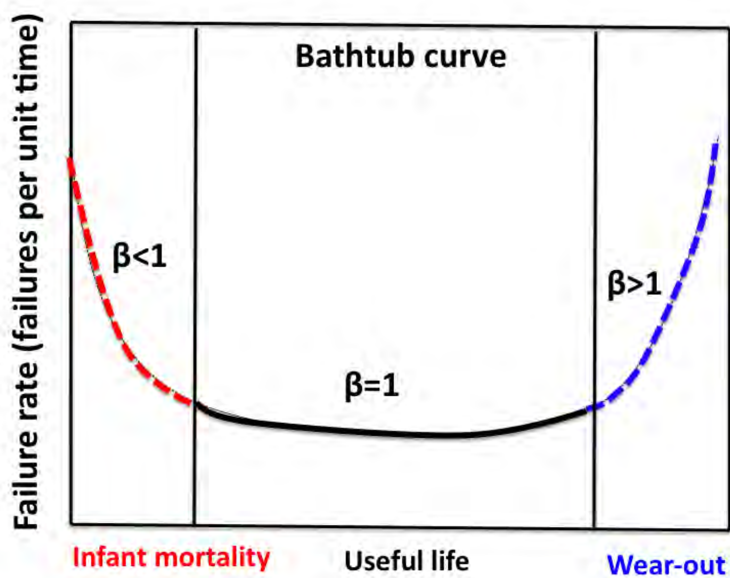

Figure 5.4. The bathtub curve of the failure rate (modified from Ref [18])

The scale parameter (η) can be defined in terms of a statistical dispersion of the probability distribution. If the scale parameter (η) is large, then the distribution is stretched out; if η is small then it will be pushed in toward the left. That is, the larger the scale parameter (η), the more spread out the distribution as shown in Figure 5.5.

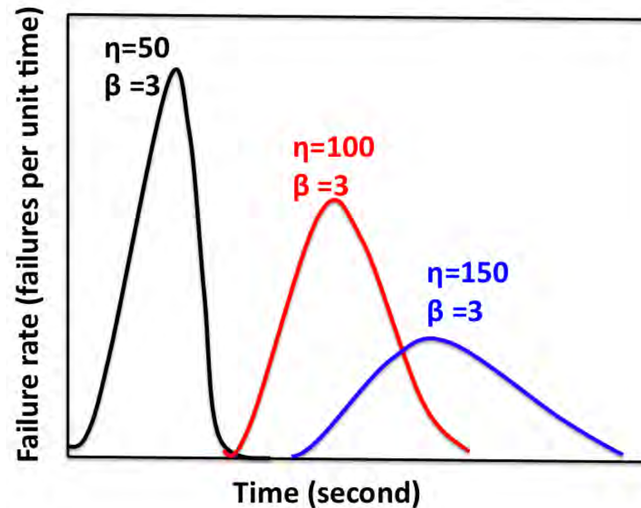

Figure 5.5. Weibull distribution with varying scale parameters (η)

Figure 5.6 shows Weibull plots of mean time to failure of 0.6 μm-thick patterned PZT (52/48) thin films (a) at three different temperatures of 120 ^{o}C, 150 ^{o}C and 180 ^{o}C with 225 kV/cm and (b) at three different electric fields of 100, 150 and 225 kV/cm at a constant temperature of 150 ^{o}C. The black straight lines shown in Figure 5.6 (a) and (b) indicate the data range used to calculate the mean time to failure. In this fitting, infant or early-life failure points are excluded because this failure method is caused by defects in the fabrication. To determine the cumulative failure distribution function (CDF), the median rank ($F_i(t)$) (also referred to as the sampling cumulative distribution parameter) was calculated from the raw data by using

Bernard's approximation expressed as follows: [23][24][25][26][27][28]

$$F_i(t) = \frac{r - 0.3}{N + 0.4} \qquad \text{equation (5.3)}$$

where r is the total sample sequential number, and N is the total sample number. It is essential to reformulate the cumulative probability function in equation (5.2). The reformulated equations are expressed as [18][19][20]:

$$\ln\ln(\frac{1}{1-F(t)}) = \beta\ln t - \beta\ln\eta \qquad \text{equation (5.4)}$$

$$\ln(-\ln R(t)) = \beta\ln(\frac{t}{\eta}) = \beta\ln t - (\beta\ln\eta) \qquad \text{equation (5.5)}$$

where R(t) is the reliability function, R(t) = 1- F(t), β is the shape parameter and η is the scale parameter and t is testing time.

Based on Weibull analysis, the MTTF (mean time to failure) value can be derived from equation (5.4) as described below [23][24][25][26][27][28]

$$MTTF(t_{50}) = \eta \times \exp\left[(\frac{1}{\beta}) \times \ln(-\ln(1 - F(t_{50}))) \right] \qquad \text{equation (5.6)}$$

where $F(t_{50})$= 0.5 which is characterized as the time at which 50% of samples have failed.

The shape parameter (β), the scale parameter (η) and the MTTF value are summarized in Tables 5.2 and 5.3 for all feature sizes of the patterned PZT (52/48) thin films. The time to failure

calculated from the Weibull distribution of the patterned PZT (52/48) films is plotted in Figure 5.6.

Table. 5.2. Mean time to failure (MTTF) and Weibull parameters measured at temperatures of 120 °C, 150 °C or 180 °C for an electric field 225 kV/cm for patterned PZT (52/48) thin films

	Temperature	β	η	t_{50}(hours)
2 μm arm size at applied 225kV/cm	120 °C	1.4 ± 0.02	17 ± 1.2	13.4
	150 °C	3.9 ± 1.2	1.25 ± 0.08	1.14
	180 °C	4.4 ± 0.2	0.48 ± 0.02	0.4

	Temperature	β	η	t_{50} (hours)
5 μm arm size at applied 225kV/cm	120 °C	2.3 ± 0.5	12.6 ± 2.5	10.8
	150 °C	2.6 ± 0.6	1.9 ± 0.2	1.6
	180 °C	4.3 ± 1	0.22 ± 0.02	0.2

	Temperature	β	η	t_{50} (hours)
8 μm arm size at applied 225kV/cm	120 °C	1.3 ± 0.5	8.6 ± 2.9	6.6
	150 °C	3.9 ± 1	1.3 ± 0.1	1.2
	180 °C	10.5 ± 2.6	0.3 ± 0.01	0.28

	Temperature	β	η	t_{50} (hours)
10 μm arm size at applied 225kV/cm	120 °C	2.6 ± 0.5	10.2 ± 1.1	8.9
	150 °C	3.1 ± 0.8	1.1 ± 0.1	1
	180 °C	67± 5.8	0.2 ± 0.007	0.2

Table. 5.3. Mean time to failure (MTTF) and Weibull parameters measured at electric fields of 100, 150 or 225 kV/cm and a constant temperature of 150 °C for patterned PZT (52/48) thin films

	Voltage	β	η	t_{50}(hours)
2 μm arm size at 150°C	6 V	4.8 ± 1.3	86 ± 6.5	79.8
	9 V	2.3 ± 0.3	25 ± 0.4	21.3
	13.5 V	3.9 ± 1.2	1.25 ± 0.08	1.1

	Voltage	β	η	t_{50}(hours)
5 μm arm size at 150°C	6 V	2.2 ± 0.5	75 ± 11.6	63.5
	9 V	2.9 ± 0.2	15.8 ± 1.7	13.9
	13.5 V	2.6 ± 0.6	1.9 ± 0.2	1.6

	Voltage	β	η	t_{50}(hours)
8 μm arm size at 150°C	6 V	1.26 ± 0.27	34 ± 8.6	25.8
	9 V	1.06 ± 0.24	16.6 ± 5.2	11.7
	13.5 V	3.9 ± 1	1.32 ± 0.11	1.2

	Voltage	β	η	t_{50}(hours)
10 μm arm size at 150°C	6 V	5.5 ± 1.1	16.6 ± 0.9	15.5
	9 V	1.8 ± 0.4	7.6 ± 1.2	2
	13.5 V	3.1 ± 0.8	1.1 ± 0.1	1

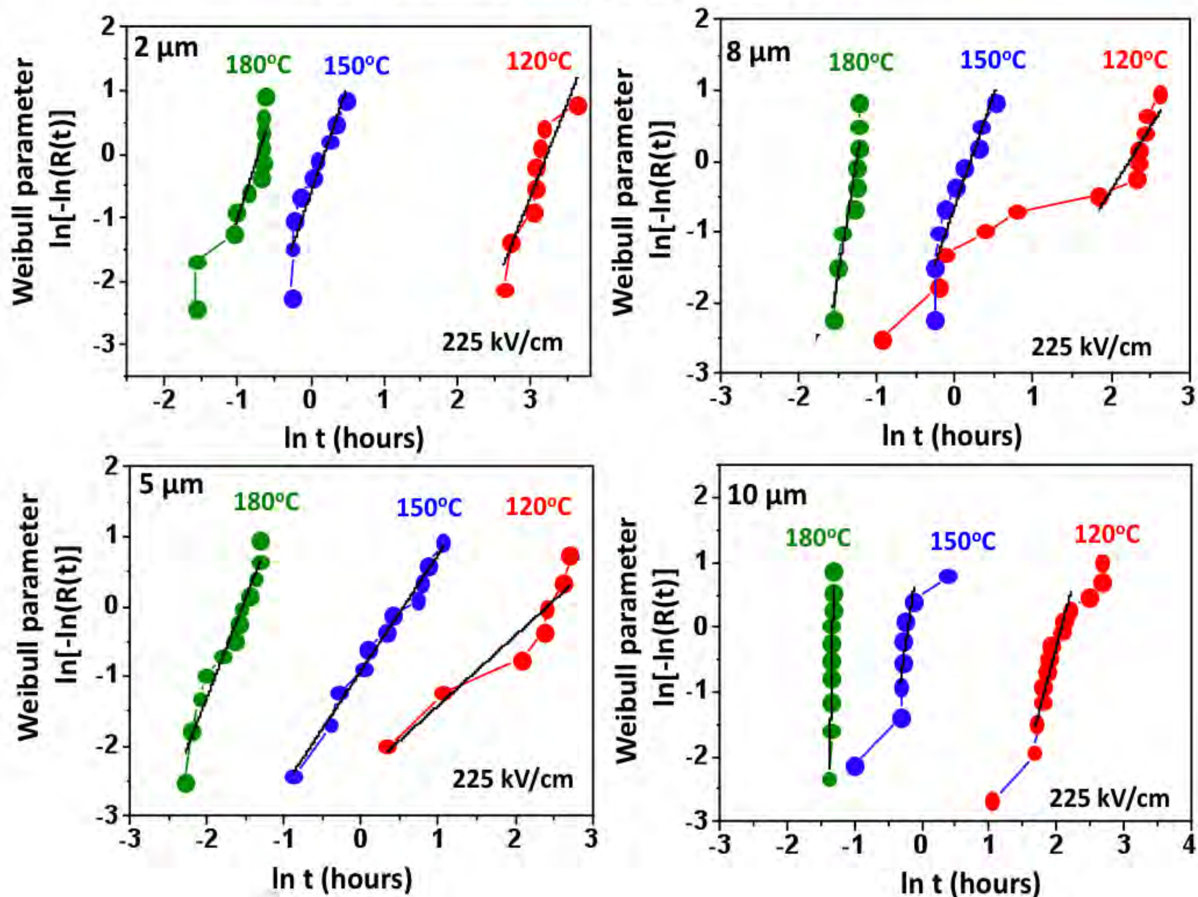

(a)

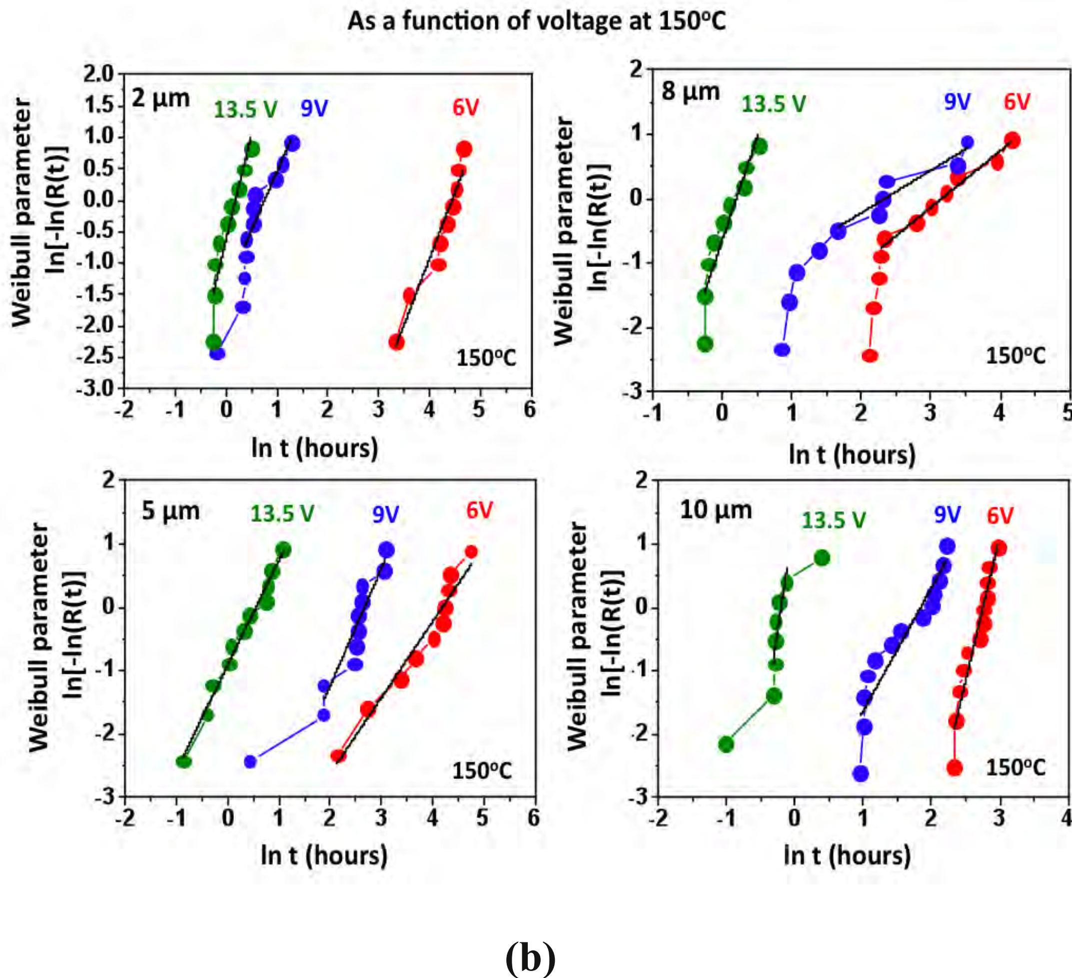

(b)

Figure 5.6. Weibull plots of time to failure of patterned PZT (52/48) thin film (a) at three different temperatures of 120 ^{o}C, 150 ^{o}C and 180 ^{o}C with 225 kV/cm and (b) at three different electric fields of 100, 150 and 225 kV/cm at constant temperature of 150 ^{o}C

Figure 5.7 exhibits the MTTF values calculated from the Weibull analysis at three different temperatures at constant voltage and three different voltages at constant temperature. The figure shows the variation of MTTF under the lowest measured temperature and voltage conditions. It should be pointed out that the characteristic time to failure increased with

decreasing feature size as a function of temperature and voltage. The reason for this behavior will be discussed later with the activation energy and FE-SEM images.

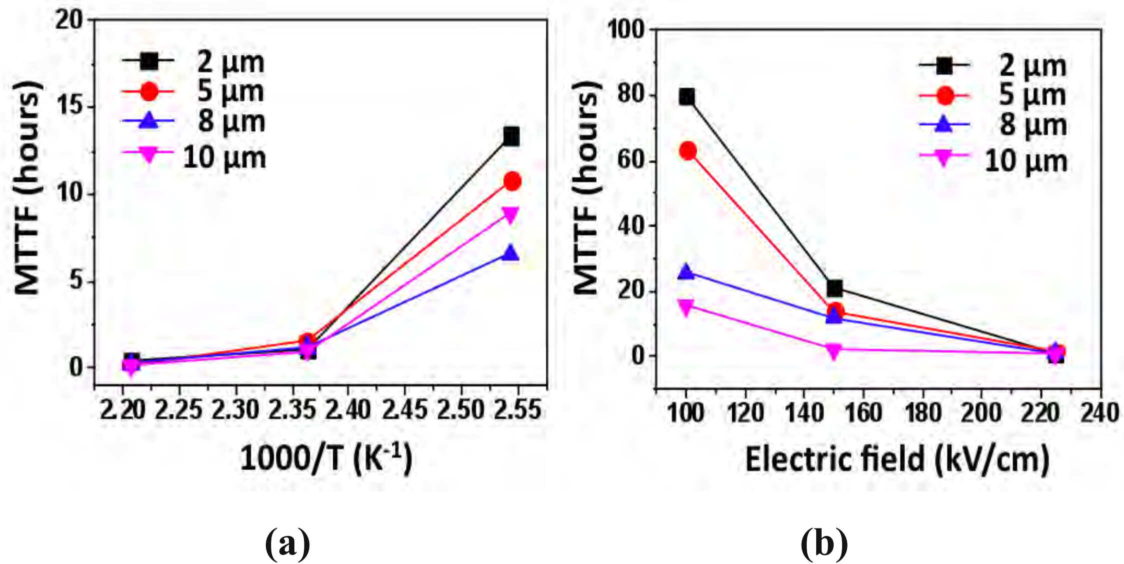

Figure 5.7. Mean time to failure, calculated from Weibull distribution function, as a function of (a) temperature at 225 kV/cm and (b) electric field at 150 °C for 0.6 μm thick patterned PZT (52/48) thin film

B. Determination of the MTTF (t_{50}) Using Lognormal Distribution

As an alternative, a bimodal lognormal distribution, which can describe the presence of infant failure populations, was applied to determine the MTTF using a cumulative percent failure plot that is S shaped [(23)]. The first step in graphical analysis is listing the cumulative number of failures and the cumulative percent failures as shown in Table 5.4.

Table 5.4. Example of failure data with cumulative frequency and percentage

Failure time (hours)	Cumulative number of failures	Cumulative percent failure
0.5	1	10
1.8	2	20
5	3	30
17	4	40
56	5	50
89	6	60
95	7	70
137	8	80
180	9	90
235	10	100

The cumulative number of failures is the result of the addition of the number of failure events. The cumulative percent failure is the total number of failure events as a percentage of the total events: [23][27]

$$\textbf{Cumulative percent failure} = \left(\frac{\text{Cumulative number of failure}}{\text{Total number of test units}} \right) \text{X } 100$$

equation (5.7)

The cumulative percent failure (probability of failure) was then plotted as a function of the log time to failure on the x-axis using a lognormal graph. Then, the 50% failure time (MTTF) was obtained directly from the plot. An S-shaped curve is found when there are two failure modes:

the lower portion of the S-shaped curve is due to infant failures associated with processing defects, while the upper portion describes the failure of the better part of the dielectric. The MTTF and standard deviation (σ_{ln}) can be determined from the main portion using a linear extrapolation. The probability of failure for the S-shaped curve can be expressed as (23)(28):

$$F(t) = p_A F_{FR}(t) + (1 - p_A) F_M(t) \qquad \text{equation (5.8)}$$

where p_A is the fraction of the infant or freak distribution, and $F_{FR}(t)$ is the freak distribution and $F_M(t)$ is main part of distribution respectively. p_A can be determined as the inflection point which is an abrupt changing in slope between the lower and upper portions of the S-shaped curve. Figure 5.8 is an example of S-shape curve of bimodal lognormal distribution, which was taken from reference [23] (23)(27)(28).

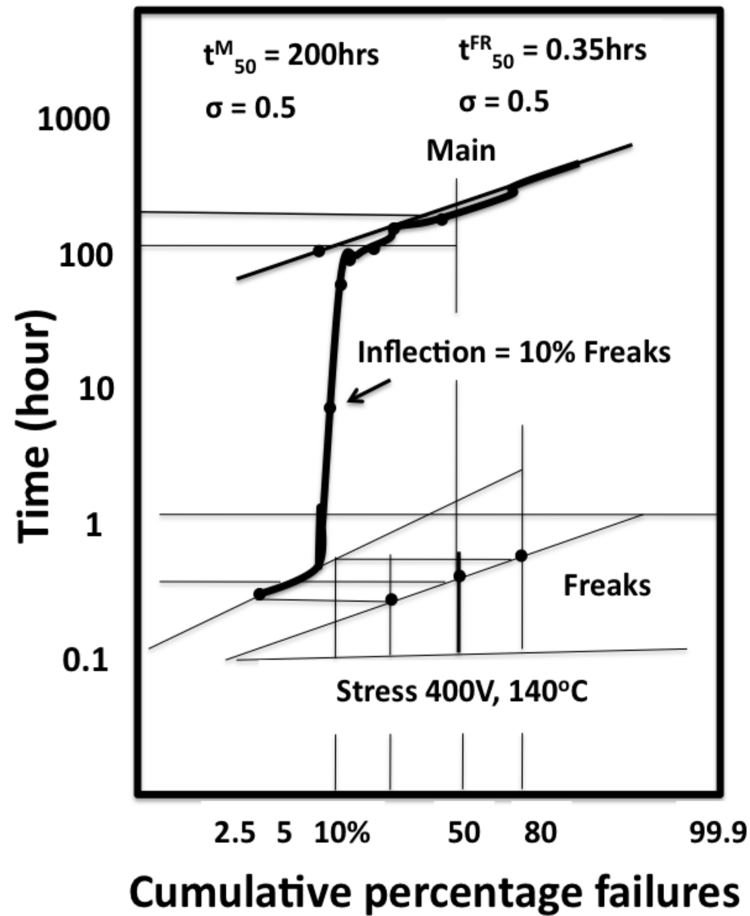

Figure 5.8. The S-shaped curved of cumulative percent failure plot (adapted from reference [23])

Based on this method, the MTTF (t_{50}) was calculated from the patterned PZT HALT data.

Figure 5.9 shows the cumulative percent failure plot of an 8μm feature size PZT (52/48) film, for an experiment conducted at 120 ^{o}C and 225 kV/cm.

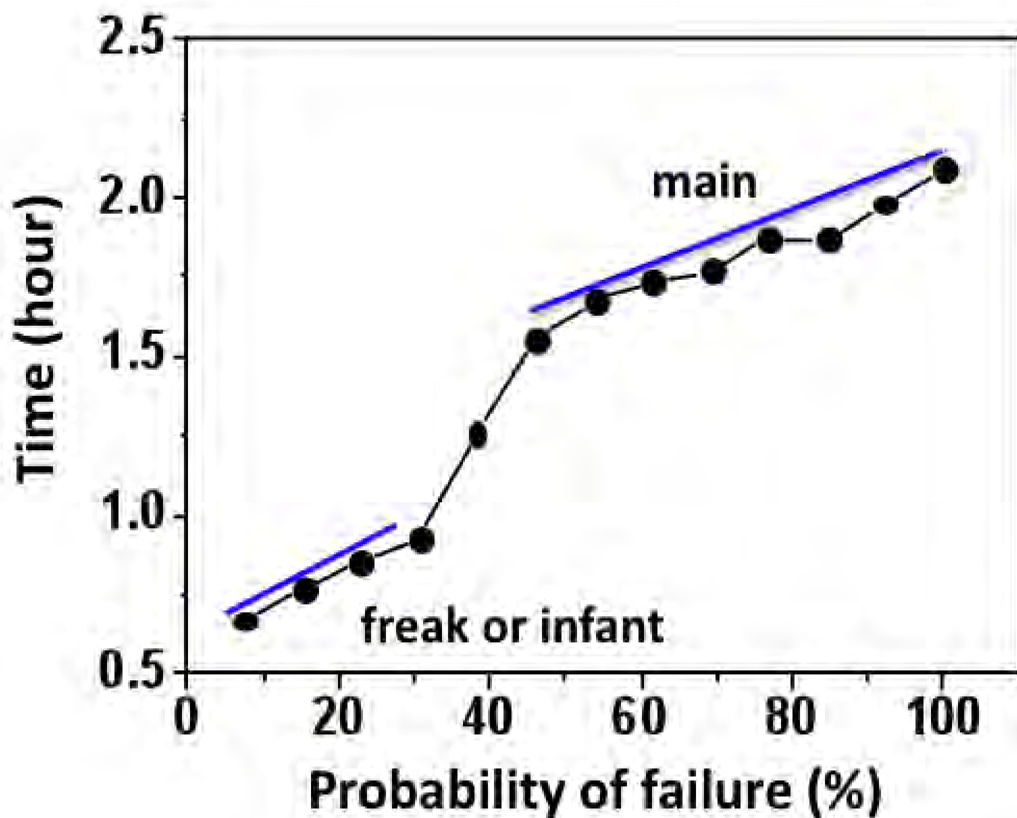

Figure 5.9. Plot of cumulative percentage failure versus time from HALT data of 5 μm feature size PZT (52/48) thin film measured at 150 °C and 225 kV/cm.

Table 5.5 and Figure 5.10 summarize all of the data. As shown in Figure 5.10, the MTTF values estimated from the cumulative percentage failure distribution show the same trend as the MTTF calculated from the Weibull distribution; that is the characteristic time to failure t_{50} increased with decreasing feature size as a function of temperature and voltage.

Table. 5.5. Mean time to failure (MTTF) obtained from a cumulative percentage failure plot measured at electric fields of 100, 150 and 225 kV/cm at a constant temperature of 150 °C and also at 120 °C, 150 °C and 180 °C at constant electric field 225kV/cm for 0.6 μm thick patterned PZT (52/48) films.

	Temperature	t_{50}(hours)		Voltage	t_{50}(hours)
2 μm arm size at applied 225kV/cm	120°C	20.3	2 μm arm size at 150°C	6 V	77.6
	150°C	1.0		9 V	29.8
	180°C	0.5		13.5 V	1.0

	Temperature	t_{50}(hours)		Voltage	t_{50}(hours)
5 μm arm size at applied 225kV/cm	120°C	10.7	5 μm arm size at 150°C	6 V	61.8
	150°C	1.6		9 V	12.6
	180°C	0.2		13.5 V	1.6

	Temperature	t_{50}(hours)		Voltage	t_{50}(hours)
8 μm arm size at applied 225kV/cm	120°C	8.2	8 μm arm size at 150°C	6 V	16.2
	150°C	1.0		9 V	7.2
	180°C	0.3		13.5 V	1.0

	Temperature	t_{50}(hours)		Voltage	t_{50}(hours)
10 μm arm size at applied 225kV/cm	120°C	6.8	10 μm arm size at 150°C	6 V	13.7
	150°C	0.7		9 V	4.4
	180°C	0.1		13.5 V	0.7

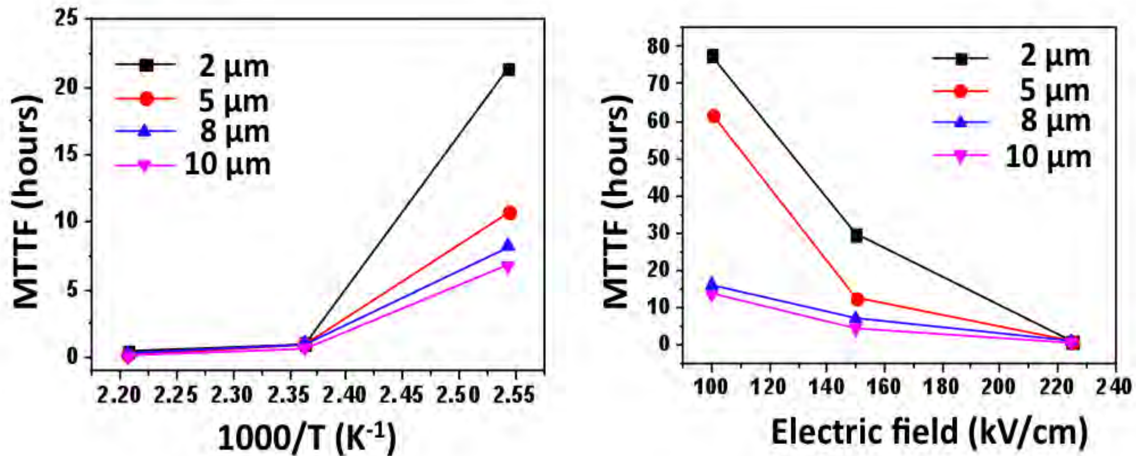

Figure 5.10. Mean time to failure, calculated from the cumulative percentage failure plot, as a function of (a) temperature at 225 kV/cm and (b) electric field at 150 ^{o}C for 0.6 μm thick patterned PZT (52/48) thin film.

C. Determination of Activation Energy

The activation energy which controls the degradation process can be determined from an Arrhenius model reduced from equation (5.1).[(29)]

$$\frac{t_1}{t_2} = \exp\left[\frac{E_a}{k}\left(\frac{1}{T_1} - \frac{1}{T_2}\right)\right] \qquad \text{equation (5.9)}$$

where t_1 and t_2 are the time to failure of each point, E_a is the activation energy, k is Boltzmann's constant and T is the absolute temperature. The activation energy was obtained from the plot of the relationship between the logarithm of MTTF and reciprocal of absolute temperature of 0.6 μm thick patterned PZT (52/48) thin film. This test was conducted with three different

temperatures of 120 °C, 150 °C and 180 °C at constant electric field of 225 kV/cm. As shown in Figure 5.11, the ranges of activation energy for all feature sizes are 0.82 eV ~ 1.1 eV. The activation energy is slightly higher for increasing feature size. Some reports ascribe an activation energy from 0.82 eV ~ 1 eV to the movement of oxygen vacancies, but the degradation mechanism associated with an activation energy above 1 eV is still debated. Here, a working model was developed in which there were contributions from the sidewall and the bulk of the film.

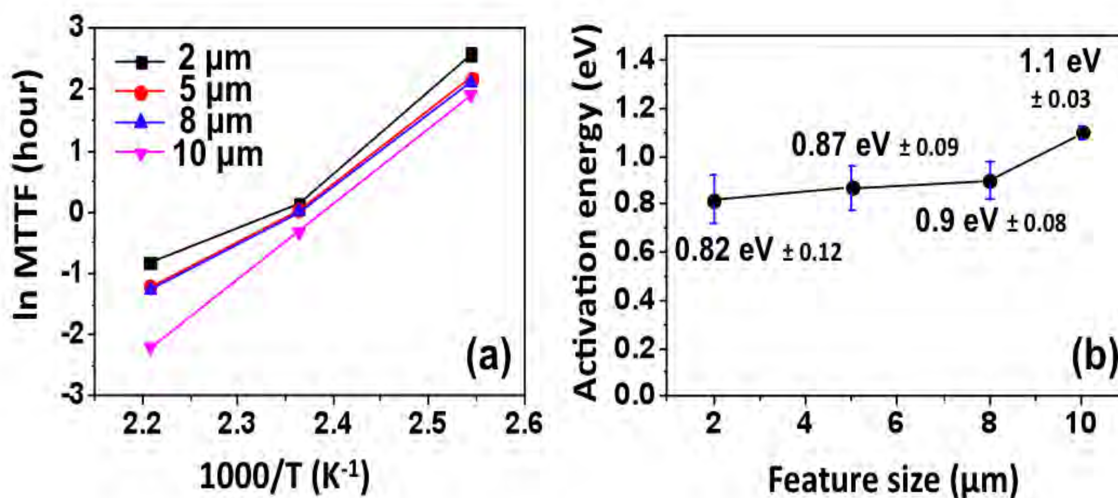

Figure 5.11. Plots of (a) the ln mean time to failure vs 1000/T, (b) the activation energy of all feature sizes under three different temperatures of 120 °C, 150 °C and 180 °C at electric field of 225 kV/cm

It is useful to compare the mean time to failure and activation energy between blanket and patterned PZT thin films. It should be expected that the fabrication processes associated with the patterning could influence the failure mechanisms and the resulting behavior. For example, it was found that the aging behaviors differed between PZT thin film patterned by reactive ion etching and argon ion milling as will be mentioned in chapter 6. To begin examining this, the

similarities and differences in properties between blanket film and patterned PZT film are compared. Table 5.6 shows a comparison between blanket film PZT thin films and films patterned into 2 μm arm sizes.

Table 5.6. Summary of comparisons of results between blanket film PZT thin films and patterned 2 μm arm size PZT (52/48) thin film

	Fabrication	ε_r	**tanδ (%)**	P_r **(μC/cm^2)**	E_c **(kV/cm)**
Polcawich *et al*[27] 1 μm thick PZT (52/48) film	Conventional process	1000-1100	2 - 4	20-25	38-42
This work (0.6 μm continuous PZT (52/48) films	Conventional process	960-900	1.5 - 2.5	20	50
This work (0.6 μm thick PZT (52/48) for 2 μm feature size	Reactive ion etching	1115-1100	2 - 5	35.7	91

Polcawich et al. fabricated PZT (52/48) thin film using chemical solution deposition; the platinum top electrode was deposited by sputtering through a shadow mask.[28] As mentioned in chapter 4, in this work, the PZT thin films were deposited by chemical solution deposition and after film deposition, lithography, Ni electroplating and reactive ion etching were performed. As shown in Table 5.6, the blanket film and patterned PZT film have similar dielectric properties such as dielectric constant and dielectric loss, however, patterned PZT film showed higher remanent polarizations (P_r) and coercive fields (E_c) than the blanket films. As mentioned in chapter 4, the higher remanent polarization of patterned PZT film in 2 μm feature size is due to a

declamping effect.

Table 5.7. The comparison of lifetime between blanket films PZT thin films and patterned 2 μm arm size PZT (52/48) thin film

	HALT conditions		t_{50}
	Electrical field	Temperature	
Duane Dimos *et al.* [10]	375 kV/cm	100 °C	30h
	375 kV/cm	125 °C	10 h
	375 kV/cm	170 °C	4 h
Polcawich *et al.* [27]	250 kV/cm	120 °C	136 h
	250 kV/cm	150 °C	17 h
	250 kV/cm	180 °C	6.5 h
Garten *et al.* [28]	150 kV/cm	160 °C	45.2 h
	150 kV/cm	180 °C	10.2 h
	150 kV/cm	200 °C	2.98 h
2 μm feature size patterned PZT	225 kV/cm	120 °C	13.4 h
	225 kV/cm	150 °C	1.1 h
	225 kV/cm	180 °C	0.4 h

The higher coercive field (E_c) in the 2 μm feature size patterned PZT films would be consistent with the switching measurement sampling more pinning sources in the films. It is possible, for example, that the patterned PZT thin film has more mobile oxygen vacancies than films prior to patterning, even after recovery annealing at 500 °C for 1 minute in the RTA. A second possibility is that on partial declamping of the film, a larger fraction of domains are

switchable than was possible in blanket films; these new switching entities may have been more heavily pinned, The first of these possibilities would be consistent with the observation that on average, patterned PZT films have shorter lifetimes than those of blanket films reported in Table 5.7. [(10)(28)(29)]. It is also possible that during the Ni electroplating and etching processes, the top electrode might be damaged. Field concentrations associated with damage to the top electrode would also be expected to shorten lifetimes in patterned PZT film. Any such defects would be expected to be similar in concentration for all feature sizes. However, no visible damage to the top electrode was detected by optical microscopy.

Based on the comparisons in Table 5.8, it is inferred that there are two potential failure paths associated with patterned features: the sidewall and the bulk of the film. These two are described in detail below

Table 5.8. Comparison between 2 μm and 10 μm feature size PZT (52/48) thin films

	2 μm feature	**10 μm feature**
Activation energy	0.82 eV ± 0.12	1.1 eV ± 0.03
MTTF (hour) (225 kV/cm, 120°C)	13.4 h	8.9 h
MTTF (hour) (100 kV/cm, 150°C)	79.8 h	15.5 h
P_r (μC/cm^2)	35	29
Density of domain walls	Less	More
Sidewall damage & dangling bonds	More	Less
Unfilled trap center	More	Less
Concentration of defects in the bulk of the film	Same	Same

1. Sidewall effect:

The degradation of patterned PZT (52/48) thin film could, in principle, be driven by the defects in the sidewall region. The 2 μm feature size presumably has more sidewall damage and induced dangling bonds that may act as trap centers than any other sample. In contrast, it should be assumed that the concentrations of bulk defects are the same for all feature sizes because all of the samples were fabricated from the same blanket film. If these hypotheses are true, then there could be more unfilled trap sites for the 2 μm feature size parts. If so, it should take longer for 2 μm feature size parts to fill these traps at the same leakage currents. This would account for the observation that the 2 μm feature size had the longest MTTF. It is also possible that the smaller activation energy for failure observed for the 2 μm feature size (~0.82 eV) is because the trap centers at the sidewalls provide a broader distribution of possible sites for hopping. It could be that the trapping/detrapping process at the sidewall would be dominant degradation mechanisms in patterned PZT (52/48) thin film for smaller feature size. Figure 5.12 shows a schematic of the sidewall effect for 2 μm feature size.

2. Bulk effect

A second failure pathway can occur through the "bulk" of the ferroelectric. If infant failures are screened out, then macroscopic defects can be excluded from consideration. Thus, it is presumed that oxygen vacancies, electrons, holes, other point defects, and/or barriers at the dielectric/electrode interface will dominate the failure process. It is presumed that in the bulk, carriers can be pinned at domain walls. Therefore, trapped charge carriers at domain walls can act as electrical paths, so the enhanced defect migration leading to failure might be expected as

shown in Figure 5.12.[30][31][32] Based on the higher remanent polarization observed in the P-E hysteresis loops in patterned PZT (52/48) films with finer feature sizes, the domain structure depends on the degree of release from the clamping induced by the underlying substrate. That is, with smaller feature sizes, more out of plane domain orientation can be achieved. One way that this could occur is if the 2 μm arm size has a lower density of domain walls than larger feature sizes because the substrate-imposed clamping is reduced in the 2 μm feature size.

Moreover, it is anticipated that the average in-plane stress state of the antenna features decreases with the arm width. This is because as-processed PZT films on Si substrates are typically under 100 – 150 MPa tensile stress.[33][34][35] Some of this stress is relaxed on lateral patterning. Based on these two factors, the 10 μm arm size has a higher density of domain walls and a larger residual tensile stress in the bulk of the film that the 2 μm arm size. As will be described below, there is not significant evidence for microcracking associated with the failure process. Thus, it is anticipated that the average stress state may not be dominant in accounting for the differences in lifetimes with feature size.

Based on this, it is hypothesized that the shorter lifetime observed with increasing feature size (especially notable for the 10 μm arm size) is due to the possibility of a higher density of domain walls acting as conduction pathways. The activation energy for failure might then be correlated with the activation energy for motion of the carriers. Since the activation energy (~ 1 eV) is higher than that reported for oxygen vacancy migration (~0.6 eV)[2][10], it is possible that detrapping of carriers from domain walls dominates the response.

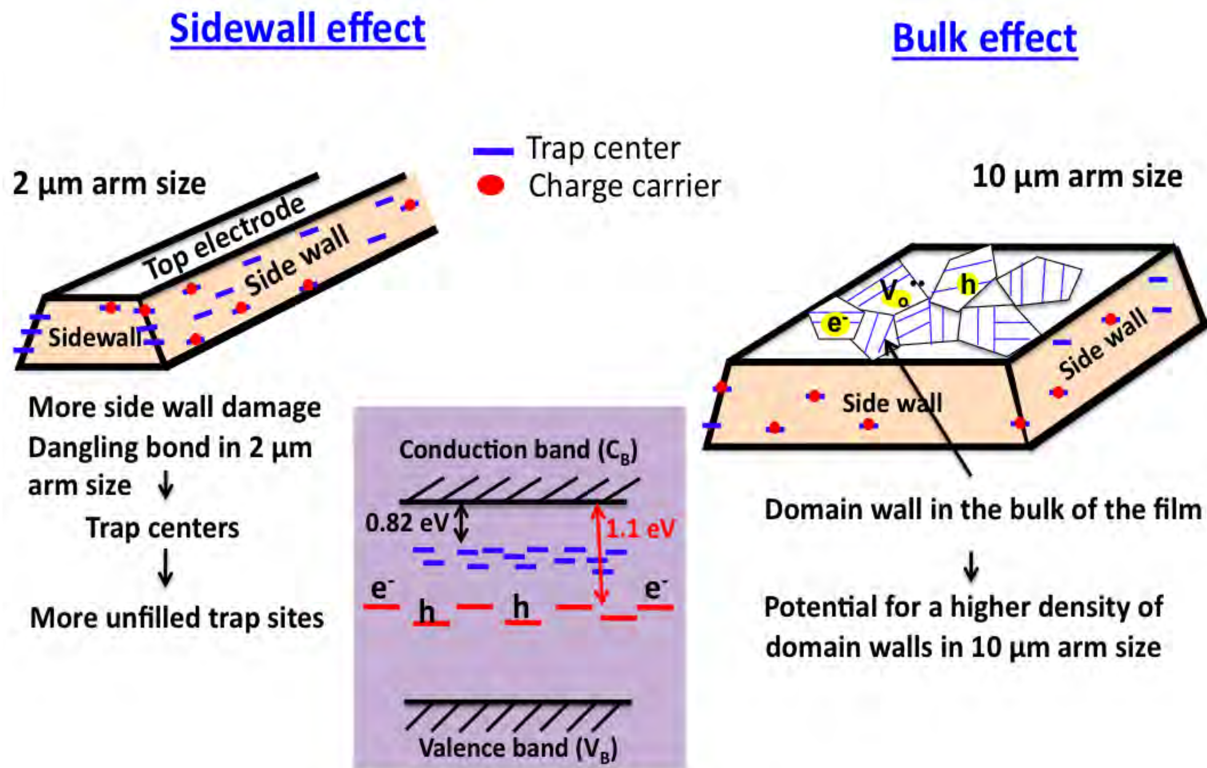

Figure 5.12. Schematic of mechanisms associated with failure of antennae shaped 2 µm arm size and 10 µm arm size along with a possible energy band diagram

To remove/minimize sidewall damage, wire bonded samples were coated by atomic layer deposition (Savannah 200 ALD system, Cambridge Nanotech, MA). The HfO_2 ALD coating parameters are summarized in Table 5.9.

Table 5.9. Atomic layer deposition parameters for the patterned PZT films

HfO_2 ALD	Conditions
Metal-precursors	Tetrakis hafnium ($Hf(NMe_2)_4$)
Precursor dose time (s)	0.2 sec
Purge time (s)	15 sec
Water does time (s)	0.015 sec
Purge time (s)	10 sec
Temperature	200°C
Growth rate	1.01 Å/cycles

After HfO_2 ALD coating, HALT measurements were conducted using the same conditions as the non-ALD coated samples. Figure 5.13 shows that Weibull plots of time to failure of patterned PZT (52/48) thin film at the same field (225 kV/cm) for three different temperatures: 120 °C, 150 °C and 180 °C and with isothermal condition (150 °C) at three different electric fields of 100, 150 and 225 kV/cm. The tendencies for the Weibull plots for HfO_2 ALD coated films are the same as for non-ALD coated samples. Tables 5.10 and 5.11 summarize the Weibull parameters and mean time to failure.

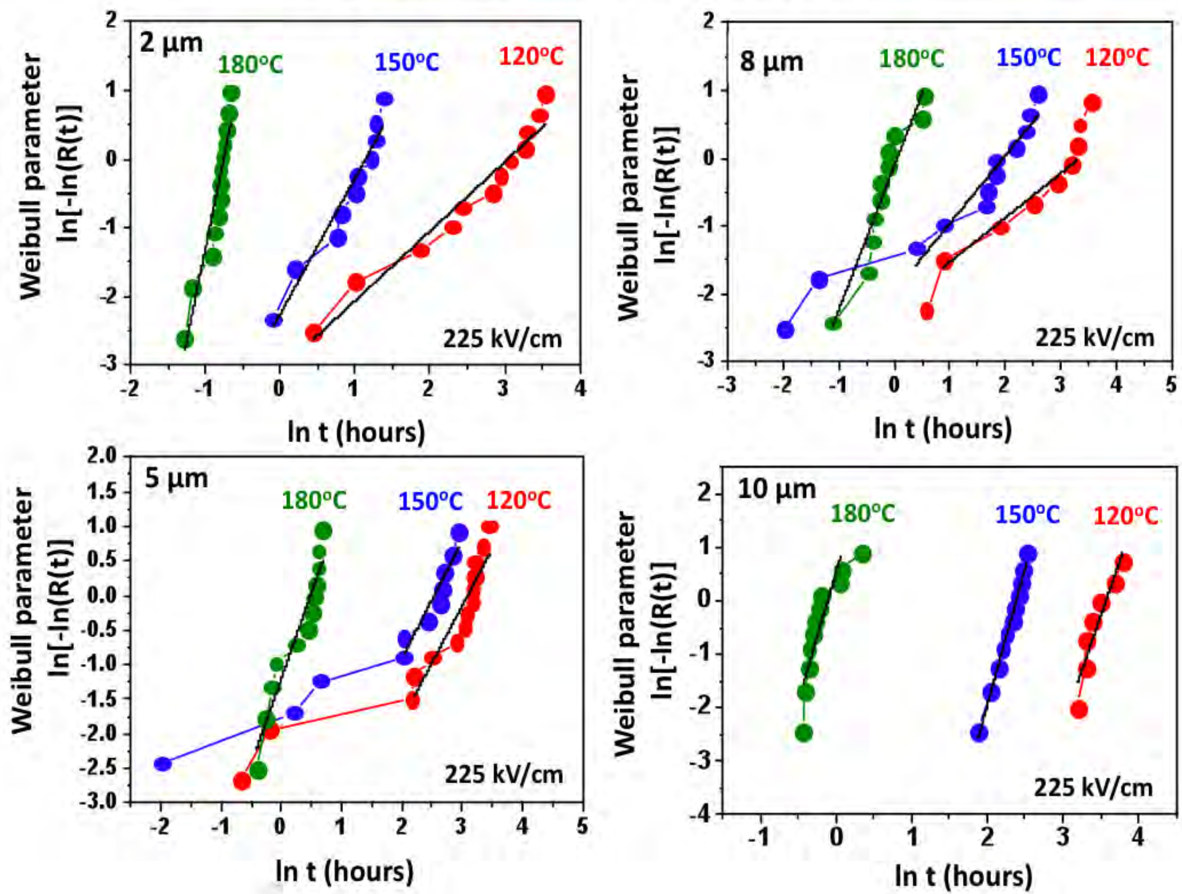

(a)

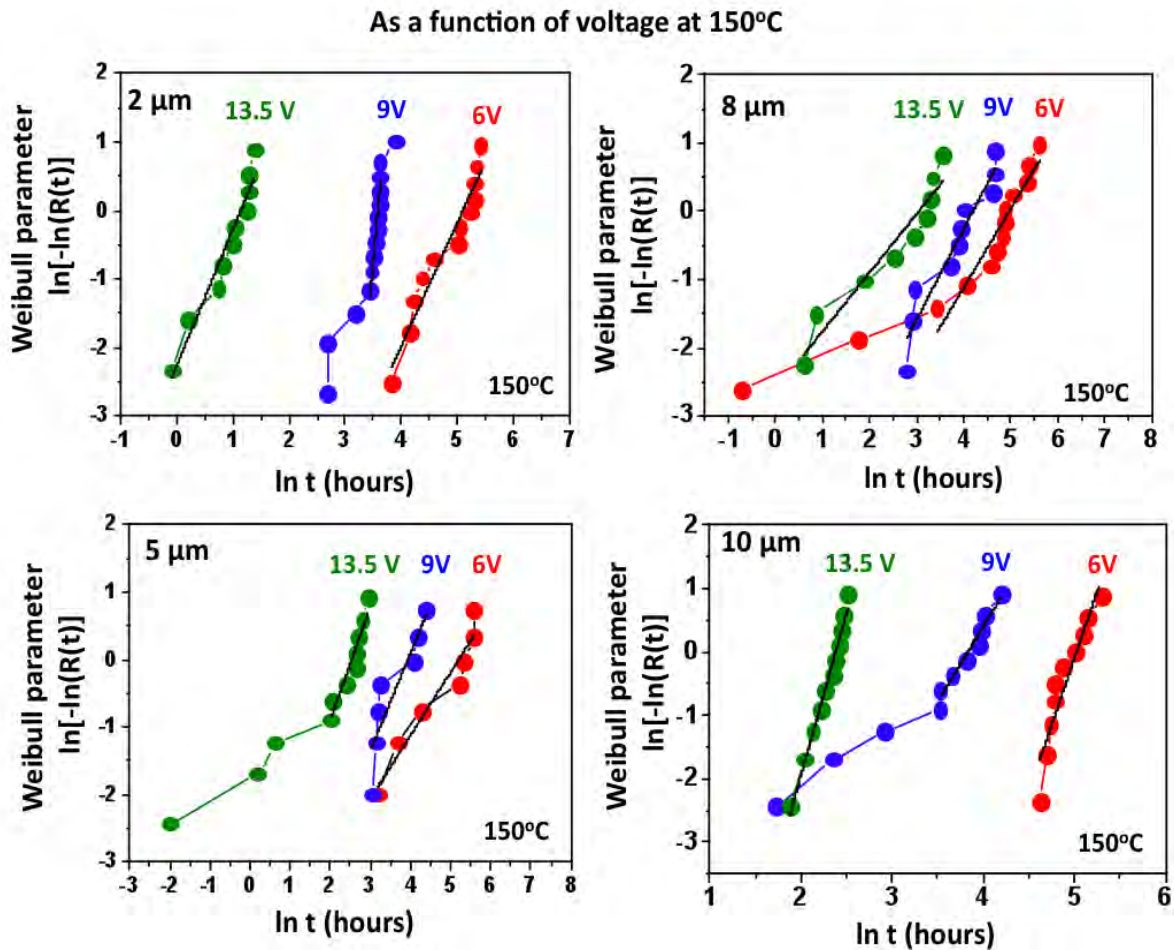

(b)

Figure 5.13. Weibull plots of time to failure of HfO_2 ALD coated PZT (52/48) thin film (a) at three different temperatures of 120 °C, 150 °C and 180 °C with 225 kV/cm and (b) at three different voltages of 100 kV/cm, 150 kV/cm and 225 kV/cm with 150 °C

Table 5.10. Mean time to failure (MTTF) and Weibull parameters measured at (a) three different temperatures of 120 °C, 150 °C and 180 °C with 225 kV/cm for ALD coated PZT (52/48) thin films

	Temperature	β	η	t_{50} (hours)
2 μm arm size at applied 225kV/cm	120°C	1.4 ± 0.02	22 ± 0.4	18.2
	150°C	3.0 ± 0.1	3.2 ± 0.2	2.8
	180°C	8.2 ± 0.7	0.53 ± 0.02	0.4

	Temperature	β	η	t_{50} (hours)
5 μm arm size at applied 225kV/cm	120°C	1.5 ± 0.02	21 ± 0.5	18.9
	150°C	1.6 ± 0.04	7.5 ± 0.6	10.4
	180°C	0.53 ± 0.03	1.51 ± 0.02	0.7

	Temperature	β	η	t_{50} (hours)
8 μm arm size at applied 225kV/cm	120°C	2.0 ± 0.3	21 ± 0.5	19
	150°C	1.17 ± 0.04	7.0 ± 0.4	6.3
	180°C	2.2 ± 0.1	1.18 ± 0.03	0.5

	Temperature	β	η	t_{50} (hours)
10 μm arm size at applied 225kV/cm	120°C	1.93 ± 0.03	25 ± 0.9	21.9
	150°C	6.5 ± 0.4	11 ± 0.3	10.7
	180°C	2.9 ± 0.2	1.1 ± 0.07	0.6

Table 5.11. Mean time to failure (MTTF) and Weibull parameters measured at three different electric fields of 100, 150 and 225 kV/cm at constant temperature of 150 ^oC for HfO_2 ALD coated PZT (52/48) thin film

	Voltage	β	η	t_{50} (hours)
2 μm arm size at 150°C	6 V	2.4 ± 0.4	169 ± 2.2	145.6
	9 V	2.7 ± 0.2	39 ± 2.7	34.1
	13.5 V	3.9 ± 1.2	1.25 ± 0.08	1.1

	Voltage	β	η	t_{50} (hours)
5 μm arm size at 150°C	6 V	1.6 ± 0.04	183 ± 3.4	145.7
	9 V	2.1 ± 0.06	56 ± 2.1	46.2
	13.5 V	1.6 ± 0.04	7.4 ± 0.6	5.9

	Voltage	β	η	t_{50} (hours)
8 μm arm size at 150°C	6 V	1.11 ± 0.03	131 ± 2.5	93.4
	9 V	1.83 ± 0.02	69 ± 2.2	56.3
	13.5 V	1.14 ± 0.04	7.0 ± 0.4	5.0

	Voltage	β	η	t_{50} (hours)
10 μm arm size at 150°C	6 V	3.8 ± 0.4	163 ± 3.5	147.3
	9 V	1.51 ± 0.03	51 ± 2.4	39.5
	13.5 V	6.4 ± 0.4	11.0 ± 0.3	10.4

Figure 5.14 shows comparisons of the MTTF values and activation energies of HfO_2 coated and uncoated PZT (52/48) thin film determined from the Weibull analysis. As shown in Figure 5.14 (a) and (b), after ALD coating, the lifetime of all features sizes improves. In addition, activation energies are very similar for all feature sizes. It should be pointed out that contrary to results of uncoated PZT films, there is no consistent feature size dependence for the MTTF, though there may be a weakly lower MTTF for the 2 micron feature sizes. These results suggest that after ALD coating, the sidewall damage is partially recovered, so the effect of sidewall damage on the breakdown mechanism is reduced.

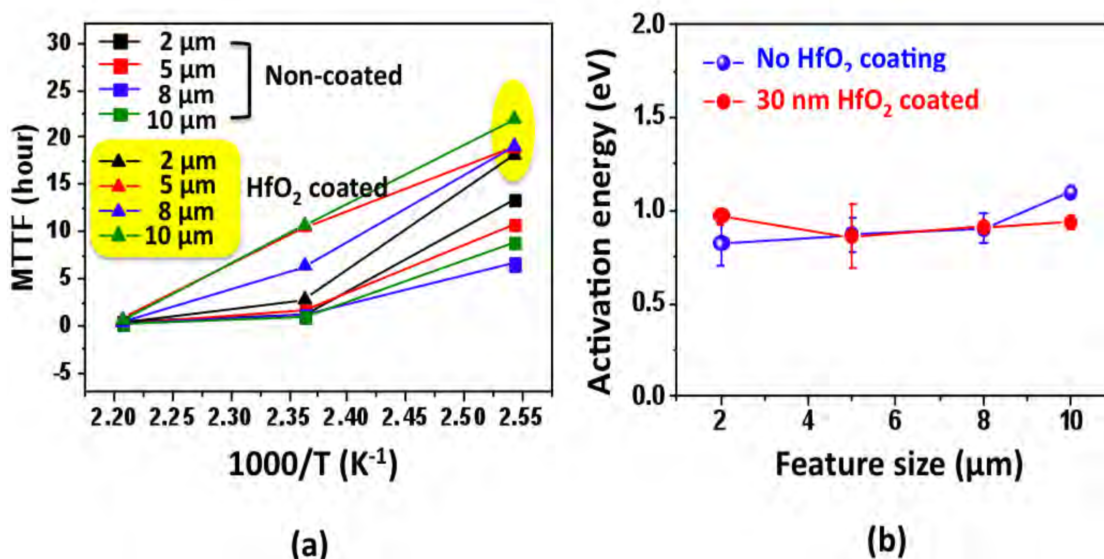

Figure 5.14. Comparisons of mean time to failure and activation energy between uncoated and HfO_2 coated 0.6 μm thick patterned PZT (52/48) thin films. (Calculated from the Weibull distribution function)

D. Microstructure after HALT Measurement

After HALT measurement, the electrode surfaces of capacitors were imaged by field emission scanning electron microscopy (FE-SEM) to assess the failure mechanism.

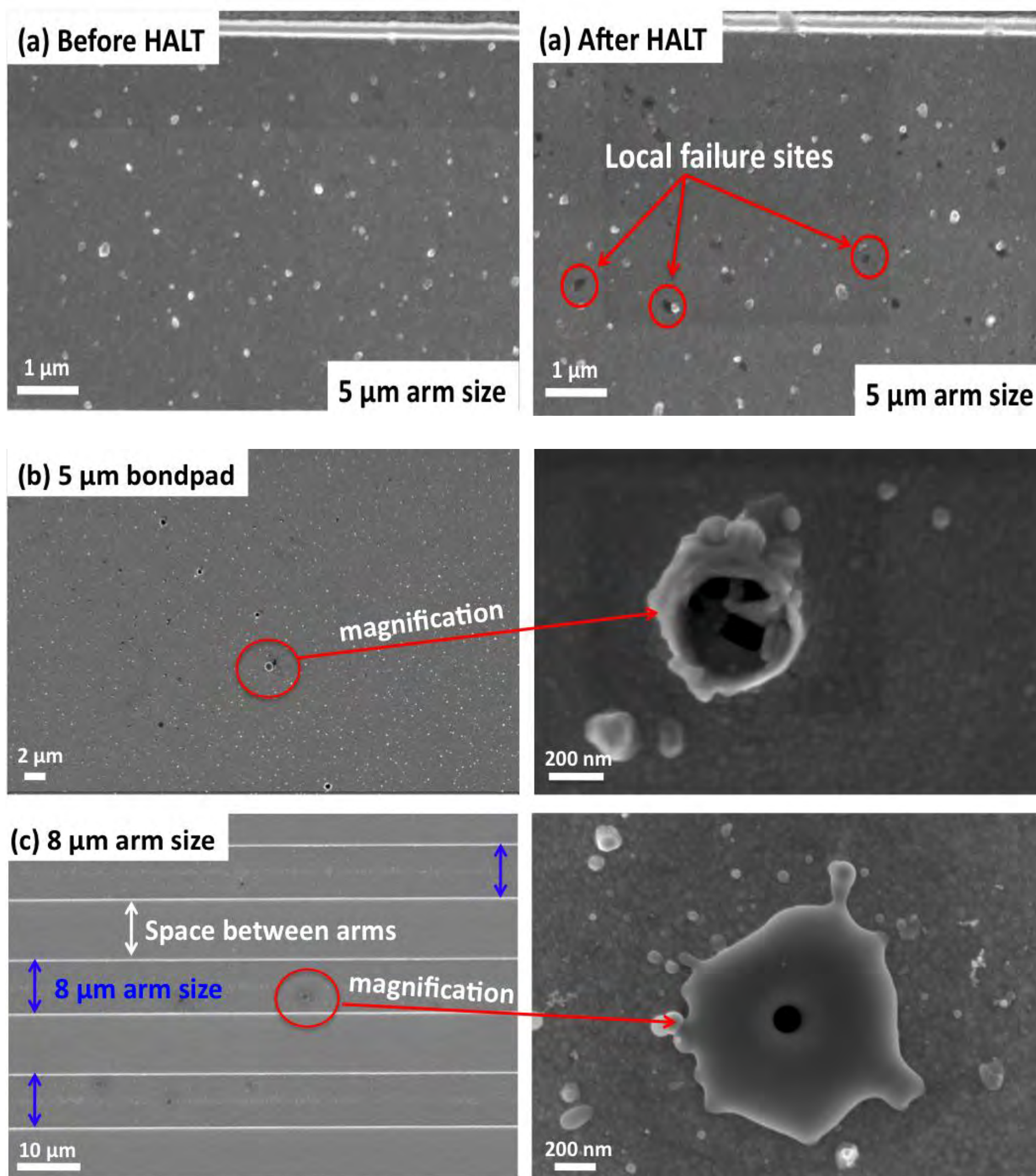

Figure 5.15. FE-SEM micrograph of surface of Pt/PZT/Pt layers after HALT measurements. (a) the comparison between before and after HALT testing; (b) and (c) are magnified blackened spots on a 5 µm bondpad and 8 µm arms respectively

As shown in Figure 5.15 (a), there are blackened defect sites on the surface of films following HALT testing. There is little evidence for microcracking as a major failure mechanism. The distribution of these local failure sites on a 5 μm bondpad and 8 μm feature size arm is shown in Figure 5.15 (b) and (c). Local failures are characterized by crater defects in which Pt/PZT layers have been eliminated; the resulting craters are distributed relatively evenly over the surface area. There is no evidence for a strong preference for failure near the etched sidewalls. It is also clear that multiple local breakdown events are associated with eventual degradation.

E. Determination of Voltage Acceleration Factor

The voltage acceleration factor was determined from the power-law dependence on voltage at fixed temperature [27].

$$\ln\frac{t_1}{t_2} = n\ln\frac{V_2}{V_1} \quad \text{or} \quad t = C_T V^{-n} \qquad \text{equation 5.10}$$

where V is the applied voltage, t is the median time to failure, C_T is a constant, and n is the voltage acceleration factor. Figure 5.16 illustrates ln median time to failure versus ln voltage.

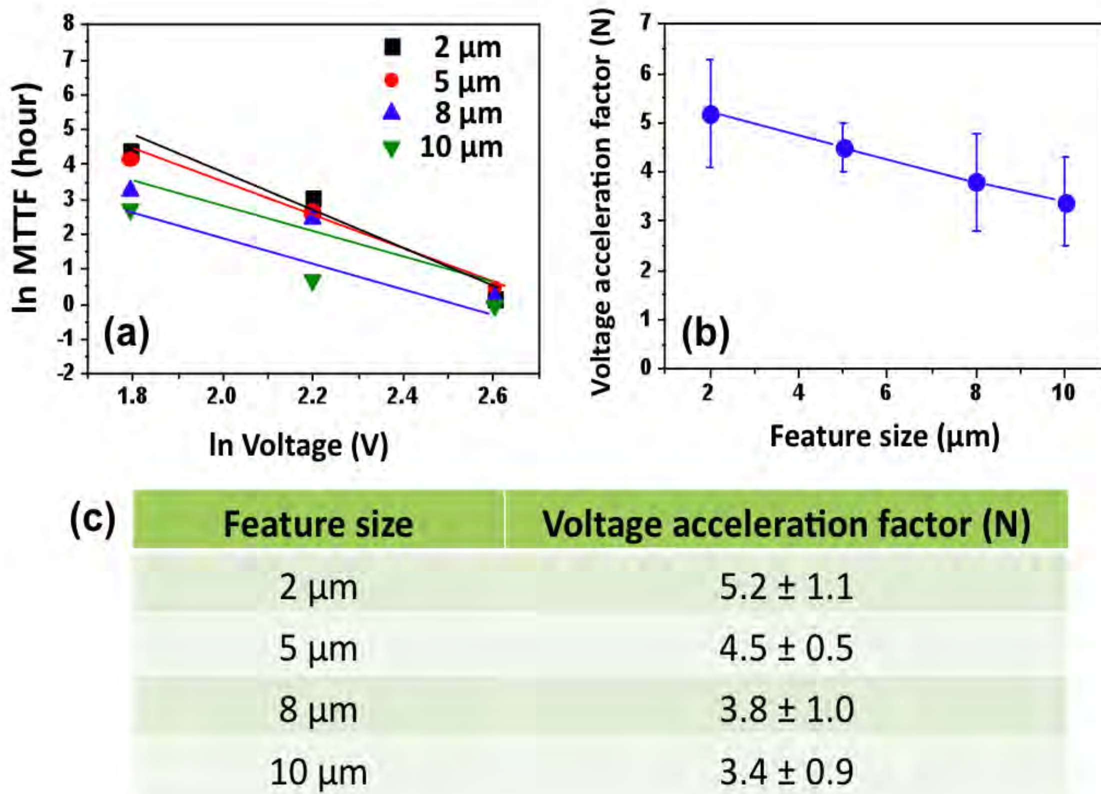

Feature size	Voltage acceleration factor (N)
2 µm	5.2 ± 1.1
5 µm	4.5 ± 0.5
8 µm	3.8 ± 1.0
10 µm	3.4 ± 0.9

Figure 5.16. Plots of (a) the ln mean time to failure, (b) and (c) the voltage acceleration factor of all feature sizes (data from measurements at 100 kV/cm, 150 kV/cm or 225 kV/cm at a temperature of 150 ^{o}C) to calculate the voltage acceleration factor from the slope of the line (Experimental data were taken from 0.6 µm thick patterned PZT (52/48) thin films without ALD HfO_2 coating)

The ranges of voltage acceleration factors (n) for all feature sizes are 3.4 ~ 5.2 in Figure 5.16 (b) and (c). It is clear that the voltage acceleration factor rises for smaller feature sizes. These calculated values are comparable to previous reports of n ~ 4-5 for PZT thin films.[(29)] Garten established a new model for the voltage acceleration factors based on the presumption

that Schottky barrier are important to the failure process of blanket films.[29] To assess whether this is important in patterned films, the voltage acceleration factor was refitted using Garten's model. The ranges of voltage acceleration factor (n) for all feature sizes are 2.2 ~ 3.4 as shown in Figure 5.17. A voltage acceleration factor of ~ 2 for the larger features sizes would be consistent with a Schottky model. However, the larger voltage acceleration factors for the finer feature sizes suggest that the sidewalls do, indeed, play an additional factor in influencing the MTTF.

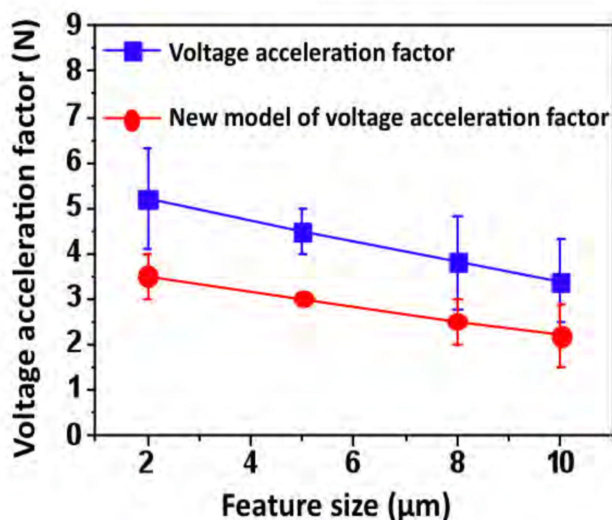

	2 µm	5 µm	8 µm	10 µm
Voltage acceleration factor	5.2 ± 1.1	4.5 ± 0.5	3.8 ± 1.0	3.4 ± 0.9
Voltage acceleration factor (new model)	3.5 ± 0.5	3.0 ± 0.1	2.5 ± 0.5	2.2 ± 0.7

Figure 5.17. The plot and table of comparisons of voltage acceleration factors obtained from the Eyring equation and Garten model (Experimental data were taken from 0.6 μm thick patterned PZT (52/48) thin films without ALD HfO_2 coating)

5.3.2. Conduction Mechanisms in 0.6 μm Thick Patterned PZT (52/48) Thin Film

An analytical study of the conduction mechanisms in current-voltage characteristics was undertaken to provide additional information on reliability. Several conduction mechanisms have been suggested in the literature: Schottky emission and Poole-Frenkel emission are often reported for PZT films. Leakage current versus voltage measurements were conducted at several temperatures to investigate the conduction mechanisms.

The conduction mechanisms are summarized in Table 5.12. [22][36]

Table 5.12. Lists of conduction mechanisms

Mechanism	*J* - *E* characteristics	
1. Schottky emission	$J_{Sch} = A^{*}T^{2}\exp\left[\frac{-q\left(\phi_{B}-\sqrt{qE_{a}/4\pi\varepsilon_{i}\varepsilon_{0}}\right)}{k_{B}T}\right]$	Schottky barrier was formed when contact is made between metal and ferroelectric material
2. Poole-Frenkel emission	$J_{FP} = BE\exp\left[\frac{-q\left(\phi_{t}-\sqrt{qE_{a}/\pi\varepsilon_{i}\varepsilon_{0}}\right)}{k_{B}T}\right]$	Governed by emitted transport carrier from trap centers under an application of strong electric field
3. Ohmic current	$J_{Oh} = q\mu_{p}n_{0}E\exp\left[\frac{-qE_{a}}{k_{B}T}\right]$	If an excess charge on the surface is placed enough to bend energy band structure for holes, the interfaces becomes an ohmic contact
4. Space Charge limited	$J_{SCL} = C\mu_{p}\varepsilon_{i}\frac{V^{2}}{d^{3}}\exp\left[\frac{-qW_{t}}{k_{B}T}\right]$	Governed by excess carriers within an insulator
5. Others	Tunneling current, Ionic Conduction, Intrinsic Conduction	

A. Schottky Emission

Typical energy diagrams for Schottky barriers are discussed in many textbooks to describe the situation when a metal and a n-type or p-type semiconductor are brought into contact. [37]

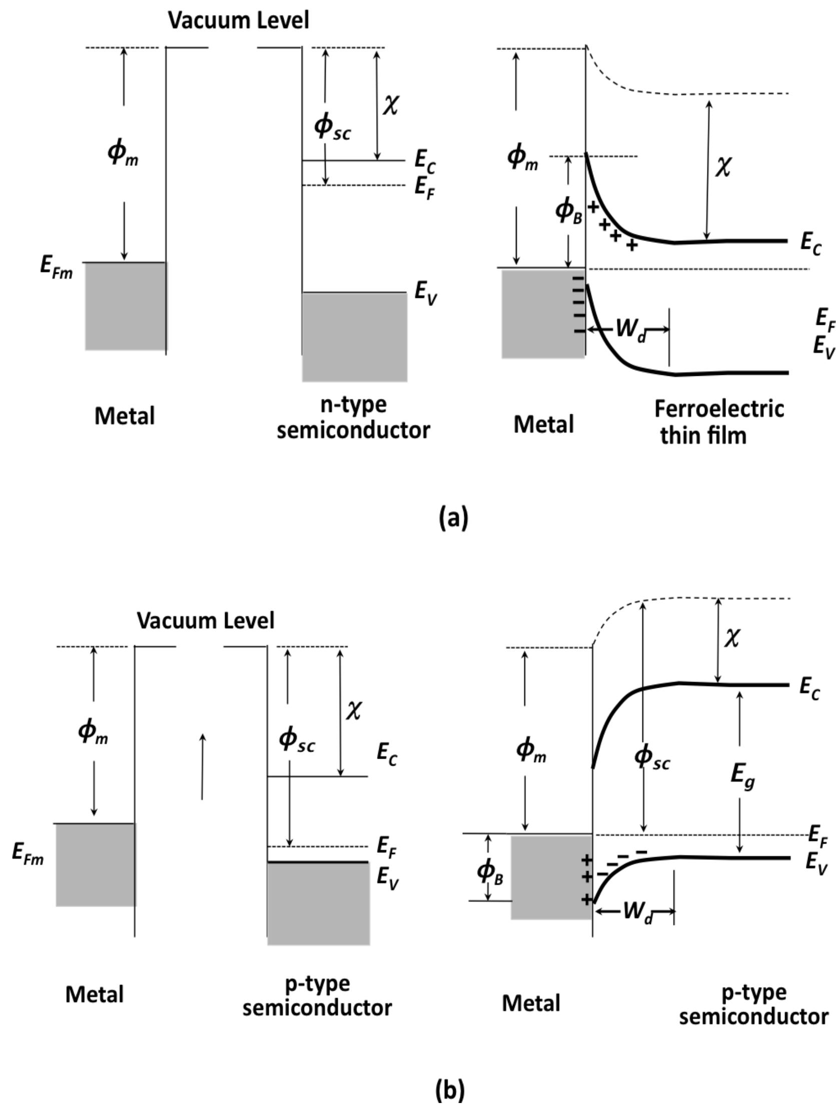

Figure 5.18. Schottky barrier energy band diagrams of (a) metal-n type semiconductor contact with $\phi_m > \phi_{sc}$ and (b) metal- p type semiconductor contact with $\phi_m < \phi_{sc}$. The metal and semiconductor work functions are ϕ_m and ϕ_{sc}, respectively, while the Fermi energy is E_F and the Schottky barrier height is ϕ_B. (modified from reference [37])

In the case of contact between a metal and and n-type semiconductor with ϕ_m (metal work function) > ϕ_{sc} (semiconductor work function) as shown in Figure 5.18 (a), electrons flow from the semiconductor into the metal; the result is band bending and generation of an electrical potential near the interface. When the chemical potential in the n-type semiconductor reaches equilibrium with the Fermi energy in the metal, a region depleted of electrons is produced, called the depletion layer (W_d) or space charge region. Figure 5.18 (b) shows the case when contact is made between a metal and a p type semiconductor having $\phi_m < \phi_{sc}$. Electrons flows from the metal into the semiconductor until the Fermi energy is the same in both. Again, a depletion layer is formed in the p-type semiconductor.

From the standpoint of defect chemistry, there is controversy in the literature as to whether undoped PZT films are p-type or n-type semiconductors.[37] Bulk PZT is widely acknowledged to be p-type.[10][38] In this chapter, it is assumed that undoped PZT is p-type due to PbO volatilization during crystallization. The origin of p-type conduction in PZT can be described via the following reactions:

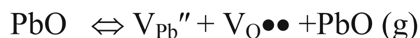

$$PbO \Leftrightarrow V_{Pb}'' + V_O^{\bullet\bullet} + PbO\ (g)$$

The oxidation reaction can be described as

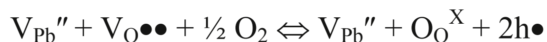

$$V_{Pb}'' + V_O^{\bullet\bullet} + \tfrac{1}{2} O_2 \Leftrightarrow V_{Pb}'' + O_O^X + 2h^\bullet$$

However, from the results of the experimental observation on the leakage current behavior, it is difficult to conclude whether the PZT thin film is p-type or n-type. Electrodes with large work functions like Pt produce large Schottky barriers, which is not expected for a p-type dielectric film. Scott et al., proposed that this could be explained if the majority of the PZT

film was p-type, but that near the Pt electrodes, n-type inversion regions exist.[39] That is, conduction in PZT films is more complicated than the ideal case of a thin film capacitor with ideal electrodes and no surface states. In particular, diffusion of lead into the electrodes (e.g. the bottom electrode) and traps at the surfaces should be considered because these factors change the surface charge density near the interface, which can influence the Schottky barrier heights.

The leakage current (J_{sch}) for a Schottky emission is governed by equation 5.11.

$$J_{sch} = A^* T^2 \exp\left[\frac{-q(\phi_{Bp} - \sqrt{\frac{qE_a}{4\pi\varepsilon_i\varepsilon_0}}}{k_B T}\right] \qquad \text{equation (5.11)}$$

where A* is the modified Richardson's constant, Φ_{Bp} the potential height, T the absolute temperature, E the applied electric field, ε_i the dynamic dielectric constant in ferroelectric material, q unit charge and k_B Boltzmann's constant.

B. Poole - Frenkel Emission (PF emission)

The dominant mechanism of Poole-Frenkel emission model is transport of carriers released from trapped centers by application of an electric field. The carriers jump from trap to trap. Figure 5.19 illustrates the Poole-Frenkel emission mechanism. [22][33]

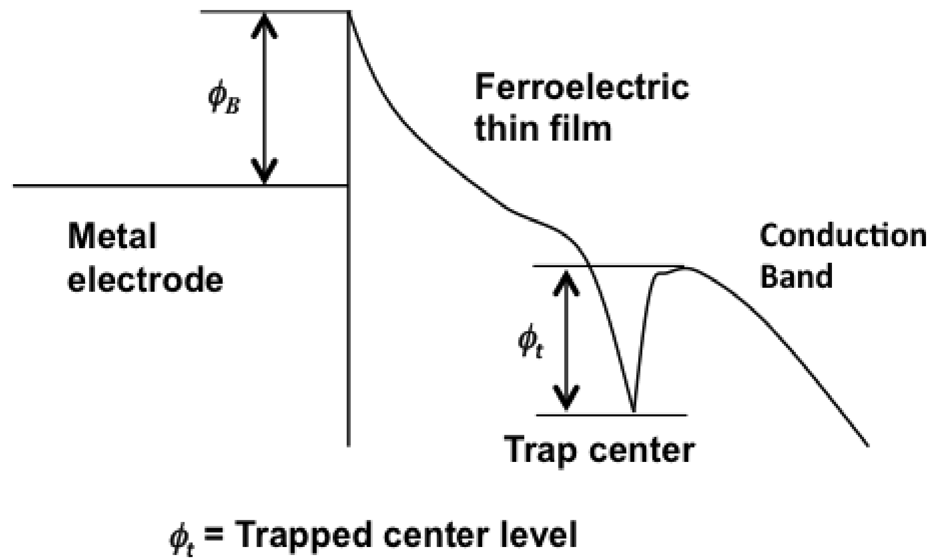

Figure 5.19. The schematic diagram of the Poole-Frenkel emission

The Poole-Frenkel leakage current is described as

$$J_{FP} = BE\exp\left[\frac{-q(\phi_i - \sqrt{\frac{qE}{\pi\varepsilon_i\varepsilon_0}})}{k_B T}\right]$$ equation (5.12)

where B is a constant and ϕ_i is the trap center level.

The current-voltage (I-V) characteristics of 0.6 μm patterned PZT (52/48) was investigated at several temperatures. Figure 5.20 shows the I-V curve of different lateral feature sizes at room temperature. The applied electric field was gradually increased up to 833 kV/cm; positive bias was applied on the top electrode with respect to the bottom electrode. As shown in Figure 5.20, the breakdown strength increases with the size of the lateral features.

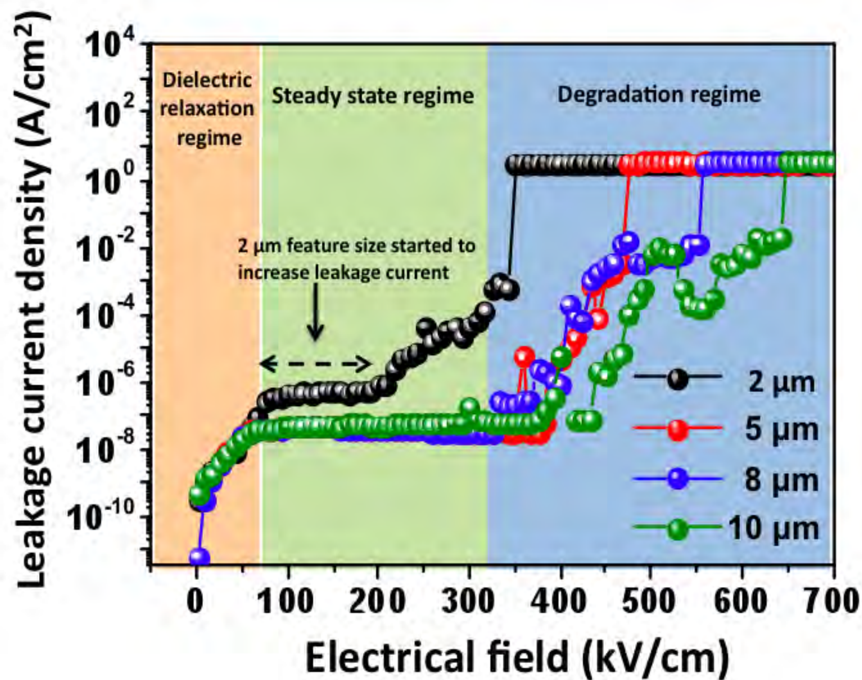

Figure 5.20. I-V characteristics of 0.6 μm patterned PZT (52/48) measured from 0 V to 50 V at room temperature

I-V measurements were conducted as a function of temperature from 50 ^{o}C to 150 ^{o}C. To investigate possible conduction mechanisms, the dynamic dielectric constant was derived from the slope of Schottky and Poole-Frenkel plots (Figure 5.21 and 5.22). It is observed that the field-dependence of the current fitted both the Schottky and Poole-Frenkel emission models very well in the high-field region. The dynamic dielectric constant was extracted from the Schottky emission and Poole-Frenkel models. The dynamic dielectric constant is identical to the square of the refractive index ($n = \sqrt{\varepsilon}$).

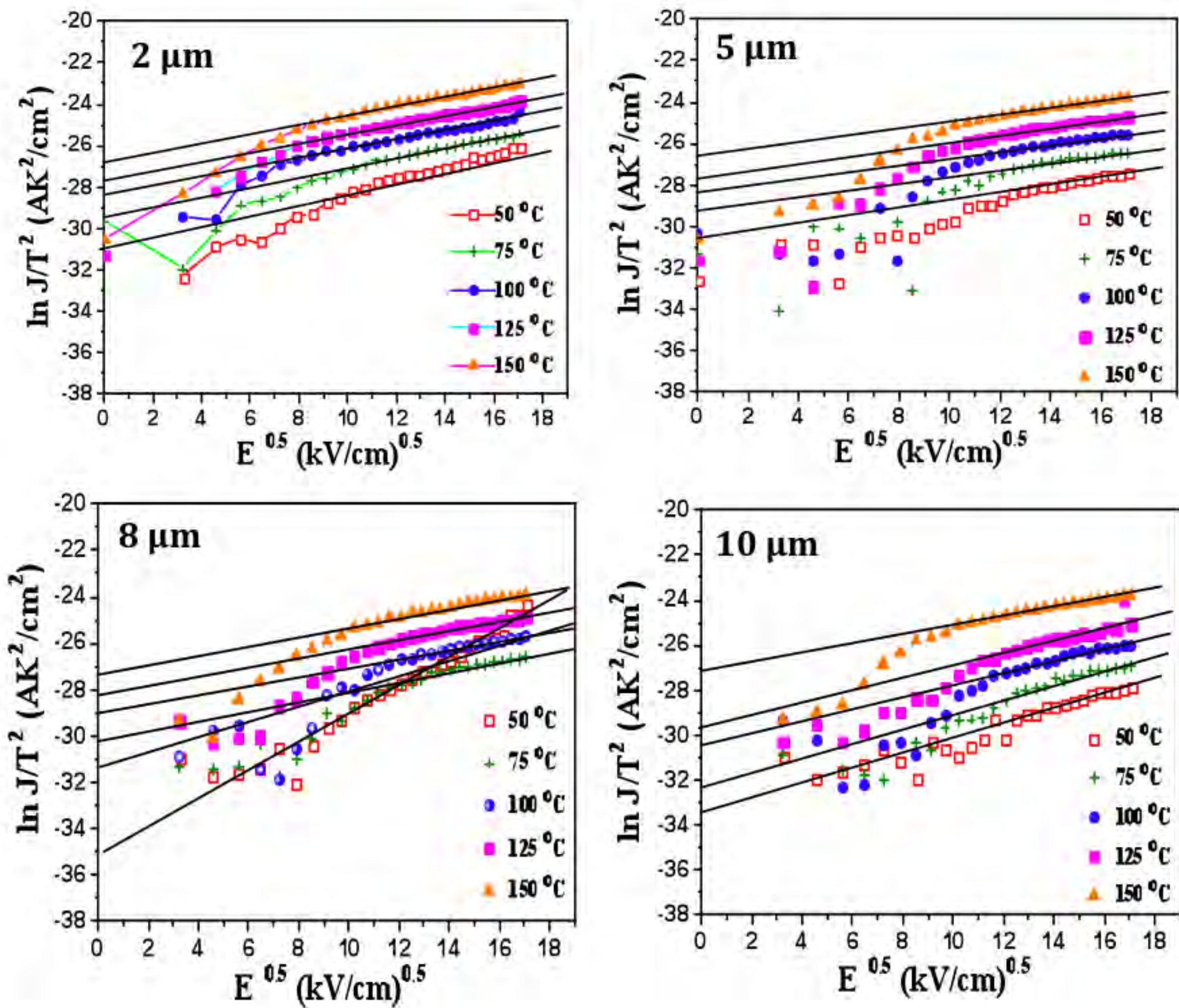

Figure 5.21. ln (J/T^2) versus E $^{0.5}$ as function of temperature for 0.6 μm thick patterned PZT films with different lateral feature sizes (The current is fitted well with Schottky emission model at high electrical fields)

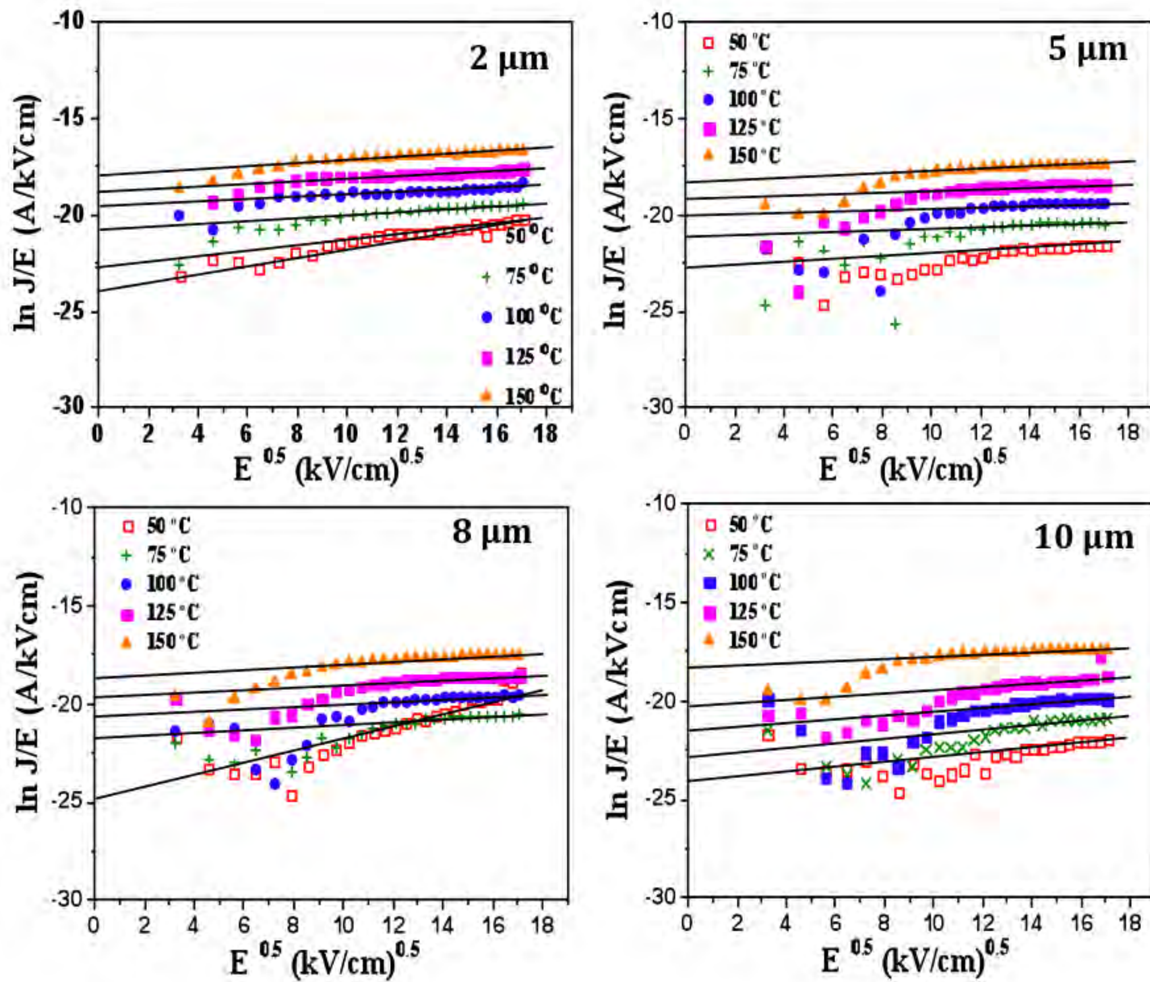

Figure 5.22. ln (J/E) versus E $^{0.5}$ as function of temperature of 0.6 μm patterned PZT film (The current is fitted well with Poole-Frenkel emission model at high electrical fields)

The range of derived refractive index from Schottky and Poole-Frenkel model are from 1.7 to 2.4 and from 5.9 to 20, respectively, for all feature sizes as shown in Table 5.13 and Figure 5.23. The experimental refractive index in PZT is from 2.1 to 2.5.[(43)(44)] Thus, it was concluded that the Schottky emission model is more reasonable.

Table 5.13. The refractive index as a function of temperature extracted from Schottky and Poole-Frenkel emission models

Schottky	50°C	75°C	100°C	125°C	150°C
2 µm	1.9	1.6	3.1	1.8	2.3
5 µm	2.5	2.1	2.4	2.3	2.0
8 µm	2.4	2.2	1.8	2.0	1.7
10 µm	1.9	2.0	2.0	1.8	1.9

Frenkel Poole	50°C	75°C	100°C	125°C	150°C
2 µm	5.9	9.8	8.2	12.4	10.7
5 µm	13.3	13.3	18	14.4	11.5
8 µm	14.7	19.4	16.8	17	19
10 µm	13.9	17.3	18.5	19.4	17.8

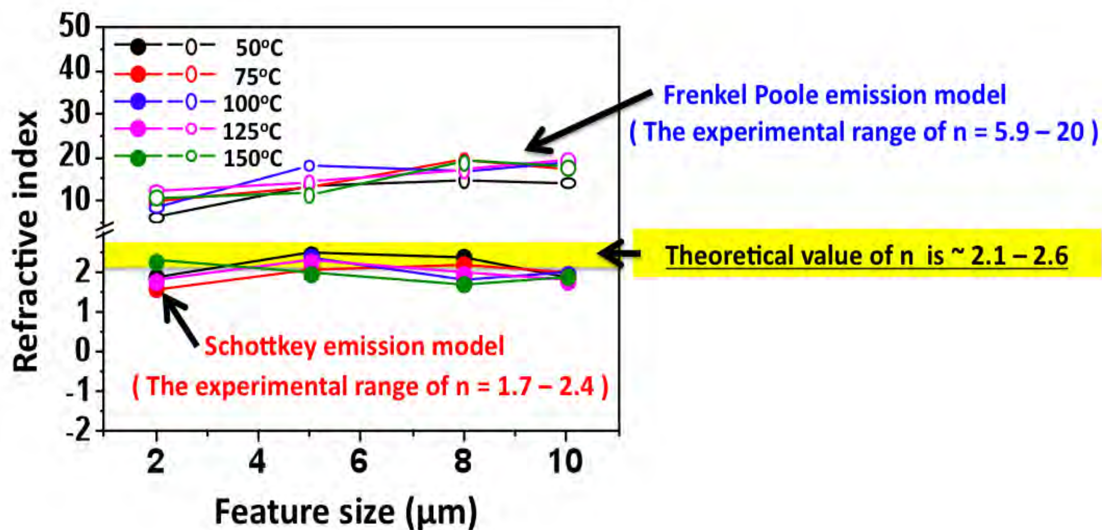

Figure 5.23. Plots of the experimental refractive index as a function of temperature extracted from Schottky and Pool-Frenkel emission models

The Schottky barrier height (ϕ_{Bp}) was extracted from plots of ln (J/T^2) versus 1/T when E=0 using the Schottky emission model as shown in Figure 5.23. [42][45][46][47][48] The range of Schottky barrier heights is from 0.4 to 0.56 eV. The value of Schottky barrier height slightly increased with increasing feature size.

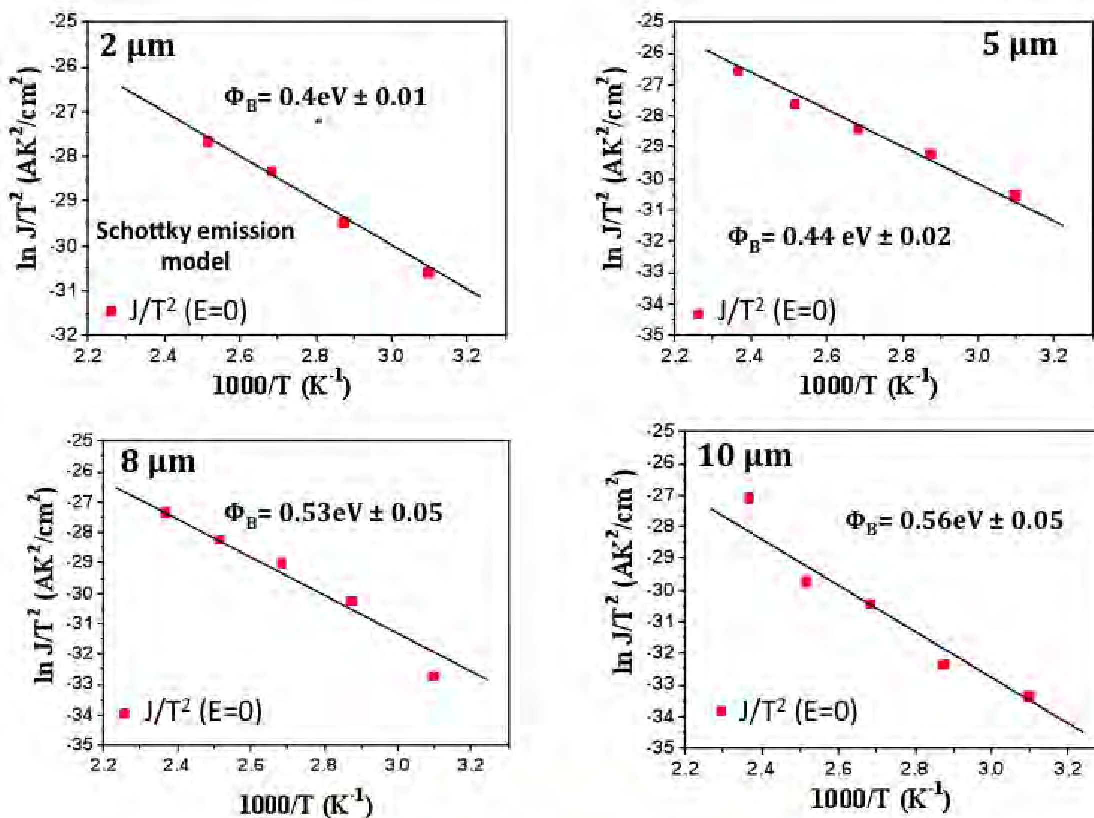

Schottky Barrier Heights (Φ_B)

	2 µm	5 µm	8 µm	10 µm
Φ_{Bp}	0.4± 0.01	0.44± 0.02	0.53± 0.05	0.56± 0.05

Figure 5.24. Evaluation of the barrier height for the Schottky emission model. In the table, values of barrier heights for all feature size are listed

It is possible that the 2 μm feature size has more defects from the sidewall induced during etching; these factors might lower the Schottky barrier heights.

5.4. Conclusions

In this chapter, HALT measurements were conducted to assess the lifetime of patterned PZT films and to determine the failure mechanism. Also, I-V measurements were performed to study the possible conduction mechanism as a function of temperature.

Based on Weibull analysis, the lifetime (characteristic time to failure t_{50}) of patterned PZT films increased with decreasing feature size as a function of temperature and voltage. The ranges of activation energy for all feature sizes were 0.82 eV ~ 1.1 eV.

It was hypothesized that there are two potential failure paths associated with patterned features: the sidewall and the bulk of the film. Trapping/detrapping of carriers at the sidewall appeared to lengthen the lifetime in patterned PZT (52/48) films for smaller feature sizes. The 2 μm feature size presumably has more sidewall damage and induced dangling bonds that may act as trap centers, since it has a longer perimeter. As a result, there could be more unfilled trap sites for the 2 μm feature size parts compared to the 10 μm feature size. Therefore, the breakdown in the 2 μm feature size will occur at a higher failure time. The activation energy for failure of the 2 μm feature sizes was the smallest value observed (~0.82 eV), possibly because the trap centers are distributed more broadly in energy.

A second failure pathway can occur through the "bulk" of the ferroelectric. 10 μm arm size has a more chance to have shorter failure time due to trapped charge carriers such as electron, hole and oxygen vacancies at a higher density of domain walls acting as conduction pathway. The activation energy for failure might then be correlated with the activation energy for

motion of the carriers. Since the activation energy (~ 1 eV) is higher than that reported for oxygen vacancy migration (~0.6 eV), it is possible that detrapping of carriers from domain walls dominates the response. It should also be noted that the process of patterning the ferroelectric material apparently changes the likelihood of failure in the bulk of the film.

HfO_2 was coated on PZT film to reduce sidewall damage using ALD. After ALD coating, the lifetime of all features sizes improves. In addition, activation energies are very similar for all feature sizes. These results suggest that after ALD coating, the sidewall damage is partially recovered, so the effect of sidewall damage on the breakdown mechanism is reduced.

After HALT measurement, the electrode surfaces of capacitors were imaged by field emission scanning electron microscopy (FE-SEM) to observe visible change on the surface of PZT (52/48) thin film. It was observed that there were blackened defect sites on the surface of films after HALT testing. Blackened regions looked like explosion sites. The breakdown events appear all over the surface area, and are not concentrated at the sidewalls. The electric field is enhanced near defects so local breakdown events occurred and multiple local breakdown events precede eventual degradation.

I-V measurements were performed as function of temperature to investigate possible conduction mechanisms. From the I-V results, the refractive index was calculated from Schottky and Poole-Frenkel plots. A refractive index of about 1.7 to 2.5 was obtained from the Schottky emission model; this value is in good agreement with the range of known refractive index in PZT material is from 2.1 to 2.5. The value of refractive index obtained from the Poole-Frenkel model does not fit the experimental value. Therefore, it seems likely that the correct conduction mechanism is Schottky conduction in patterned PZT film at intermediate field levels. Also, it was calculated that the range of Schottky barrier heights with different feature size was from 0.4

to 0.56 eV; it was also found that the value of Schottky barrier height slightly increased with increasing feature size. The reason for this is unknown, but it is possible that the 2 μm feature size may have more defects from the sidewall induced by etching; these factors might lower the Schottky barrier heights.

5.5. References

1. P. Muralt, R.G. Polcawich, and S. Trolier-McKinstry, “Piezoelectric thin films for sensors, actuators, and energy harvesting,” MRS Bulletin Vol. 34, 658-664 (2009)

2. D. Dimos, R. W. Schwartz and S. J. Lockwood, “Control of leakage resistance in Pb(Zr, Ti)O_3 thin films by donor doping,” J. Am. Ceram, Soc. Vol. 77 [11], pp. 3000-3005 (1994)

3. J.F. Scott and C.A. Paz de Araujo, “Ferroelectric memories,” Science Vol. 246, No.4936, pp. 1400-1405 (1989)

4. A.J. Moulson and J.M. Herbert, Electroceramics, Chapman & Hill New York, (1990)

5. K. Lehovec and G.A. Shim, “Conductivity injection and extraction in polycrystalline barium titanate,” J. Appl. Phys., Vol. 33, pp. 2036-2044 (1962)

6. Rainer Waser, Tudor Baiatu, and Karl-Heinz Hardtl, “dc electrical degradation of perovskite-type titanates: I, ceramics,” J. Am. Ceram. Soc., Vol. 73, No. 6, pp. 1645-53 (1990)

7. Rainer Waser, Tudor Baiatu, and Karl-Heinz Hardtl, “dc electrical degradation of perovskite-type titanates: II, single crystals,” J. Am. Ceram. Soc., Vol. 73, No. 6, pp. 1654-62 (1990)

8. Markus Vollman and Rainer Waser, "Grain boundary defect chemistry of acceptor-doped titanates: space charge layer width," J. Am. Ceram. Soc., Vol. 77, No. 1, pp. 235-43 (1994)

9. R. Waser, "Processing of Dielectric Titanates: Aspects of Degradation and Reliability," in Ferroelectric Ceramics, Tutorial review, theory processing, and applications, edited by N. Setter and E. L Colla, pp. 273-298, published by Birkhausere Verlag, (1993)

10. Ken Numata, Yukio Fukuda, Katsuhiro Aoki and Kitoshi Nishimura, "Analysis of resistance degradation of $SrTiO_3$ and $Ba_xSr_{(1-x)}TiO_3$ thin films," Jpn. J. Appl. Phys. Vol. 34, Part 1, No. 9B, pp. 5245-5249 (1995)

11. Husam N. Al-Shareef and Duane Dimos, "Leakage and reliability characteristics of lead ziconate titanate thin-film capacitors," J. Am. Ceram. Soc., Vol. 80, No. 12, pp. 3127-32 (1997)

12. S. Zhao, S. J. Zhang, W. Liu, N. J. Donnelly, Z. Xu, and C. A. Randall, "Time dependent dc resistance degradation in lead-based perovskites: 0.7 $Pb(Mg_{1/3}Nb_{2/3})O_3$-0.3 $PbTiO_3$," J. Appl. Phys., Vol. 105, pp. 053705-1-7 (2009)

13. Duane Dimos, Robert W. Schwartz, and Steven J. Lockwood, "Control of leakage Resistance in Pb(Zr, Ti)O_3 thin films by donor doping," J. Am. Ceram. Soc., Vol. 77, No. 11, pp. 3000-3005 (1994)

14. E. Bouyssou, R. Jerisian, N. Cezac, P. Leduc, G. Guegan, C. Anceau, "Wafer level reliability and leakage current modeling of PZT capacitors," Mat. Sci. & Eng. B 118, pp. 28-33 (2005)

15. J. J. Dih and R. M. Fulrath, "Electrical conductivity in lead zirconate-titanate ceramics," J. Am. Ceram. Soc. Vol. 61, No. 9-10, pp. 448-451 (1978)

16. M.V. Raymond and D.M. Smyth, "Defects and charge transport in perovskite ferroelectrics," J. Phys. Chem. Solids, Vol. 10, pp. 1507-1511 (1996)

17. H. Daniel Chen, K. R. Udayakumar, Kewen K. Li, Christopher J. Gaskey, & L. Eric Cross, "Dielectric breakdown strength in sol-gel derived PZT thick films," Integrated Ferroelectrics, Vol. 15, pp. 89-98 (1997)

18. J. Robertson, W. L. Warren, B. A. Tuttle, and D. Dimos, "Shallow Pb^{3+} hole traps in lead zirconate titanate ferroelectrics," Appl. Phys. Lett, Vol. 63, No. 11, pp. 1519-1521 (1993)

19. B.S. Kang, S. K. Choi and C. H. Park, “Diffuse dielectric anomaly in perovskite-type ferroelectric oxides in the temperature range of 400–700°C,” J. Appl. Phys., Vol. 94, No. 3, pp. 1904-1911 (2003)

20. William J. Minford, “Accelerated life testing and reliability of high k multilayer ceramic capacitors,” IEEE Transaction on Components, Hybrids and Manufacturing Technology, Vol. CHMT-5, No. 3, September (1982)

21. T. I. Prokopowicz and A. R. Vaskas, “Research and development, intrinsic reliability, subminiature ceramic capacitors,” Final Rep. ECOM-90705-F, NTlS AD-864068, Oct. (1969)

22. Takashi Mihara and Hitoshi Watanabe, “Electric conduction characteristics of sol-gel ferroelectric $Pb(Zr_{0.4}Ti_{0.6})O_3$ thin-film capacitors: Part I,” Jpn. J. Appl. Phys. Vol. 34, pp. 5664-5673 (1995)

23. Stewart K. Kurtz, Solomon Levinson, and Dexiang Shi, “Infant mortality, freaks, and wear-out: Application of modern semiconductor reliability methods to ceramic multilayer capacitors,” J. Am. Ceram. Soc., Vol. 72, No. 12, pp. 2223-33 (1989)

24. Beihai Ma, Manoj Narayanan and U. Balachandran, “Dielectric strength and reliability of ferroelectric PLZT films deposited on nickel substrates,” Materials Letters 63, pp 1353-56 (2009)

25. Waloddi Weibull and Stochholm Sweden, “A statistical distribution function of wide applicability,” J. of Appl. Mechanics, pp. 293-297, September (1951)

26. Jung-Hyuk Koh and Tae-geun Kim, “Reliability of Pb(Mg, Nb)O_3-Pb(Zr, Ti)O_3 multilayer ceramic piezoelectric actuators by Weibull method,” Microelectronics Reliability, 46, pp183-188 (2006)

27. Ronald G. Polcawich and Susan Trolier-McKinstry, “Piezoelectric and dielectric reliability of lead zirconate titanate thin films,” J. Mater. Res., Vol. 15, No. 11, pp. 2505-2513 (2000)

28. Ronald G. Polcawich, "Piezoelectric and Dielectric Reliability in Lead Zirconate Titanate Thin Films,” Masters thesis in Materials Science and Engineering, the Pennsylvania State University (1999)

29. Lauren M. Garten, “Reisdual Ferroelectricity, Piezoelectricitiy, and Flexoelectricity in Barium Strontium Titannate Tunable Dielectrics,” PhD thesis in Materials Science and Engineering, the Pennsylvania State University (2014)

30. A. Misarova, “Aging of barium titanate single crystal,” Sov. Phys. Solid State (Engl. Transl.), 2, 1160 (1960)

31. K. Carl and K. H. Hardtl, "Electrical after effects in Pb(Ti,Zr)O_3 ceramics," Ferroelectrics, Vol. 17, 47 (1978)

32. W. L. Warren, Duane Dimos, and B. A. Tuttle, "Electronic and ionic trapping at domain walls in $BaTiO_3$," J. Am. Ceram. Soc. Vol. 77 [10], pp. 2753-2757 (1994)

33. E. Hong, R. Smith, S.V. Krishnaswamy, C.B. Freidhoff, and S. Trolier-McKinstry, "Residual stress development in Pb(Zr,Ti)O_3/ZrO_2/SiO_2 stacks for piezoelectric microactuators," Thin Solid Films, Vol. 510, Issue 1-2, pp. 213-221 (2006)

34. Jae-Wung Lee, Chee-Sung Park, Miyoung Kim, and Hyoun-Ee Kim, "Effects of residual stress on the electrical properties of PZT films," J. Am. Ceram. Soc., 90 [4], pp.1077–1080 (2007)

35. Geoff L. Brennecka, Wayne Huebner, Bruce A. Tuttle and Paul G. Clem, "Use of stress to produce highly oriented tetragonal lead zirconate titanate (PZT 40/60) thin films and resulting electrical properties," *J. Am. Ceram. Soc.,* 87 [8], pp.1459–1465 (2004)

36. Roni D. Levi, "Solid solution trends that impact electrical design of submicron layers in dielectric capacitors," PhD thesis in Materials Science and Engineering, the Pennsylvania State University (2009)

37. M.S. Tyagi, “Introduction to semiconductor materials and devices,” Chapter 10. Majority carrier diodes, pp. 263-291, published by John Wiley & Sons, Inc. (1991)

38. Carlos Paz de Araujo, James F. Scott, George W. Taylor, “Ferroelectric thin films: synthesis and basis properties,” in Ferroelectricity and Related Phenomena, vol 10, Intergrated Ferroelectric Devices and Technologies, part 1, published by Gordon and Breach (1996)

39. S.M. Sze: Physics of Semiconductor Devices (John Wiley & Sons., New York, 1981) 2nd ed.

40. D. M. Smyth, ‘‘The Role of Impurities in Insulating Transition Metal Oxides,’’ *Prog. Solid State Chem.,* **15**, pp.145–71 (1984)

41. J.F. Scott, “Device physics of ferroelectric thin-film memories,” Jpn. J. Appl. Phys. Vol. 38, Part 1, No. 4B, pp. 2272-2274 (1999)

42. C.A. Mead, “Metal-Semiconductor Surface Barriers,” in Solid-State Electronics, Pergamon Press, Vol. 9, pp. 1023-1033 (1965)

43. Philip D. Thacher, “Refractive index and surface layers of ceramic (Pb, La)(Zr, Ti)O_3 compounds,” Applied Optics, vol. 16, no. 12, pp.3210-3213 (1977)

44. Akira Okada, "Some electrical and optical properties of ferroelectric lead- zirconate–lead- titanate thin films," Journal of Applied Physics, Vol. 48, No.7, pp. 2905-2909 (1977)

45. Y.S. Yang, S.J. Lee, S.H. Kim, B.G. Chae, and M.S. Jang, "Schottky barrier effects in the electronic conduction of sol-gel derived lead zirconate titanate thin film capacitors," J. Appl. Phys. Vol. 84, No. 9, pp. 5005-5011 (1998)

46. B. Nagaraj, S. Aggarwal, T. K. Song, T. Sawhney, and R. Ramesh, "Leakage current mechanism in lead-based thin-film ferroelectric capacitors," Phys. Rev. B, Vol. 59, No. 24, pp. 16 022-027 (1999)

47. Ju Cheol Shin, Cheol Seong Hwang, and Hyeong Joon Kim, "Leakage current of sol-gel derived $Pb(Zr, Ti)O_3$ thin films having Pt electrodes," Applied Physics Letters, Vol. 75, No. 21, pp. 3411-13 (1999)

48. Feng Chen and Andreas Klein, "Polarization dependence of Schottky barrier heights at interfaces of ferroelectrics determined by photoelectron spectroscopy," Physical Review B, Vol. 86, 094105 (2012)

Chapter 6

Aging Behavior in Patterned PZT (52/48) Thin Films

Long-term reliability of microelectronic devices will be essential to adoption of piezoelectric MEMS by industry. In particular, ferroelectric materials are prone to degradation processes such as aging. This chapter briefly describes the mechanisms of aging reported in the literature and discusses experimental results on aging in patterned PZT thin films with different lateral feature sizes. Of particular interest is whether the process of laterally patterning films by reactive ion etching introduces defects that change the mechanism or rate of property aging.

6.1. Introduction

Aging is the gradual change of physical and electrical properties with time in the absence of an external mechanical and electrical load on the material.(1)(2)(3)(4)(5) Dielectric aging can be manifested in ferroelectric materials from changes in the polarization-electric field (P-E) hysteresis loop, as shown in Figure 6.1, where aged materials can develop pinching of the hysteresis loop. (6)(7)(8) Also, properties such as the dielectric constant and piezoelectric parameters gradually decrease with time as shown in Figure 6.2. The change in a property often has a logarithmic relation: (9)

$$\frac{[Y(t) - Y(t_0)]}{Y(t_0)} = A * \log\left(\frac{t}{t_0}\right)$$

equation (6.1)

where Y(t) is the property at time t, $Y(t_0)$ is the initial property magnitude, and A is a constant. In ferroelectric materials, the dielectric and piezoelectric coefficients typically decrease by a few percent per decade, whereas the frequency constants increase with time, in response to time dependent changes in the domain structure. Aged materials can be deaged by application of high electric field or heating materials above their Curie temperature.(1)(3)(6) These processes re-write the domain structure and restart aging.

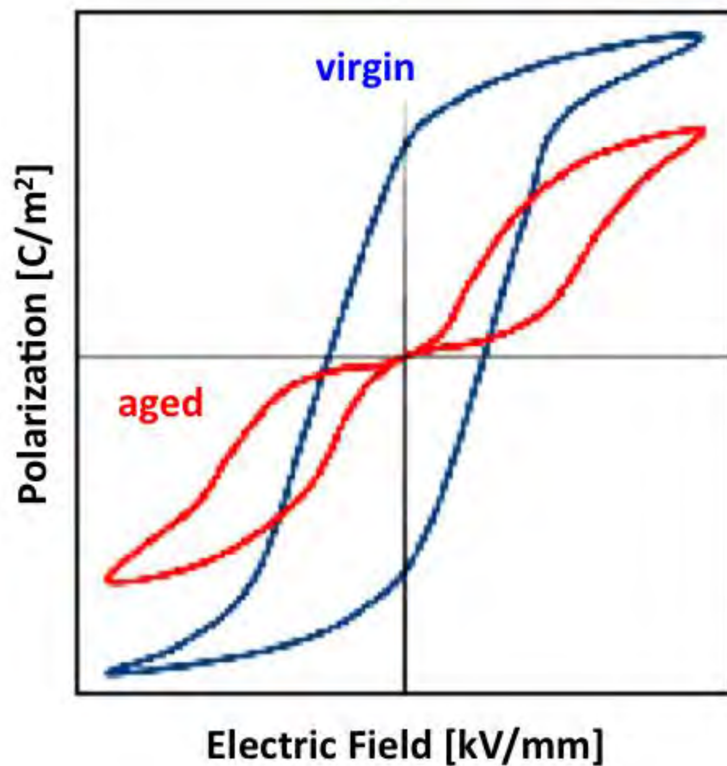

Figure 6.1. Schematic diagram of the polarization-electric field (P-E) hysteresis loop showing strongly pinched curve on aging [1]

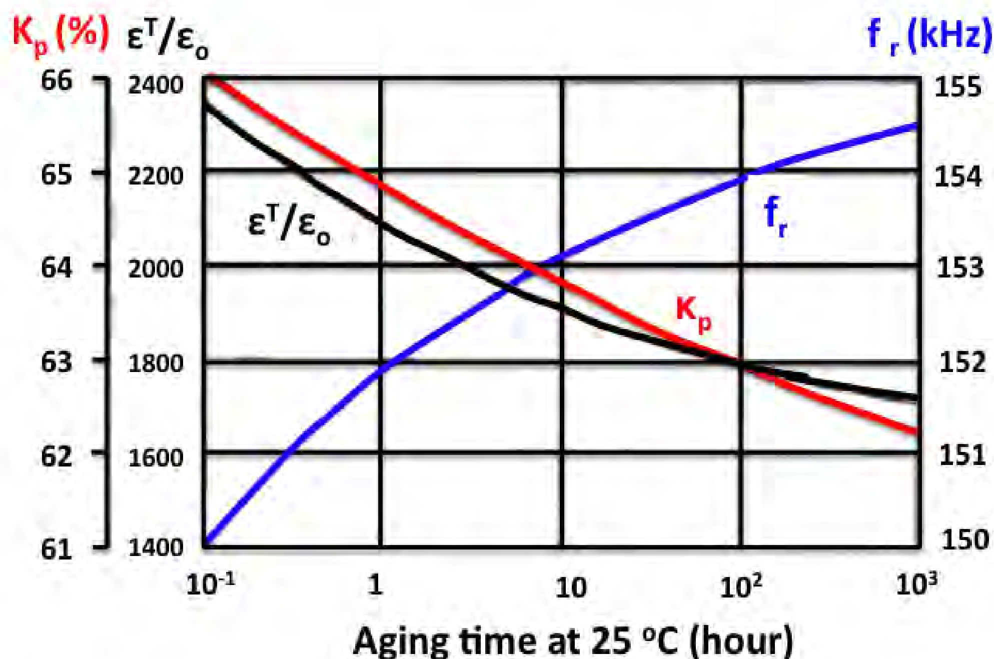

Figure 6.2. Aging of the dielectric, piezoelectric coupling factor and resonance frequency constant of poled PZT (modified from [2])

A number of researchers have reported aging rates and proposed aging mechanisms that are related to the stabilization of domain structure and immobilization of domain walls. Reported permittivity aging values are summarized in Table 6.1. The reported permittivity aging rates are measured at room temperature and 1 kHz. All aging rates are expressed percent decrease per decade.

Table. 6.1. Reported permittivity aging rate for PZT

Reference	Material	Composition / parameters	Aging rate (%/decade)	Comments
Zhong [10]	Undoped PZT(51/49) ceramic	0.02 mol% Ce	1.2	Combined doping of PZT ceramic with Ce-Mn shows reduced aging rates due to internal bias field
		0.5 mol% Mn	0.7	
		0.02 mol% Ce and 0.5 mol% Mn	0.3	
Srilomsak *et al.*[11]	Undoped PZT(53/47) ceramic	Undoped	5.9	Used harmonic analysis to investigate aging behavior
		1 mol% Mn	4.0	
		6 mol% Sr	3.2	
		2.4 mol% Nb	0.7	
Dederichs *et al.*[12]	$Pb(Ti_{0.42}Zr_{0.58})_{1-x}Fe_xO_3$ ceramic x=0.003	0.01 kHz	13.1	
		0.4 kHz	15.8	
		10 kHz	16.0	
Polcawich *et al.* [13]	PZT (52/48) thin film	Normal poling	2.4	UV imprint reduced aging rate due to the generation of the space charge field
		Thermal poling	2.4	
		UV	0.9	

As mentioned earlier, aging phenomena are caused by changes in the domain structure due to interaction with local elastic or electric fields in the material, or due to migration of mobile charge carriers. Aging processes can be represented by three mechanisms, which are strongly related to stabilization of the domain structure.

A. Volume Effect (Bulk Effect)

The volume effect is an alignment of defect dipoles, typically those formed by an oxygen vacancy and an acceptor ion (e.g., $Fe'_{Ti} - V_O^{\bullet\bullet}$; using Kroger-Vink notation), as shown in Figure 6.3 (a) and (b). Defect dipoles can be reoriented through the movement of the oxygen vacancy within the octahedron as shown in Figure 6.3 (c). [3][14] Robels and Arlt attributed aging to reorientation of defect dipoles, which caused the clamping of domain walls in acceptor doped ferroelectric ceramics.[15] Warren *et al*. proved using electron paramagnetic resonance (EPR)[16] that defect dipoles could be aligned by displacement of oxygen vacancy along with the spontaneous polarization in polycrystalline PZT ceramics.

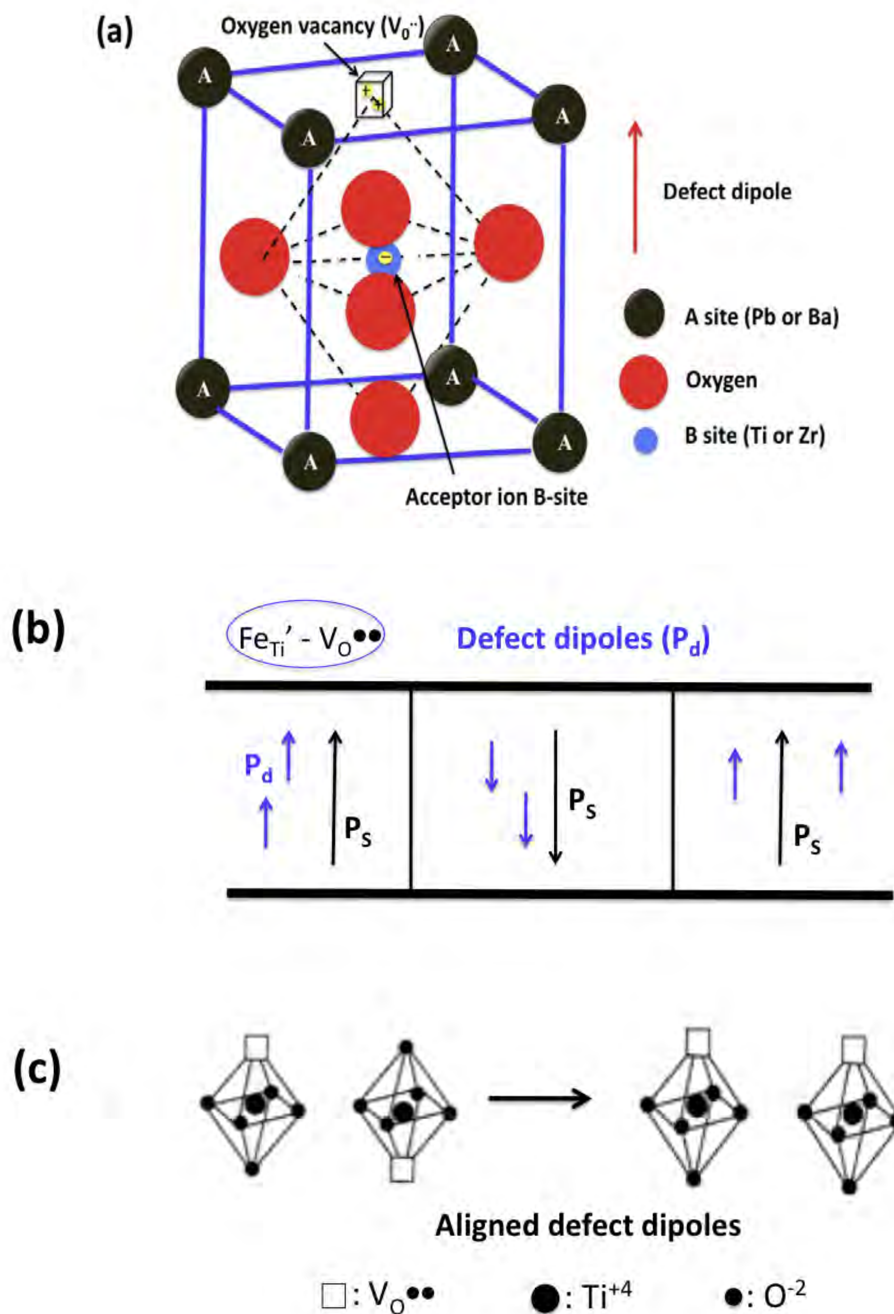

Figure 6.3. Illustrations of volume effect for aging: (a) a defect dipole within the unit cell, in practice distributed defect dipoles are also possible; (b) domain stabilization by defect complexes interacting with the spontaneous polarization; (c) Aligned defect dipoles by the reorientation of oxygen vacancy within the octahedron

B. Domain Wall Effect

The second mechanism of aging is the domain wall effect, which pins domain wall motion, and hence reduces domain wall contributions to the properties. In this mechanism, charged defects such as electrons or oxygen vacancies diffuse to charged domain walls, fixing their position as illustrated in Figure 6.4. [17][18]

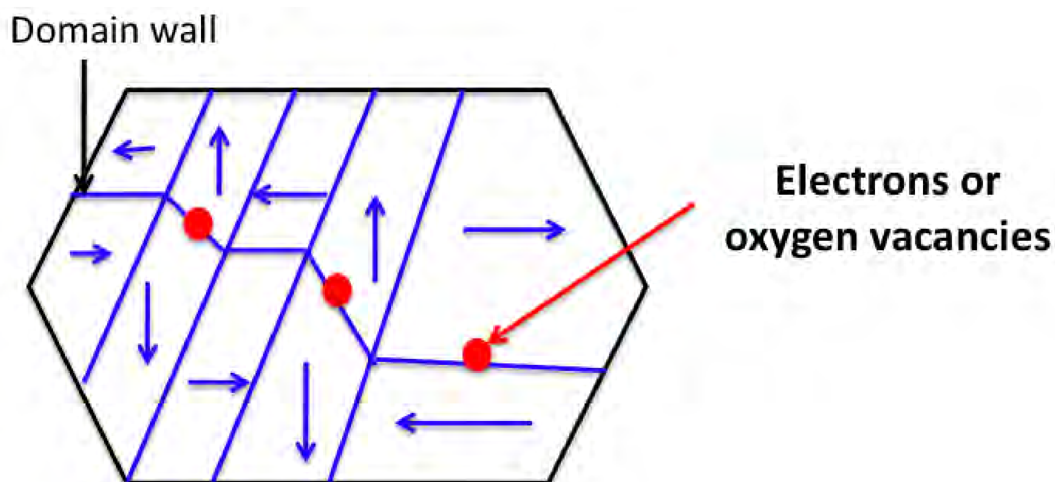

Figure 6.4. Schematic diagram of the domain wall-based aging mechanism

C. Interface Effect

The third mechanism for domain stabilization is the interface or grain boundary effect associated with formation of space charge by diffusing defects such as oxygen vacancies, electrons or ions to interfaces. These interfaces can be between the electrode and the film or at grain boundaries, as shown in Figure 6.5.[19] Some authors attribute the phenomenon of imprint to development of charges at interfaces.[20][21][22] All of these mechanisms may occur together,

and act to produce internal electric or mechanical strain fields, which stabilize the domain structure.

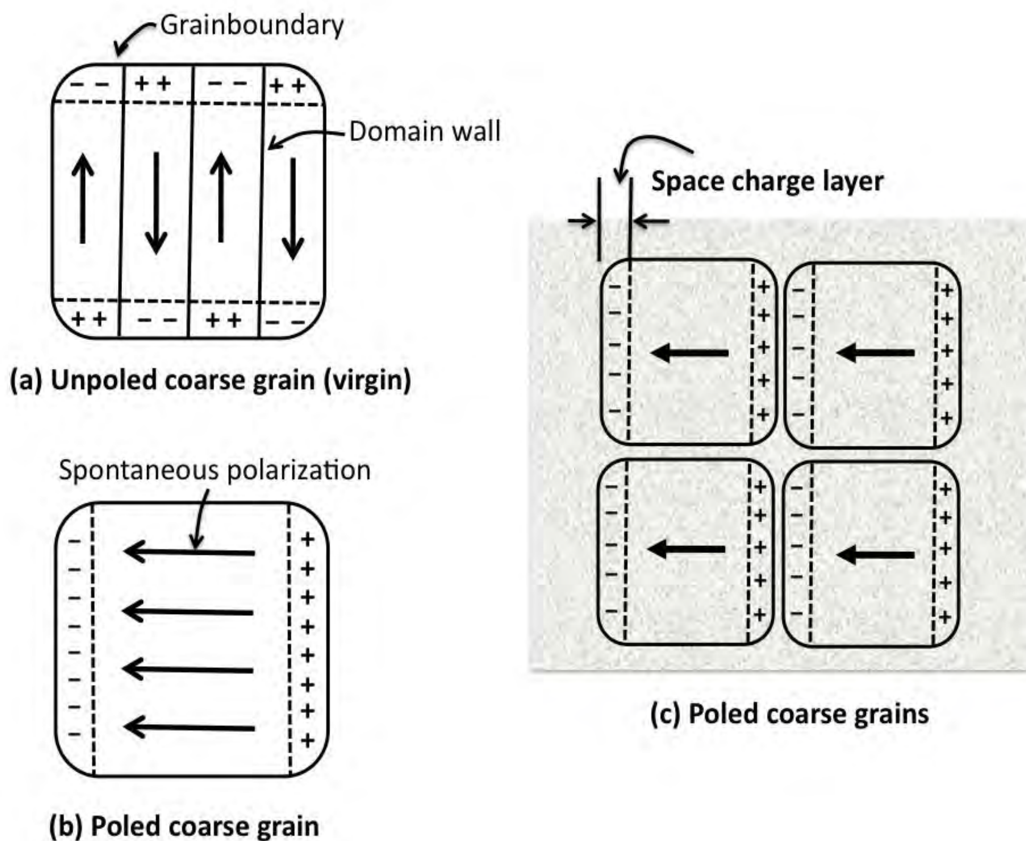

Figure 6.5. Schematic diagram of grain boundary effect on aging phenomena (modified from [24])

Thus, aging can be related to the reorientation of mobile charged defects such as electrons, oxygen vacancies and defect complexes, or reorientation of the domains in response to local strains; any of these can act to stabilize the domain state.

In this chapter, Rayleigh measurements were conducted as a function of time to directly analyze aging mechanisms of the dielectric response for patterned PZT thin film with different lateral feature sizes; these films were patterned by reactive ion etching. Two methods were used to obtain preferred polarization states in the ferroelectric. First, patterned PZT films were exposed to a dc bias (poling); secondly, films were poled at elevated temperature to promote alignment of defect dipole complexes.[20][23]

6.2. Experimental Procedure

6.2.1. Aging of the Rayleigh Parameters

Figure 6.6 shows the aging system used in the work. It consisted of a temperature controller and sample stage, which has a high temperature ceramic socket for a 24 pin DIP. The system was designed and built by Paul Moses and Jeff Long, of the technical staff of the Materials Research Institute. Measurements of the dielectric nonlinearity were made on 6 capacitors per DIP package for each feature size of patterned PZT film to achieve more statistical data using a Hewlett-Packard 4284A precision LCR meter at a frequency between 100 Hz and 10 kHz. The changes in Rayleigh parameters were monitored over time by sweeping the ac voltage from 0 to 2V, which was determined to be less than 1/3 to 1/2 of the coercive voltage. The dielectric data were plotted and analyzed using Origin and Microsoft Excel, using a logarithmic fit to quantify the aging.

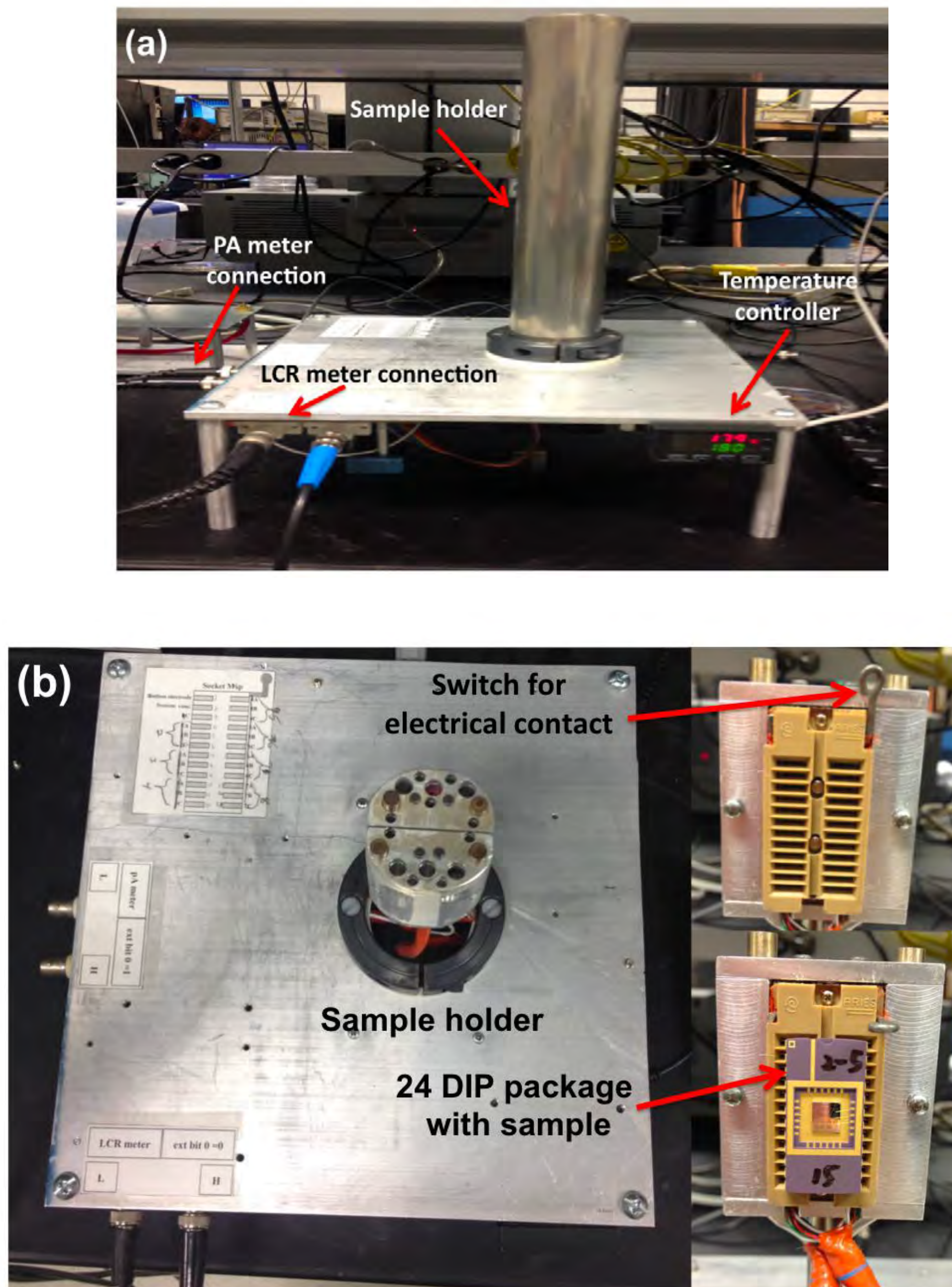

Figure 6.6. Images of (a) aging system with built in temperature controller, and (b) sample stage with a high temperature ceramic socket for wirebonded sample on 24 pin DIP package

6.2.2. Imprint of Patterned PZT (52/48) Thin Films – Poling and Hot Poling

The samples used were 0.6 μm thick patterned PZT (52/48) thin films prepared as described in Chapter 4; the films were patterned by a reactive ion etching process and then annealed at 500°C for 1min in RTA (in contrast to the ion milled devices described in Chapter 3). To generate imprint in patterned PZT films, the samples were poled in one of two ways. First, samples were poled at 150 kV/cm (9V) for 10 or 20 minutes. Secondly, samples were poled at 150 kV/cm (typically two times the coercive field) for 10 minutes at 150°C (the positive bias was applied to the top electrode with respect to the bottom electrode) and then cooled to room temperature while maintaining the dc voltage. After poling, the Rayleigh parameters were measured over time by sweeping the ac voltage up to ± 2V with a Hewlett-Packard 4284A precision LCR meter at a frequency of 10 kHz.

6.2.3. Polarization Measurement

Polarization - electric field loops were measured on patterned samples to determine their high voltage response using an RT-66A Ferroelectric Test System (Radiant Technology, Inc.). The measurement frequency was 100 Hz and the applied ac voltage ranged from 5 to 20 volts.

6.3. Results and Discussion

6.3.1. Effect of Poling and Hot Poling on The Rayleigh Parameters of Patterned PZT Thin Films

The Rayleigh parameters were determined by fitting the linear region of the ac field dependent dielectric data as shown in Figure 6.7. The reversible Rayleigh coefficient (ε_{init}) is

associated with the intrinsic contribution and reversible domain wall motion, while the irreversible Rayleigh constant (α) is dominated by motion of domain walls.

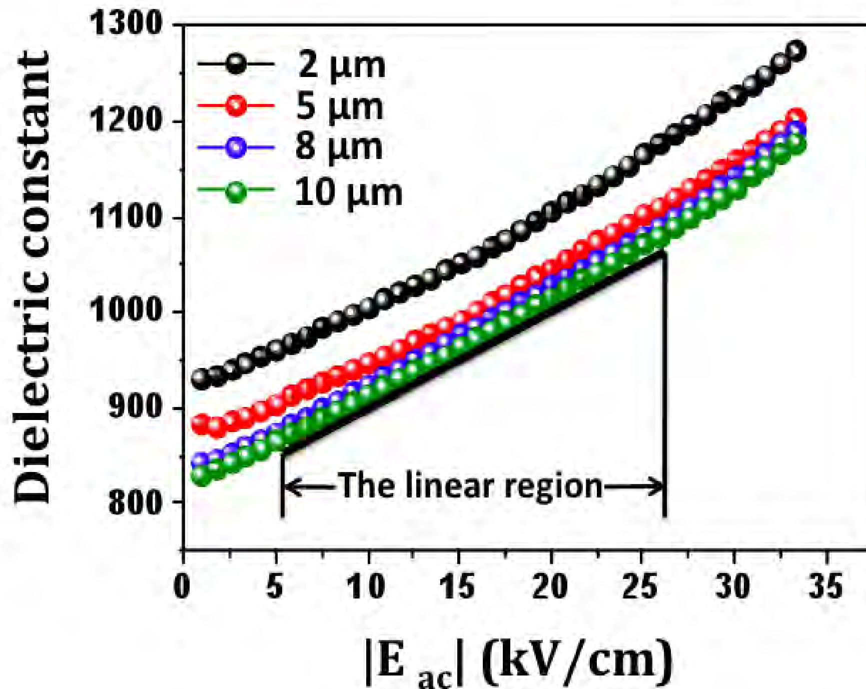

Figure. 6.7. The dielectric constant as a function of ac electric field of poled (at 150 kV/cm for 10min) 0.6 µm thick patterned PZT (52/48) thin films with different lateral feature sizes (as shown in the caption)

Figure 6.8 shows a comparison of the ε_{init} and α values for patterned PZT films with different feature sizes as a function of poling time compared with an unpoled sample. The data are averaged from measurements on 6 different samples for each feature size.

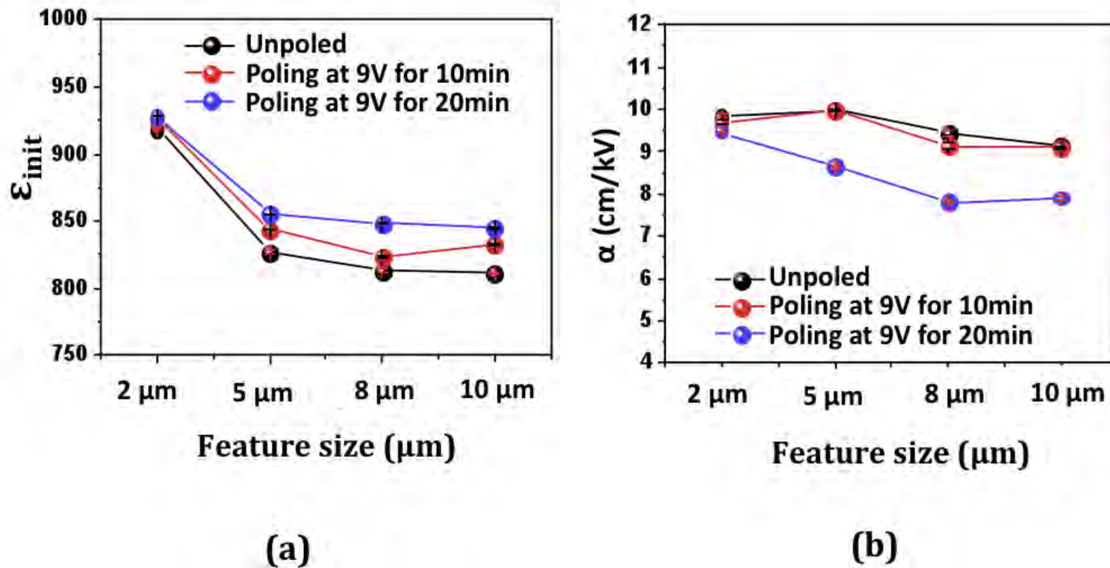

Figure 6.8. Variation of (a) ε_{init} and (b) α values for a 0.6 µm thick patterned PZT (52/48) thin films as a function of poling time with the top electrode at positive bias. Films were poled at 150 kV/cm, which is two times the coercive field of the film

First, it can be seen that ε_{init} and α increase with decreasing feature size, presumably due to an increase in domain wall mobility because of declamping.[(25)(26)(27)(28)] As discussed in chapter 3, after patterning, the potential energy profile for domain wall motion is changed and the film is less clamped by the substrate. It is proposed that this occurs because the interaction between the film and substrate provides a significant source of pinning for domain wall motion that can be reduced as the film is laterally patterned.

Secondly, a change in the Rayleigh parameters is seen after room temperature poling. The irreversible Rayleigh coefficients (α) decreased after poling, presumably because the domain state is stabilized and potentially because the density of domains walls is reduced. The result is a reduction of the irreversible extrinsic contributions to the dielectric response of this

film, as shown in Figure 6.8 (b). With increasing poling time, α values decreased further. It suggests that the longer the poling time, the more stable the domain configuration becomes.

In the same way, hot poling significantly reduces both Rayleigh parameters. Figure 6.9 shows the effect of hot poling (at 150 °C) on the dielectric response of patterned PZT (52/48) thin films compared to room temperature poling at the same field values (150 kV/cm) for 10 min.

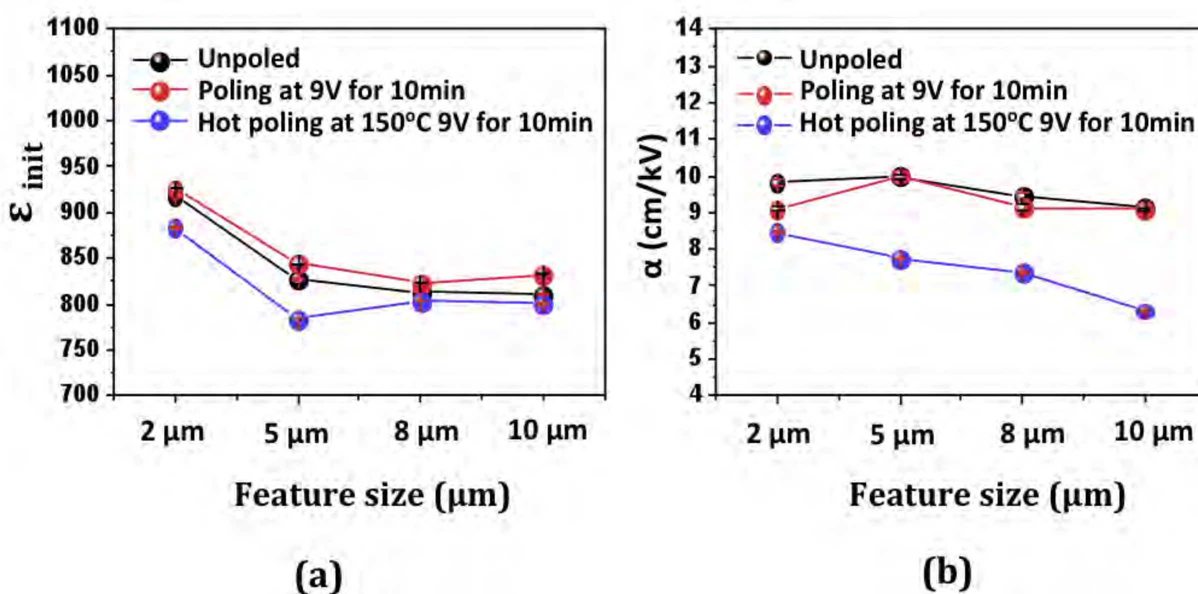

Figure 6.9. Variation of (a) ε_{init} and (b) α values of 0.6 μm thick patterned PZT (52/48) thin films as a function of room temperature poling and hot poling with the top electrode at positive bias.

There are several potential reasons why the Rayleigh constants decrease further on hot poling relative to room temperature poling. One possibility is that the thermal energy facilitates alignment of dipole complexes (potentially V_{Pb}'' - $V_o^{\bullet\bullet}$) so the stability of the domain state is improved.[23] It is also possible that the additional thermal energy promotes longer range motion

of mobile species such as oxygen vacancies, or injection of charge from one or both electrodes.

6.3.2. Rayleigh Parameters of Aging Behavior on Patterned PZT Thin Films

As mentioned earlier, there are multiple aging mechanisms reported for ferroelectric materials in the literature. Among the possible mechanisms are space charge creation,(19) defect dipole reorientation,(15) or redistribution and drift of charge carriers (29)(30), which stabilize the domain structure over time. Here, the samples described in the previous section were measured as a function of time after poling in order to assess:

1) The effect of lateral feature size on the aging rates of Rayleigh parameters
2) The effect of imprint on aging of the Rayleigh parameters
3) A comparison of the ratio of the irreversible to reversible Rayleigh parameters over time as a function of the poling conditions.

Figure 6.10 shows the aging rate of the Rayleigh parameters for 0.6 μm thick patterned PZT (52/48) thin films. First, the aging rate of reversible and irreversible Rayleigh coefficients was nearly constant for all lateral feature sizes, as shown in Figure 6.10 for samples prepared by reactive ion etching under the conditions described in section 4.2. In contrast, as mentioned in chapter 3, the ε_{init} and α values of argon ion milled parts aged more rapidly with decreasing serpentine line width due to local non-stoichiometry or altered crystallinity at the sidewalls; this was attributed to domain pinning. However, the Rayleigh parameters for the reaction ion etched unpoled PZT features of samples are a weak function of size. This suggests that the reactive ion etching process utilized does not significantly perturb the pinning distribution for domain walls.

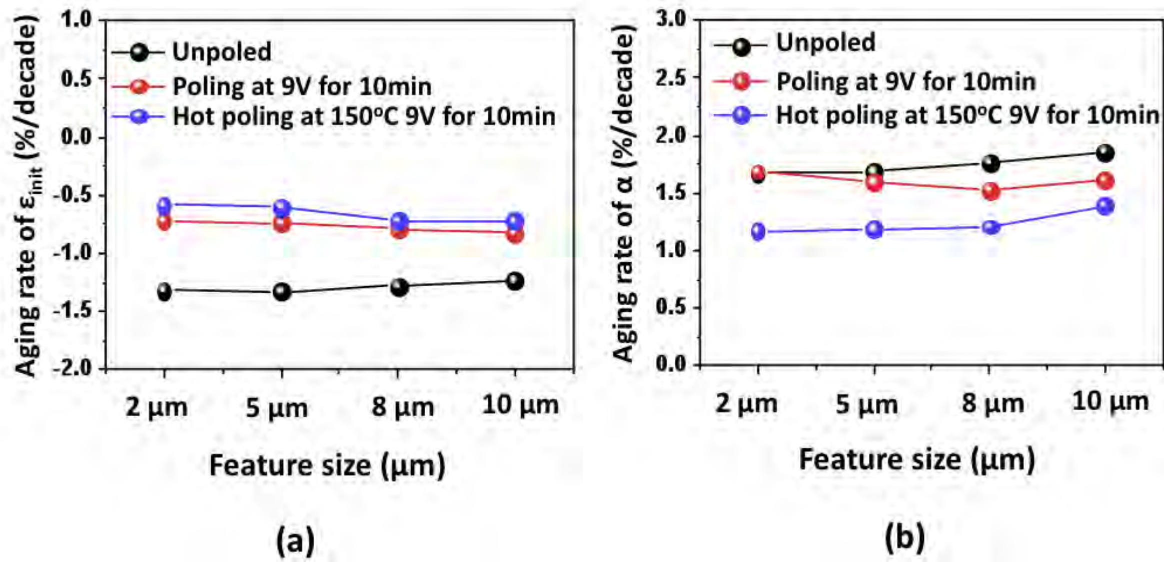

Figure 6.10. Comparison of the aging rate of Rayleigh parameters for 0.6 μm thick patterned PZT (52/48) thin films patterned by reactive ion etching

Second, it is clear that hot poling significantly reduces the aging rates relative either to unpoled samples or room temperature poling. As mentioned earlier, imprint which results from hot poling helps lock in a domain configuration and reduces the aging rate of PZT film.[(31)(32)(33)(34)] Imprint is observed as a voltage shift in the P-E hysteresis loop due to creation of internal fields.[(35)(36)(37)] Figure 6.11 shows the development of imprint in the films used in this thesis, with different poling conditions. The polarization – electric field (P-E) hysteresis loops was taken prior to and after poling at 5V, 10V, 15V and 20V and a frequency at 100Hz. Figure 6.11 (a) shows the P-E hysteresis loops and (b) generated internal field of patterned PZT (52/48) thin films. Both room temperature poled and hot poled samples have loops that are shifted negatively along the electric field axis. The magnitude of the shift is consistent with the aging rates: smaller aging rates correspond to larger internal fields.

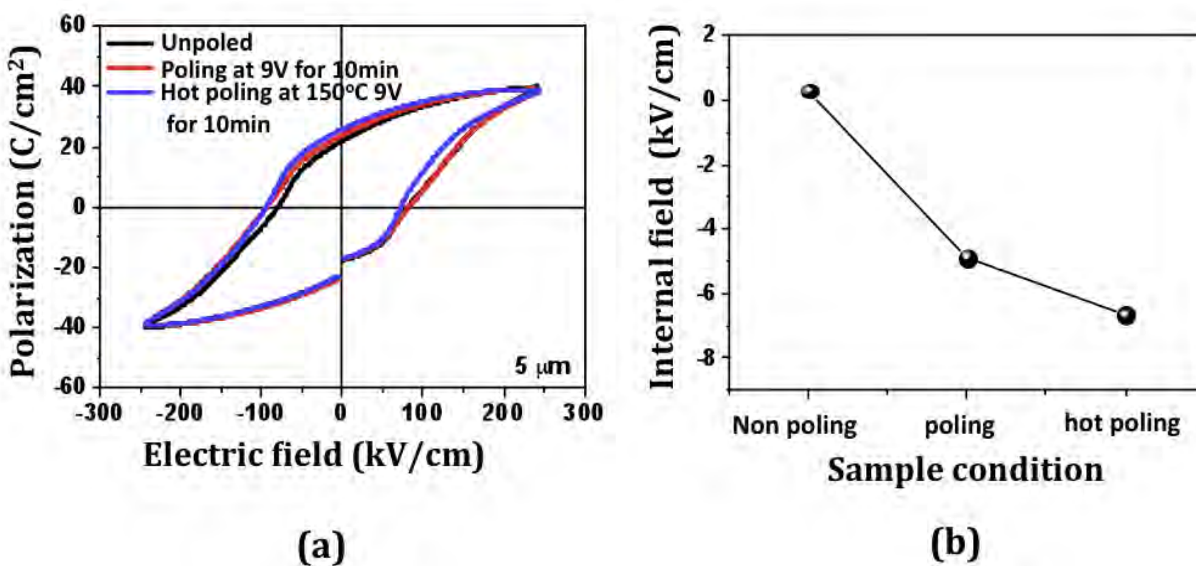

Figure 6.11. (a) The P-E hysteresis loops and (b) plot of internal fields after imprint for unpoled, room temperature poled and hot poled antenna patterned PZT (52/48) thin films

Poling at 150°C reduced the aging rate to ~ 0.6 %/decade for ε_{init} and 1.1 %/decade for α values, in comparison with aging rates of unpoled samples ~ 1.3 %/decade for ε_{init} and ~1.8 %/decade for α. Therefore, it is suggested that the thermal energy facilitates alignment of dipole complexes or migration of charge carriers, so that the stability of the domain state is improved.(23)(36)(37)

Third, the change in the ratio of the irreversible to reversible Rayleigh parameters (α / ε_{init}) was calculated from the aging data after poling either at room temperature or 150°C. Figure 6.12 illustrates the change in the ratio of α / ε_{init} over time and Figure 6.13 shows the aging rate of α / ε_{init} after imprint. Note that there were 300 data points in each graph. It can be seen that all feature sizes shows the same trend; α / ε_{init} decreased rapidly over short time scales (on the order of 1-150 seconds) and then gradually decreased at longer time. This could be a result of

domain walls that originally moved irreversibly at short times after poling gradually pinning into deeper wells. This would shift the balance between irreversible and reversible domain wall motion, and produce the rapid initial aging rates.

Figure 6.14 compares the aging of $\alpha/\varepsilon_{init}$ as a function of the poling methods. It was found that $\alpha/\varepsilon_{init}$ in unpoled samples changes by 100% (i.e. $\alpha/\varepsilon_{init}$ decreased from 0.0188 cm/kV to 0.0091 cm/kV) in 30000 second. After room temperature poling, $\alpha/\varepsilon_{init}$ decreased by 45 % (from 0.01425 cm/kV to 0.00765 cm/kV), while hot poling lead to a decrease of 35 % (from 0.00985 cm/kV to 0.00642 cm/kV) in the same time frame.

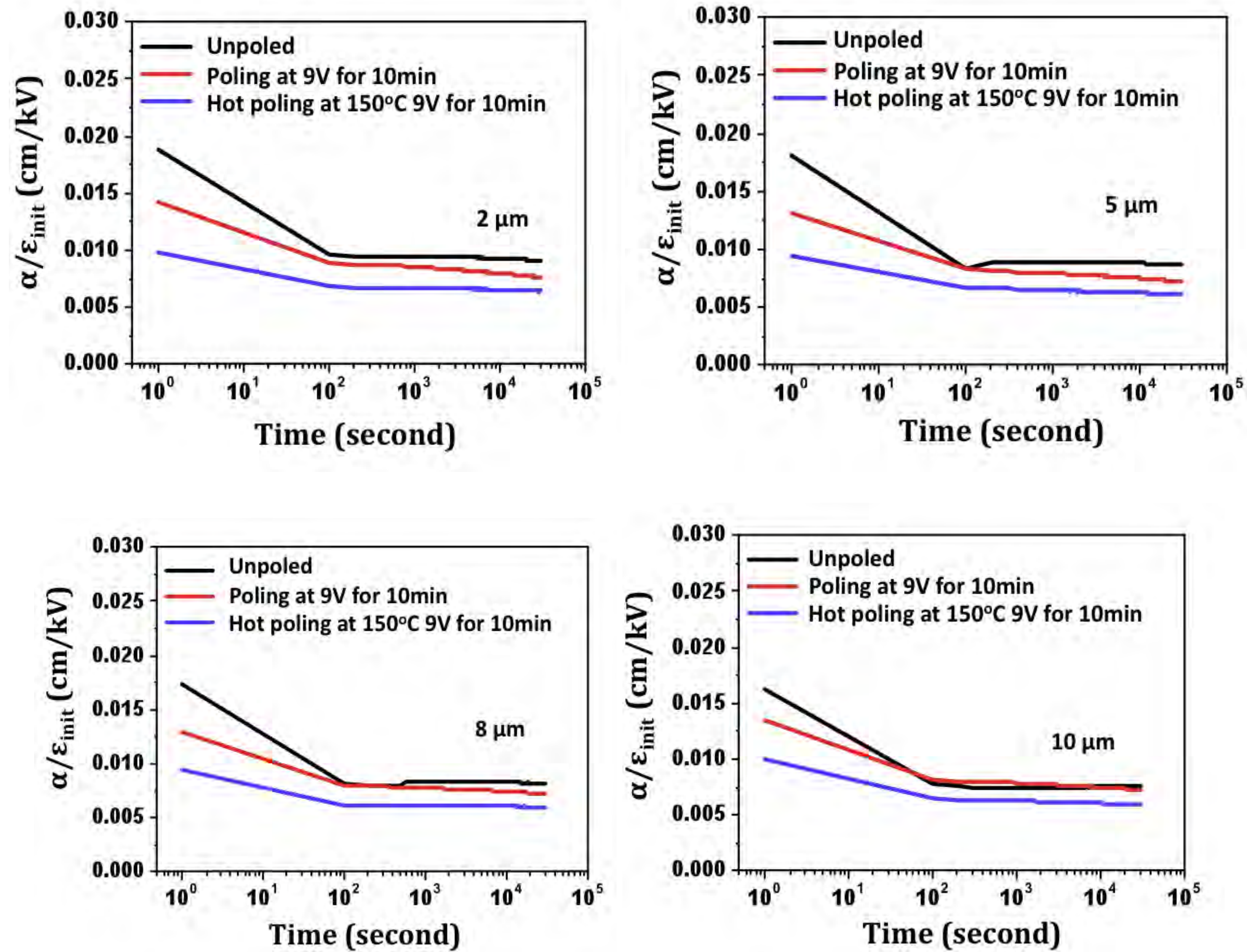

Figure 6.12. Plots of the ratio of irreversible to reversible Rayleigh parameters ($\alpha/\varepsilon_{init}$) as a function of time after imprint

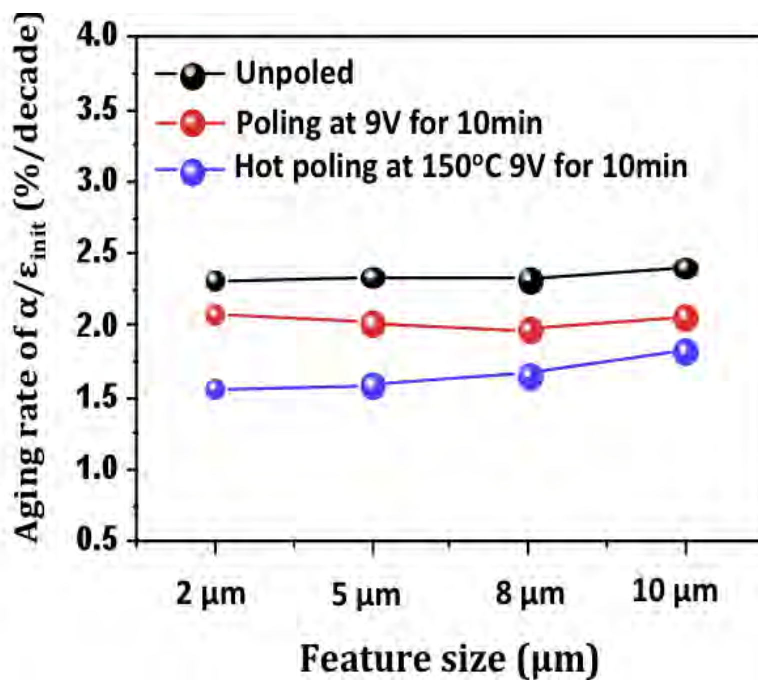

Figure. 6.13. Comparison of the aging rate of the ratio of $\alpha/\varepsilon_{init}$ for 0.6 μm patterned PZT (52/48) thin films after imprint

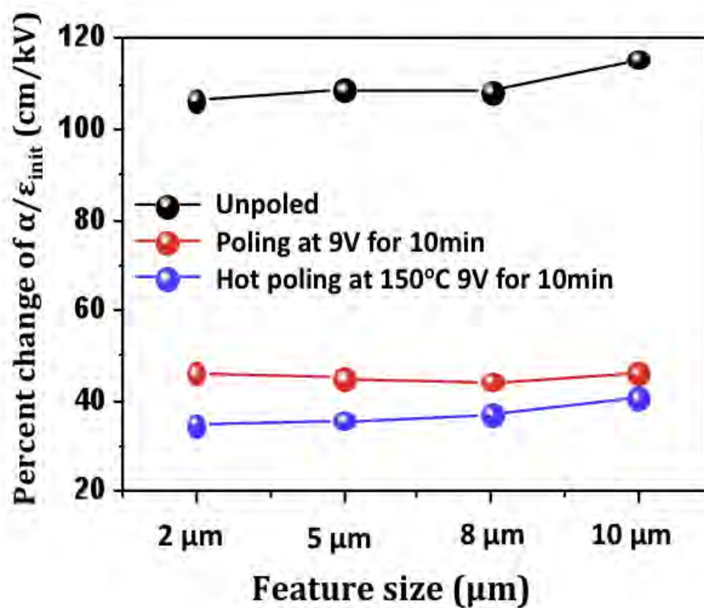

Figure 6.14. Comparison of percent changes in $\alpha/\varepsilon_{init}$ response for the aging period of 30000 seconds for unpoled, room temperature poled and hot poled patterned PZT (52/48) thin films

6.4. Conclusions

The Rayleigh law was applied to investigate the nonlinearity of dielectric response of antennae patterned PZT (52/48) thin films as a function of lateral feature size and poling conditions. The ε_{init} and α values increased with decreasing lateral feature size, probably due to an increase in domain wall mobility because of declamping. This suggests that the interaction between the film and substrate provides a significant source of pinning for domain wall motion.

The effect of room temperature poling and poling time on the Rayleigh parameter was studied. After room temperature poling at 150 kV/cm, the irreversible Rayleigh coefficients (α) decreased relative to the unpoled samples due to an improvement in the domain state stability. Also, with increasing poling time, α decreased further. This suggests that the longer the poling time, the more stable the domain configuration becomes.

The study of the dielectric nonlinearities as a function of room temperature poling and hot poling was performed. Hot poling significantly reduces both Rayleigh parameters. The results suggest that thermal energy facilitates alignment of defect dipole complexes so that the stability of the domain state is improved. It is also possible that the additional thermal energy promotes longer range motion of mobile species such as oxygen vacancies, or injection of charge from one or both electrodes.

The time dependence of dielectric nonlinearity was also investigated to assess the effect of lateral feature size and imprint on the aging rates of Rayleigh parameters. The aging rate of reversible and irreversible Rayleigh coefficients was constant for all lateral sizes for samples prepared by reactive ion etching under the conditions described in section 4.2. Rayleigh parameters for the reaction ion etched unpoled PZT features of samples are a weak function of size for an aging period of 30000 seconds. This suggests that the reactive ion etching process

utilized does not significantly perturb the pinning distribution for domain walls.

After imprint, there was a voltage shift in the P-E hysteresis loops due to creation of internal field by space charge or defect dipoles. The internal field stabilizes the domain configuration. Poled and hot poled samples have loops that are shifted negatively along the electric field axis. The magnitude of the shift is consistent with the aging rates: smaller aging rates correspond to larger internal fields. Poling at 150°C reduced the aging rates to ~ 0.6 %/decade for ε_{init} and 1.1 %/decade for α. In comparison, the aging rate of unpoled samples were ~ 1.3 %/decade for ε_{init} and ~1.8 %/decade for α.

Values of α / ε_{init} were evaluated from the aging data after poling either at room temperature or 150°C. All feature sizes showed the same trend; α / ε_{init} decreased rapidly over short time scales (on the order of 1-150 seconds) and then gradually decreased at longer time. The $\alpha/\varepsilon_{init}$ in unpoled samples changes by 100% in 30000 second. After room temperature poling, $\alpha/\varepsilon_{init}$ decreased by 45 % while hot poling led to a decrease of 35 % in the same time frame.

6.5. References

1. Y. A. Genenko, J. Glaum, M. J. Hoffmann, K. Albe, "Mechanisms of aging and fatigue in ferroelectrics," Materials Science and Engineering B. 192, pp. 52-82 (2015)

2. Yuhuan Xu, "Ferroelectric Materials and Their Applications," NorthHolland (1991)

3. G. Arlt and H. Neumann, "Internal bias in ferroelectric ceramics: Origin and time dependence," Ferroelectrics, Vol. 87, pp. 109-120 (1988)

4. W. A. Schulze and K. Ogino, "Review of literature on aging of dielectrics," Ferroelectrics, Vol. 87, pp. 361-377 (1988)

5. A. Kholkin, E. Colla, K. Brooks, P. Muralt, M. Kohli, T. Maeder, D. Taylor, and N. Setter, "Interferometric study of piezoelectric degradation in ferroelectric thin film," Microelectronic Engineering, Vol. 29, pp. 261-264 (1995)

6. P.V. Lambeck and G. H. Jonker, "The nature of domain stabilization in ferroelectric perovskites," J. Phys. Chem. Solids, Vol. 47, No. 5, pp. 453-461 (1986)

7. M.I. Morozov and D. Damjanovic, "Charge migration in Pb (Zr,Ti)O_3 ceramics and its relation to ageing, hardening, and softening," J. Appl. Phys. 107, 034106, pp. 1-10 (2010)

8. R.E. Alonso, P. del la Presa, A. Ayala, A. Lopez-Garcia and C. Livage, “The stability of $PbZr_{0.52}Ti_{0.48}O_3$ prepared by the sol-gel method,” Solid State Communications, Vol. 107, No. 4, pp. 183-187 (1998)

9. J. R. Scholz, “Aging rates in PZT ferroelectrics with mixed acceptor-donor dopants,” Masters thesis in Materials Science and Engineering, the Pennsylvania State University (2009)

10. W. L. Zhong, “Stabilization effects of manganese and cerium on the properties of PZT ceramics,” Ferroelectrics Letters. Vol. 2 (1), pp. 13-16 (1984)

11. S. Srilomsak, W. A. Schulze, S. M. Pilgrim, and F. A. Williams Jr., “Harmonic analysis of polarization hysteresis of aged PZTs,” J. Am. Ceram. Soc., Vol. 88 [8] 2121–2125 (2005)

12. H. Dederichs and G. Arlt, “Aging of Fe-doped PZT ceramics and the domain wall contribution to the dielectric constant,” Ferroelectrics, Vol. 68, pp. 281-292 (1986)

13. R. G. Polcawich and S. Trolier-McKinstry, “Piezoelectric and dielectric reliability of lead zirconate titante thin films,” J. Mater. Res., Vol. 15, No. 11, pp. 2505- 2513 (2000)

14. X. Ren, “Large electric-field-induced strain in ferroelectric crystals by point-defect-mediated reversible domain switching,” Nature Materials, Vol. 3, pp. 91-94 (2004)

15. U. Robels and G. Arlt, "Domain wall clamping in ferroelectrics by orientation of defects," J. Appl. Phys. 73 (7), pp. 3454-3460 (1993)

16. W. L. Warren, G. E. Pike, K. Vanheusden, D. Dimos, B. A. Tuttle, and J. Robertson, "Defect- dipole alignment and tetragonal strain in ferroelectrics," J. Appl. Phys. Vol. **79** (12), pp. 9250-9257 (1996)

17. V.S. Postnikov, V.S. Pavlov, S.K. Turkov, "Internal friction in ferroelectrics due to interaction of domain boundaries and point defects," J. Phys. Chem. Solids, Vol. 31, pp.1785-1791 (1970)

18. W. Warren, D. Dimos, B. Tuttle, R. Nasby, G. Pike, "Electronic domain pinning in $Pb(Zr,Ti)O_3$ thin films and its role in fatigue," Appl. Phys. Lett. Vol. 65, pp. 1018-1020 (1994)

19. M. Takahasahi, "Space charge effect in lead zirconate titanate ceramics caused by the addition of impurities," Jpn. J. Appl. Phys. Vol. 9, pp. 1236-1246 (1970)

20. U. Robels and G. Arlt, "Domain wall clamping in ferroelectrics by orientation of defects," J. Appl. Phys. 73 (7), pp. 3454-3460 (1993)

21. W. L. Warren, G. E. Pike, K. Vanheusden, D. Dimos, B. A. Tuttle, and J. Robertson,

"Defect- dipole alignment and tetragonal strain in ferroelectrics," J. Appl. Phys. Vol. **79** (12), pp. 9250-9257 (1996)

22. J. Lee, R. Ramesh, and V.G. Keramidas, "Imprint and oxygen deficiency in (Pb,La)(Zr,Ti)O_3 thin-film capacitors with La-Sr-Co-O electrodes," Appl. Phys. Lett. Vol. 66, pp. 1337-1339 (1995)

23. G.E. Pike, W.L. Warren, D. Dimos, B.A. Tuttle, R. Ramesh, J. Lee, V.G. Keramidas, and J.T. Evans, Jr., "Voltage offsets in (Pb,La)(Zr,Ti)O_3 thin films," Appl. Phys. Lett. Vol. 66, pp. 484-486 (1995)

24. K. Okazaki and K. Nagata, "Effects of grain size and porosity on electrical and optical properties of PLZT ceramics," J, American Ceramic Society, Vol. 56, No. 2, pp. 82-86 (1973)

25. D. Dimos, W.L. Warren, M.B. Sinclair, B.A. Tuttle, and R.W. Schwartz, "Photoinduced hysteresis changes and optical storage in (Pb,La)(Zr,Ti)O_3, thin films and ceramics," J. Appl. Phys. Vol. 76, pp. 4305-4315 (1994)

26. W.L. Warren, D. Dimos, G.E. Pike, K. Vanheusden, and R. Ramesh, "Alignment of defect dipoles in polycrystalline ferroelectrics," Appl. Phys. Lett. Vol. 67, pp. 1689-1691 (1995)

27. V. Nagarajan, A. Roytburd, A. Stanishevsky, S. Prasertchoung, T. Zhao, L. Chen, J. Melngailis, O. Auciello and R. Ramesh, “Dynamics of ferroelastic domains in ferroelectric thin films,” Nature Materials, Vol. 2, pp.43-47 (2003)

28. D. A. Hall, “Rayleigh behavior and the threshold field in ferroelectric ceramics,” Ferroelectrics, Vol. 223, pp. 319-328 (1999)

29. S. Li, W. Cao, and L. E. Cross, “The extrinsic nature of nonlinear behavior observed in lead zirconate titanate ferroelectric ceramic,” J. Appl. Phys. Vol. 69, pp. 7219-7224 (1991)

30. P. Bintachitt, S. Jesse, D. Damjanovic, Y. Han, I.M. Reaney, S. Trolier-McKinstry, and S.V. Kalinin, “Collective dynamics underpins Rayleigh behavior in disordered polycrystalline ferroelectrics,” Proc. Natl. Acad. Sci. U.S.A. Vol. 107, pp. 7219-7224 (2010)

31. F. Griggio, S. Jesse, A. Kumar, O. Ovchinnikov, H. Kim, T. N. Jackson, D. Damjanovic, S.V. Kalinin, and S. Trolier-McKinstry, “Substrate Clamping Effects on Irreversible Domain Wall Dynamics in Lead Zirconate Titanate Thin Films,” Phys. Review Lett. Vol. 108, pp. 157604-1-5 (2012)

32. H. J. Hagemann, “Loss mechanisms and domain stabilization in doped $BaTiO_3$,” J. Phys.

C: Solid State Phys., Vol. 11, 3333–3344 (1978)

33. Y. A. Genenko and D. C. Lupascu, "Drift of charged defects in local fields as aging mechanism in ferroelectrics," Phys. Rev. B, Vol. 75, 149907-1-14 (2007)

34. S. Gotmare, S. O. Leontsev, and R. E. Eitel, "Thermal degradation and aging of high-temperature piezoelectric ceramics," J. Am. Ceram. Soc. Vol. 93 [7], pp. 1965-1969 (2010)

35. J. P. de Medeiros, M. H. Lente and J.A. Eiras, "Influence of poling temperature on aging and thermal stability of PZT ceramics," Proc. IEEE Ultrasonics Symposium, 1051-0117/94/0000-0955, pp. 955-958 (1994)

36. D.J. Kim, S.H. Kim, J.P. Maria and A. I. Kingon, "Thermally induced imprint of PZT and SBT thin film," Mat. Res. Soc. Symp. Proc. Vol.541, pp.469-474, (1999)

37. W. L. Warren, G.E. Pike, D. Dimos, K. Vanheusden, H.N. Al-Shareef, B. A. Tuttle, R. Ramesh, and J.T. Evans, Jr., "Voltage shifts and defect-dipoles in ferroelectric capacitors," Mat. Res. Soc. Symp. Proc. Vol. 433, pp. 257-266 (1996)

Chapter 7

Conclusions and Future Work

In many cases, fabrication of the electronic devices requires the ferroelectric layer be laterally patterned. Many researchers have published that sidewall damage and clamping influenced the resulting electrical and piezoelectric properties of patterned features. In this research, serpentine and antenna shapes were designed and fabricated to investigate these two factors and their influence on aging, reliability and leakage current in patterned PZT thin films. This chapter summarizes the results of each chapter and recommends future work.

7.1. Effect of Feature Size on Dielectric Nonlinearity of Serpentine Patterned PZT Films

Serpentine patterned PZT (52/48) thin film was fabricated using Ar-ion milling. The dielectric and ferroelectric properties of patterned PZT (52/48) thin films patterned were investigated. From the result of P-E hysteresis, it was observed that the 10 μm serpentine patterns were less clamped by the substrate than was the case for the other features. The dielectric nonlinearity in the patterned PZT thin films was described using the Rayleigh law at modest ac electric fields. After recovery annealing, it was observed that ε_{init} and α increased for smaller feature sizes. The increased Rayleigh parameters (ε_{init} and α) were attributed to reduction in the number of deep potential wells associated with substrate clamping, perhaps with commensurate changes in the length scale over which domain walls interact. However, etched patterns also aged more rapidly. It is conjectured that the sidewall damage produces shallow

wells. Thus, it is believed that clamping at the film/substrate interface produces deeper wells, which prevent some fraction of the spontaneous polarization to switch at high fields and sidewall damage produces shallow wells that lower Rayleigh constant at small fields but which can be overcome by large fields to produce high P_r in P-E measurements.

7.2. DC Electrical Field Reliability and Conduction Mechanisms of Antennae Patterned PZT Films

Antenna patterned 0.6 μm thick PZT (52/48) thin film was fabricated using reactive ion etching. Highly accelerated lifetime testing (HALT) was conducted at three different temperatures and three different voltages for all feature sizes (2μm, 5μm, 8μm, 10μm). It was observed that the range of activation energies for all feature sizes was 0.82eV~ 1.1eV; the voltage acceleration factors (n) for all feature sizes are 3.4 ~ 5.2. It was found that the 2 μm arm size has longer lifetime (t_{50} = 79.8 hour at 150 ^{o}C, 225 kV/cm) and lower activation energy (E_a = 0.82 eV) than the 10 μm arm size (t_{50} =15.5 hour at 150 ^{o}C, 225 kV/cm, E_a = 1.1 eV), It is believed that trapping/detrapping processes at the sidewall were more important in governing lifetime for smaller feature sizes. Also, it is possible that the activation energy of 2 μm feature size is smallest (~0.82 eV) because of a broader distribution of trap centers.

A second failure pathway can occur through the “bulk” of the ferroelectric. It was hypothesized that the shorter failure times in larger feature sizes were associated with a higher density of domain walls acting as pathways for the failure-inducing species. The activation energy for failure might then be correlated with the activation energy for motion of the carriers. Since the activation energy (~ 1 eV) is higher than that reported for oxygen vacancy migration (~0.6 eV), it is possible that detrapping of carriers from domain walls dominates the response.

HfO_2 was coated on PZT film to reduce sidewall damage using ALD. After ALD coating, the lifetime of all features sizes improves. In addition, the measured activation energies were very similar for all feature sizes. These results suggest that after ALD coating, the sidewall damage is partially recovered, so the effect of sidewall damage on the breakdown mechanism is reduced.

I-V measurements were performed as function of temperature to investigate possible conduction mechanism. Reasonable fits to the current data were obtained via either the Schottky or the Poole-Frenkel mechanisms; of these two, more realistic values for the refractive index were obtained from the Schottky model. The Schottky barrier heights with different feature sizes ranged from 0.4 to 0.56 eV.

7.3. Aging Behavior in Patterned PZT (52/48) Thin Films

The Rayleigh law was applied to quantify the nonlinearity of dielectric response of antenna patterned PZT (52/48) thin films with time as a function of different poling conditions. It was found that for these reactive ion etching conditions, the lateral feature size did not significantly influence the aging rate of the reversible and irreversible Rayleigh parameters. This suggests that the reactive in etching process utilized does not significantly perturb the pinning distribution for domain walls.

The effect of imprint on the aging rate of Rayleigh parameters was also studied. After imprint, there was a voltage shift in the P-E hysteresis loops due to creation of internal field by space charge or defect dipoles. Poling at 150°C reduced the aging rate to ~ 0.6 %/decade for ε_{init} and 1.1 %/decade for α values; in contrast, the aging rates of unpoled samples were ~ 1.3 %/decade for ε_{init} and ~1.8 %/decade for α. All feature sizes show that the ratio of α / ε_{init}

decreased rapidly at short time scales (on the order of 1-150 seconds) and then gradually decreased over time. Thermal poling dielectric aging rate for $\alpha/\varepsilon_{init}$ ratio has lowest value. It is believed that thermal energy facilitates alignment of domains with poling field and it is accompany with stabilization of domain configurations.

7.4. Future Work

7.4.1. Thermally Stimulated Depolarization Current (TSDC) in Patterned PZT (52/48) Thin Films

In chapter 5, the time dependence of the behavior of patterned PZT films was examined, with an emphasis on the time-dependent dielectric breakdown and leakage current. However, the origin of the defects, which cause degradation in PZT films has not been clarified. Therefore, thermally stimulated depolarization current (TSDC) technique should be undertaken to understand the fundamental origins of the observed defects.[1][2] Each peak from the depolarization current as a function of temperature will be associated with defects such as oxygen vacancies, trapped charges or defect dipoles. In future work, it is proposed that TSDC measurement could be used to probe the main defect responsible for degradation under HALT for each lateral size.

Figure 7.1 illustrates profiles of temperature and electric field in TSDC measurement. Prior to the experiment, the sample is heated to the polarization temperature (T_p), which will facilitate defects to align with the electric field (E_{app}). Following poling, the sample is cooled down to room temperature while maintaining the dc electric field. Then, the sample is shorted

and immediately heated with a constant heating rate. The depolarization current from the relaxing defects is collected during the TSDC measurement.

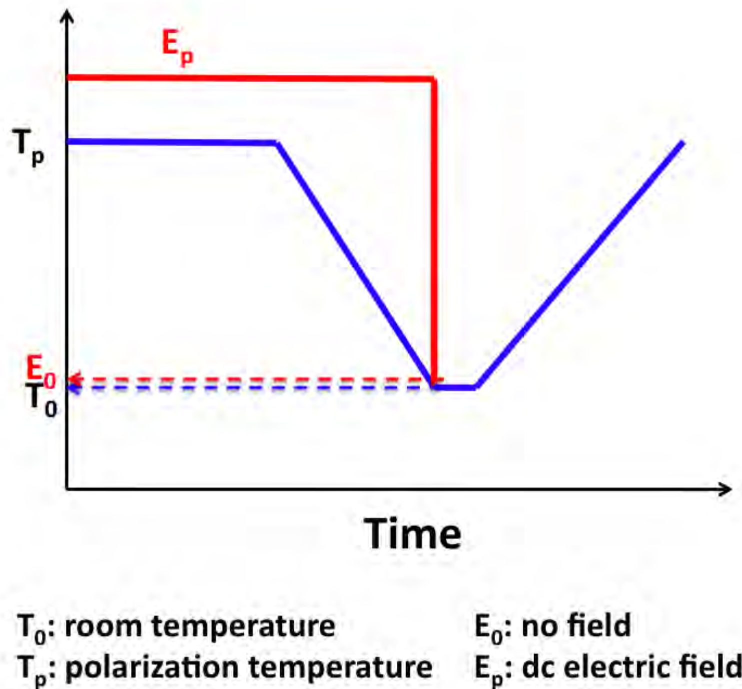

Figure 7.1. Schematic of TSDC field and temperature profile (taken from [2])

However, there is a challenge to measure accurate depolarization currents from PZT due to the pyroelectric effect. It has been reported that the electronic traps can be detected without interference from the pyroelectric effect by use of UV excitation, rather than electrical poling.(3) In order to fit curve and integrate peaks of depolarization current, the following equation should be used to estimate the activation energy, and the concentration of mobile charges and defect dipoles: (1)(2)

$$I(T) = n_0 s \exp\left(\frac{-E_a}{kT}\right) * \exp\left[-s/b\int_{T_0}^{T}\left(\frac{-E_a}{kT}\right)dT'\right]$$

$$s = b\frac{E_a}{kT^2{}_m \exp\left(\frac{-E_a}{kT_m}\right)} \qquad \text{equation (7.1)}$$

where E_a is the activation energy, T_m is the temperature corresponding to the peak maximum, and b is the heating rate.

It is recommended that the TSDC and HALT data be compared to quantify the defects and to study charge carrier transport.

7.4.2. Effect of Patterning Techniques on Reliability of Patterned PZT Thin Films

In previous work (chapters 3 and 6), it was observed that serpentine and antennae PZT film showed different aging behavior for different patterning techniques. Ar ion milled features showed that the ε_{init} and α values aged more rapidly with decreasing feature size, presumably due to local non-stoichiometry or altered crystallinity at the sidewalls. However, reactive ion etched parts showed that the aging rate of Rayleigh coefficients was nearly constant for all lateral feature sizes. This suggests that the defect distributions produced differ by patterning technique. Thus, the HALT and aging behavior of PZT thin films should be directly compared for various patterning techniques, including physical and chemical etching process as well as wet etching. Table 7.1 shows various etching techniques and their advantages and disadvantages.

Table 7.1. Summary of different etching techniques [4]

Etching techniques	Common Gases	Pros	Cons
Wet etching [5]	HCl and HF	- Excellent selectivity to platinum - Relatively high etch rate	- Highly isotropic and fast lateral etch rate - By products on the wafer surface
Ar ion milling [6]	Ar	- Variable control of the angle of incidence to remove re-deposition materials	- Poor selectivity - Low accuracy of endpoint on the desired layer
* ECR-RIE [7]	CCl_4/ CF_4/ Ar	- Anisotropic - Relatively good selectivity	- Extremely low volatility of the Zr and Ti by products
* ICP-RIE [8][9]	Cl_2/C_2F_6/Ar/BCl_3	- Anisotropic - Relatively good selectivity	

* ECR-RIE : electron cyclotron resonance reactive ion etching
* ICP-RIE: inductively coupled plasma reactive ion etching

Most patterning processes have re-deposition of etch by-products; furthermore the character of the sidewall prepared is likely to be a function of etching parameters such as the etch powers and pressures. Thus, different etching processes may change the reliability as well as the functional properties.

7.4.3. AC Electric Stress Reliability of Patterned PZT Thin Films

In this work (chapter 5), the lifetime and failure mechanisms were studied using DC HALT. However, there is no database of HALT measurement under AC electric stress. AC electric stress reliability in applications such as fuel injection system or inkjet print head system is essential.[10] It would be valuable to investigate differences between DC and AC reliability of patterned PZT thin films to determine whether the mechanisms responsible for failure are similar

or different. Figure 7.2 shows an image of the AC-HALT system with the high temperature ceramic socket for the 28 pin DIP package.

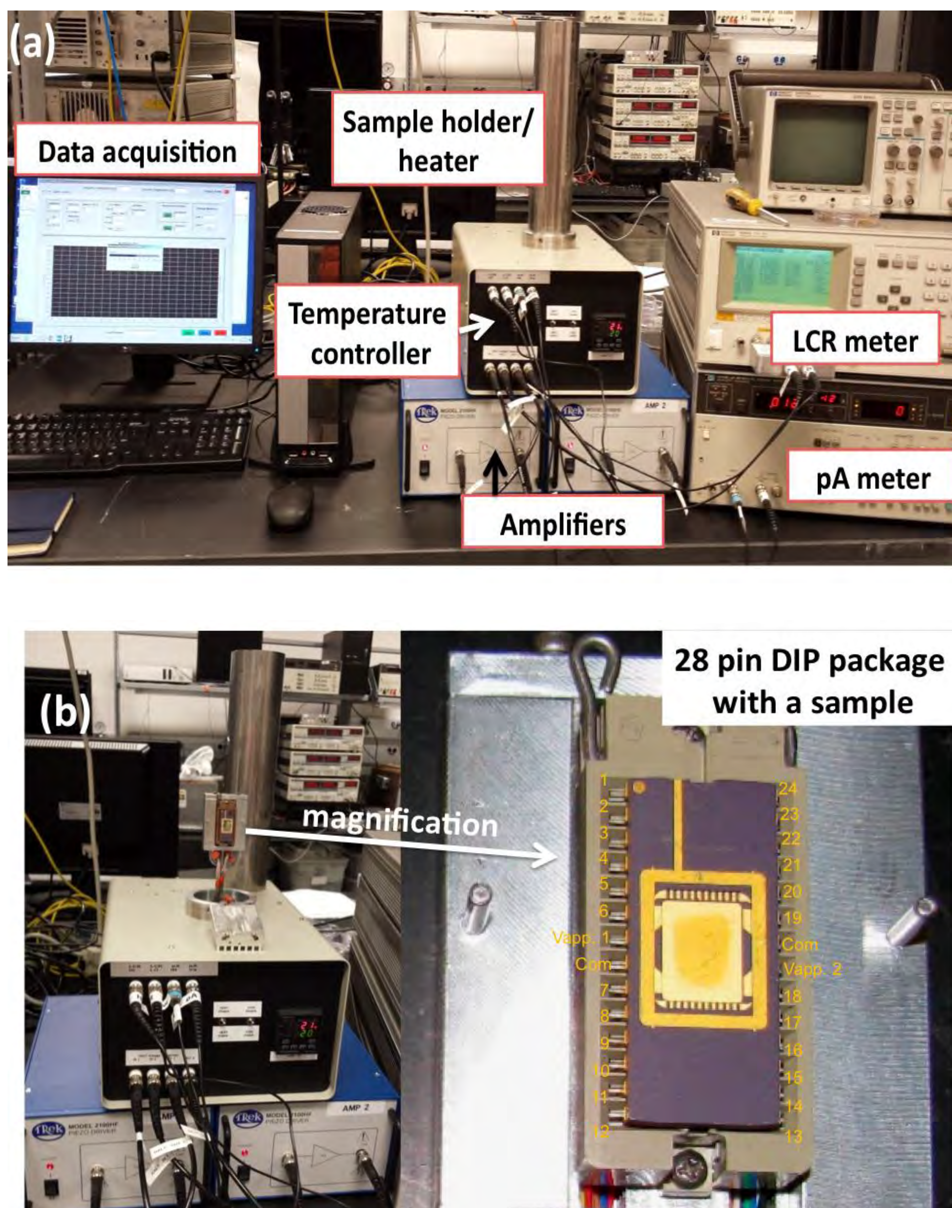

Figure 7.2. Images of (a) AC HALT system, which was composed of LCR meter, pA meter, amplifiers, temperature controller and sample holder and (b) sample stage with wirebonded sample on a 28 pin DIP package

7.4.4. Method of Classification Between Effect of Sidewall Damage and Bulk Damge of Patterned PZT Films

Many researchers have investigated the etching damage by using several etching techniques. Kim et al. investigated the etching damage on PZT thin films with a shadow dot mask, which was etched by inductively coupled plasma. (11) They showed that after etching process, it was observed strong damage of the PZT surface due to ion bombardment and chemical reaction from TEM analysis and reduction of the remanent polarization. In our research, Ni hard mask was used during etch process, so it is needed to examine a difference between effects of induced sidewall damage and surface / bulk damage on electrical properties of patterned PZT films. Two kinds of experiments will be conducted as shown in Figure 7.3. First, as shown in Figure 7.3 (a), the patterned PZT capacitor can be fabricated by using focused ion beam milling (FIB) with trenches around the perimeter of patterned PZT film to induce only sidewall damage. Second, to induce damage of surface/bulk and sidewall, Ar ion beam irradiates on the surface of PZT film as shown in Figure 7.3(b). I-V characteristics, P-E measurement, Rayleigh measurement can be conducted to compare effect of sidewall damage and bulk damage of patterned PZT films.

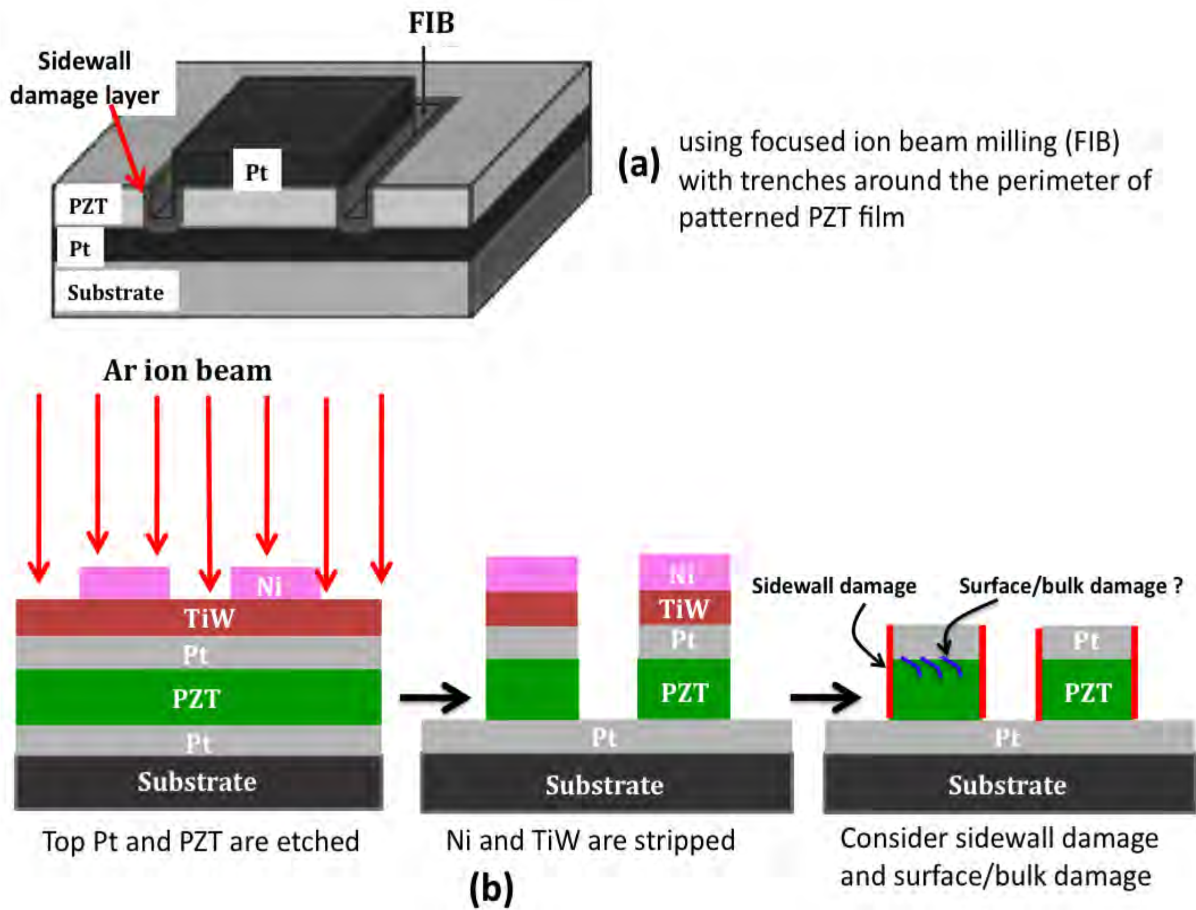

Figure 7.3. Schematic of two different etching process, FIB fabrication and Ar ion milling, of PZT thin film; (a) the patterned PZT capacitor can be fabricated by using focused ion beam milling (FIB) with trenches around the perimeter of patterned PZT and (b) PZT thin film will etch using Ar ion milling to pattern

7.5. References

1. T. Nishida, M. Echizen, T. Takeda, K. Uchiyama, T. Shiosaki, "Investigation of Crystal Defects in Lead Zirconate Titanate Films by Thermally Stimulated Current Measurement," 2007 Sixteenth IEEE International Symposium on the Applications of Ferroelectrics, pp. 234-235 (2007)

2. Wei-En Liu, "Impedance/thermally stimulated depolarization current and microstructural relations at interface in degraded perovskite dielectrics," PhD thesis in Materials Science and Engineering, the Pennsylvania State University (2009)

3. Zheng Wu and Michael Sayer, "Defect structures and fatigue in ferroelectric PZT thin films," Applications of Ferroelectrics, Proceedings of the Eighth IEEE International Symposium, pp. 244-247 (1992)

4. Ronald G. Polcawich and Jeffrey S. Pulskamp, "Additive processes for Piezoelectric Materials: Piezoelectric MEMS," in chapter 5 of a book of MEMS Materials and Processes Handbook, published by Springer, pp. 273-353 (2011)

5. K. Zheng and J. Lu, J. Chu, " A novel wet etching process of $Pb(Zr,Ti)O3$ thin films for applications in microelectromechanical system," J. Appl. Phys. 43, pp. 3934–3937 (2004)

6 R.G. Polcawich: Design, fabrication, test, and evaluation of RF MEMS series switches using lead zirconate titanate (PZT) thin film actuators, Ph.D. Thesis, Pennsylvania State University (2007)

7. J. Baborowski, P. Muralt, N. Lederman, “Etching of platinum thin films with dual frequency ECR/RF reactor,” Integrated Ferroelectrics, Vol. 27, pp. 243–256 (1999) 176

8.S. Koo, D. Kim, K. Kim, S. Song and C. Kim, “Etching properties of Pb(ZrxTi1-x)O3lead–zirconate–titanate thin films in an inductively coupled plasma Cl2/Ar and BCl3/Ar gas chemistries,” J. Vac. Sci. Technol. B 1622, pp.1519–1523 (2004)

9. C.W. Chung, “Reactive ion etching of $Pb(Zr_xTi_{1-x})O_3$ thin films in an inductively coupled plasma,” J. Vac. Sci. Technol. B 16, pp. 1894–1900 (1998)

10. P. Pertsch, S. Richter, D. Kopsch, N. Kramer, J. Pogodzik and E. Hennig, “Reliability of piezoelectric multilayer actuatros,” Contribution to the Actuator conference, Bremen, Germany, June 14-16 (2006)

VITA

Jung In Yang was born in Pusan, South Korea. In 1997 she received a Bachelors of Photographic Science and Engineering from Pukyoung National University in South Korea and in 2001 earned Master degree of Materials Science and Engineering from Korea University. She joined the group of Professor Susan Trolier-McKinstry to study for a doctorate degree in Materials Science and Engineering at the Pennsylvania State University in August 2010. She finished her long journey with a Ph.D. in Materials Science and Engineering in 2016.